Analysis of Operation and System Losses of an Inductive Power Transfer System for Wireless Charging of Electric Vehicles

Master of Science Thesis

Sotirios Sotiriou

September 2014

DELFT UNIVERSITY OF TECHNOLOGY

FACULTY OF ELECTRICAL ENGINEERING, MATHEMATICS AND COMPUTER SCIENCE

ELECTRICAL POWER PROCESSING

Analysis of Operation and System Losses of an Inductive Power Transfer System for Wireless Charging of Electric Vehicles

September 2014

Delft

Author

Sotirios Sotiriou

42520179

Thesis Committee

prof.dr.ir. P. Bauer

prof. dr. eng. J.A. Ferreira

prof.dr. L.R. Elizondo

Summary

The promotion of resource-saving technologies by the public authority was being intensified during the last years in order to reduce energy consumption and CO2-emissions. If charged from renewable energy sources, electric vehicles can contribute significantly to these objectives. Additionally, they can be employed to store and balance the fluctuating energy production of renewable sources. Therefore, however, a high availability of electric vehicles in the grid has to be guaranteed. In order to achieve a widespread dissemination of electric vehicles, several barriers for the usage have to be dismantled.

Available charging systems for electric vehicles use cables to connect the vehicle to the grid, although this involves certain disadvantages such as risk of vandalism, additional effort for the user and present safety issues due to the open contacts and hanging charging cables in public areas. Unplugged cables lead to uncharged batteries, which causes a minimization of mobility. A further reduction of the available range of electric vehicles is not acceptable. An alternative is wireless charging on the basis of resonant inductive energy transfer. This technology provides galvanic isolation, has no open contacts and hanging charging cables, which represent potential hazards in public places, and are susceptible to vandalism allowing an automatic, reliable and safe charging process. Therefore, automatic resonant inductive charging will improve the user acceptance of electric vehicles in general and will contribute to the integration of electric vehicles into the market and thus will support the full exploitation of benefits through electro-mobility.

This thesis discusses a topology for charging electric vehicles, the basic principles of wireless resonant inductive energy transfer, different coil configurations, resonant converter topologies and presents experimental results of a 3.3kW inductive energy transfer system with bidirectional energy flow capability operating at 140kHz.

Acknowledgements

This research was carried out at the Fraunhofer IWES Institute in Kassel, Germany. This thesis could not have been carried out without the help and support of many people. I would like to express my gratitude to them.

First of all, I would like to express my gratitude to my supervisor Prof. Pavol Bauer. I am truly grateful to him for his trust in my ability to complete this work. His patience and kindness are greatly appreciated.

I would also like to sincerely thank my supervisor in Fraunhofer IWES Georgios Lempidis. I will never forget the times we stayed overnight at work to complete measurements and experiments that needed to be carried out. Another person from Fraunhofer IWES that I would personally like to thank is Marco Jung, for showing me his trust.

Finally, I would like to thank Vasilis, Sofia, Fiorella and Mary, who have always been by my side, during good and bad times.

List of abbreviations

1. **ICE-- Internal Combustion Engines**
2. **HEV-- Hybrid Electric Vehicles**
3. **EV-- Electric Vehicles**
4. **FCV-- Fuel Cells Vehicles**
5. **IPT--Inductive Power Transfe**
6. **FHA-- First Harmonic Approximation**
7. **ZVS-- Zero Voltage Switching**
8. **EMI-- Electromagnetic Interference**
9. **ESR-- Equivalent Series Resistance**

List of figures

List of tables

Table of contents

1. Introduction

1.1. Inductive charging

Inductive charging is a method of transferring power wirelessly. A power generating source system is placed near a power storing or power transferring system. An electromagnetic field is generated between the two objects and power is transferred in a way similar to transferring power from the power grid to a local transformer. It is applied to a wide variety of systems; from small hand-held devices to robotic platforms and electric vehicles. [1]

1.2. History of Wireless Power Transmission

The beginning of wireless power transmission can be dated back to 1868 when James Clerk Maxwell developed the classical electromagnetic theory. Maxwell's equations unify previous unrelated observations of electricity, magnetism and optics into one consistent theory. Later in 1888, Heinrich Rudolf Hertz verified the existence of electromagnetic radiation by building the first radio transmitter. [2]

The first significant breakthrough in wireless power transmission technology happened in 1897 when Nikola Tesla filed his first patents based on the Wardenclyffe Tower, which is also known as Tesla Tower in Colorado Springs. Tesla resonated a 3 feet diameter copper ball on top of the 200 feet power with 300 kW of power from the Colorado Springs Electric Company.

There were various attempts after the Second World War to make an efficient transmission of large amount of power wirelessly but they have failed. This is because the device technology during that time was insufficient to either generate sufficient amount of power or effectively rectify the received microwave power. In 1964, William C. Brown invented the "Amplitron", which is commonly known as the crossed-field amplifier. The amplifier is capable of an output of 400 kW at efficiency of 70%. With the development of silicon Schottky-barrier diodes by Hewlett-Packard Associates, high efficiency high power wireless power transfer was made possible. In 1975, the largest wireless power transfer was demonstrated at the Venus Site of JPL Goldstone Facility. 450 kW of power was transmitted across one mile using a 26m diameter parabolic antenna. The 3.4m x 7.2m receiving rectenna array achieved a rectified DC power of 30 kW at 82.5% efficiency. The system efficiency was only 6.67% efficiency without taking the transmitter into consideration. Therefore, most of the power loss was still due to radiation. Generating a focused electromagnetic beam so that all of the energy can be projected onto a small area remains a challenging task. The only two ways to achieve an efficient power transfer over a long distance is to

increase the number of transmitting antenna elements so as to achieve a more focused beam or increase the number of elements of the receiving rectenna. Repeater stations can be used to reduce the radiation loses, but the conversion losses to retransmit the power can be so high that it is not feasible.

A more feasible alternative to the long range power transmission is via inductive coupling. However, the operating range is limited to the proximity of the transmitter. The roots of inductive coupling date back to 1831 when Michael Faraday demonstrated that in order to induce a current on a conductor the magnetic field needs to be changing. Faraday did not continue to pursue the work in this area and left it for others to pick up from where he left off. Among many who have tried to study the phenomena was Joseph Henry. All the experiments were conducted by manually turning on and off DC supplies, until the introduction of dynamo in 1860s making AC supply available. Sir William Grove was the first to connect a transformer to an AC source to generate high voltage for his laboratory work.

One of the earliest successful demonstrations of a consumer product using inductive coupling with considerable power is the inductive cooker. In 1971, during the National Association of Home Builders convention in Houston, TX Westinghouse Electric Company demonstrated single burner range using a 25 kHz operating frequency.

On the other end of the power band, General Electric introduced the rechargeable cordless electric toothbrush in 1961, mitigating the risk of an electric shock. The power transfer is achieved by splitting a transformer core into two, for which one of the core is located into the “base station” and the other is located in the toothbrush. Energy can be coupled to the toothbrush by placing it onto the “base station” with proper alignment.

The challenge of a robust inductive coupling is to be able to transfer energy to a receiving device with considerable lateral degree of freedom. In addition, portable electronics are getting very compact and lightweight, and consumers are unwilling to accept the huge heavy ferrite core. By using an air core transformer and with the receiver much smaller than the transmitter the coupling is extremely poor. The only solution is to increase the operating frequency to enhance the coupling but it is only in the recent years that power transistors are capable of achieving high power and high speed making considerable amount of power via magnetic induction possible. In addition, losses through the windings were significant due to skin depth and proximity effect until the introduction of Litz wires.

1.3. Inductive Charging for Electric Vehicles

Up to nowadays, fossil fuels have traditionally played the major role in covering the energy needs of people. This strong dependence has resulted in the excessive use of fossil fuels, which has led to environmental problems such as air pollution and

climate change. As a result, an ever growing awareness has been raised and added to the ever existing awareness that the use of fossil fuels is limited in time, due to their depletion. Therefore, the search for environmentally friendly solutions that can contribute to decrease the oil dependency has been accelerated. [3–5]

The transportation sector is the largest consumer of fossil fuel worldwide and thus the most important factor for reducing fossil fuel demand. Currently, the engineering world is undergoing a transformation in automobiles from internal combustion engines (ICE) vehicles to hybrid electric vehicles (HEV), electric vehicles (EV) and hydrogen fuel cells vehicles (FCV). Recent studies have shown that EV's outperform FCV's in several aspects including well-wheel efficiency, cost and weight. With the proviso that the electrical energy itself is sourced from green and renewable sources, the use of EVs (and also electric scooters and motor bicycles) in cities can help reduce urban and street pollution and contribute to the reduction to the usage of fossil.

An EV is a vehicle, which is powered by stored electrical energy and has zero emissions, if the electrical energy comes from sustainable energy sources. A pure EV needs sufficient battery storage on board to maintain its driving range. Additionally, the battery storage can be employed to store and balance the fluctuating energy production of renewable sources. Currently, chargers for EV's are plugin connections where the user is required to insert a plug into a receptacle on the car in order to charge the batteries. However, plugin connections come at the cost of several disadvantages. First, the cable and connector typically delivers 2-3 times more power than standard plugs at home and this increases risk of electrocution and sparks especially in wet and hostile environments. In public areas, hanging charging cables and long wires pose a trip hazard and can also be aesthetically poor for such systems. Additionally, additional effort for the user is introduced and unplugged or not properly plugged cables can lead to uncharged batteries, a fact which causes a minimization of mobility. A further reduction of the available range of electric vehicles is not acceptable. It should also be taken into account that in harsh climates that commonly have snow and ice, the plug-in charge point may become frozen onto the vehicle and that there is a constant risk of vandalism.

The answer to all these disadvantages comes with the introduction of wireless charging technology, on the basis of resonant inductive energy transfer. The main advantages of wireless charging systems are, amongst others, that they are appropriate for usage in harsh environments, as they are practically unaffected by weather or other external conditions, allowing an automatic, comfortable, reliable and safe charging process. The galvanic isolation they provide allows security during usage, and they require less maintenance, due to the fact that most of the components of the systems are protected due to proper encapsulation, that decreases their deterioration. This also decreases the cost of the system because of the low maintenance required. Therefore, automatic resonant inductive charging will improve the user acceptance of electric vehicles in general, will contribute to the integration of

electric vehicles into the market and will definitely support the full exploitation of benefits through electro-mobility.

1.4. Research goals and objectives

The main goals of this thesis are to demonstrate inductive power transfer as a feasible technology for charging application in EV and to study the implications of such charging infrastructure on stationary charging of such vehicles.

The following objectives were formulated:

- Develop firm theoretical background of an inductive power transfer system

The first objective of this thesis is to build firm theoretical background of the inductive power transfer technology based on the knowledge already existing in literature and to pin point key design criteria of an inductive power transfer system. The developed theory will not only be useful for designing an inductive power transfer system for EV applications but can be used in general for any inductive power transfer application.

- Building a prototype

The next objective of this thesis is to build a demonstrator to demonstrate inductive power transfer using the theory developed already. The main objective of building a prototype is to demonstrate that efficient power transfer over relatively large air gaps is achievable.

- Theoretical and experimental loss analysis of the system

The final objective of the thesis is the development of a mathematical model for the theoretical estimation of the losses of the system and the experimental validation of the calculations.

1.5. Structure of the Thesis

- The background theory of inductive power transfer is developed in Chapter 2. This chapter is dedicated to introducing the reader to the theory of inductive power transfer.
- Chapter 3 presents the coil topologies that can be used for the loosely coupled transformer of such a wireless power transfer system.

- In Chapter 4, the power electronic requirements of such a system are presented. Emphasis is given on the theoretical analysis of operation of the power electronic part of the system.
- The purpose of Chapter 5 is to theoretically analyze and calculate the losses and efficiency of a wireless power transfer system.
- The practical measurements carried out on the built prototype and their comparison with the theoretical calculations are included in chapter 6.
- Chapter 7 contains conclusions from previous chapters and recommendations for future work.

2. Theory behind inductive power transfer

2.1. Electromagnetic theory

Wireless transmission of energy using induction is based on the electromagnetic theory described by Maxwell's equations. Maxwell's equations describe how electric and magnetic fields are generated and altered by each other and by charges and currents. They are named after the Scottish physicist and mathematician James Clerk Maxwell who published an early form of those equations between 1861 and 1862. A current through a conductor produces a magnetic field. Variations in the magnetic field create an electric field. The electric field causes the electrical charges to move, producing a current. [6, 7]

2.2. Maxwell's Equations

“Maxwell's equations” is a collective name for four famous equations. These equations were discovered and refined by Gauss, Ampère, Faraday and Maxwell.

The first equation relates the electrical field with electrical charges.

$$\oint_S E \cdot dS = \frac{Q}{\varepsilon_0} \tag{1}$$

The second equation states that there are no sources or sinks for magnetic fields, all field lines are closed loops.

$$\oint_S \mathrm{B} \cdot dS = 0 \tag{2}$$

The third equation states that the electrical field is related to the change in the magnetic flux.

$$\oint_C E \cdot dl = \frac{-d\Phi_E}{dt} \tag{3}$$

The fourth equation relates the magnetic field with a current and the change in the electric flux.

$$\oint_C B \cdot dl = \mu_0 \left(I + \varepsilon_0 \frac{-d\Phi_E}{dt} \right) \tag{4}$$

The last equation states that, running a current through a closed loop will create a magnetic field, also known as magnetic flux density, B. This closed loop encloses a surface S. Through this surface there flows a magnetic flux Φ.

$$\Phi_B = \oint_S \mathrm{B} \cdot dS \tag{5}$$

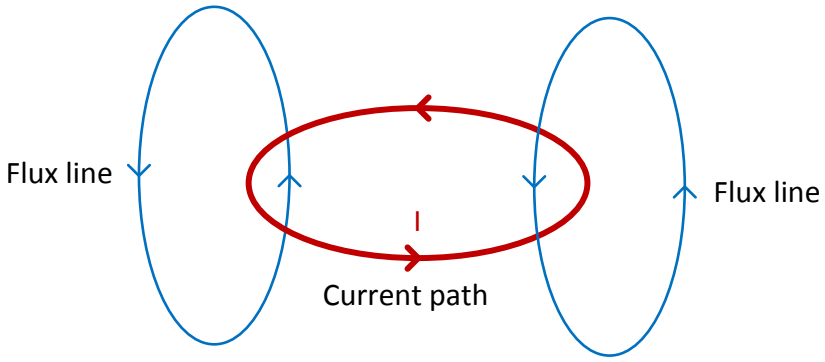

Figure 2-I Current path and flux lines

The magnetic flux density is proportional to the applied current, meaning the magnetic flux is also proportional to the current. This proportionality coefficient is the inductance L.

$$\Phi = LI \tag{6}$$

Placing a second closed loop in the vicinity of the first will cause some of the magnetic flux from the first loop, due to B_1, to pass through the surface of the second loop, S2. This is designated as the mutual flux Φ_{12}.

$$\Phi_{12} = \oint_{S_2} B_1 \cdot dS_2 \tag{7}$$

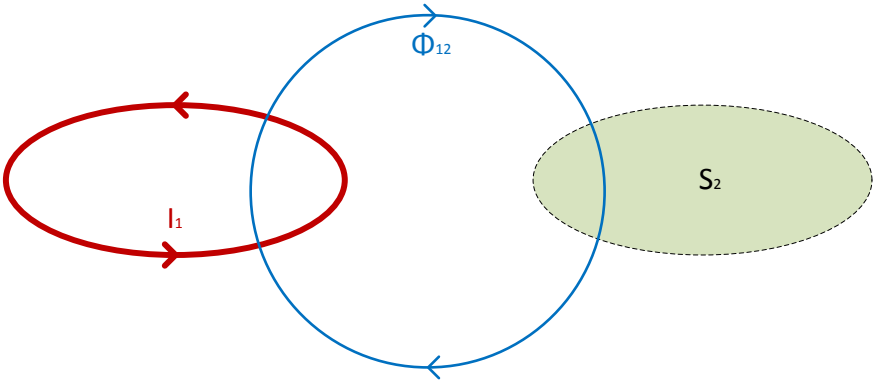

Figure 2-II Flux through the surface of the second loop S2

Running a current through the second loop instead, will produce another mutual flux.

$$\Phi_{21} = \oint_{S_1} B_2 \cdot dS_1 \tag{8}$$

The proportionality coefficient between the current and the mutual flux is the mutual inductance.

$$\Phi_{12} = L_{12} I_1 \tag{9}$$

$$\Phi_{21} = L_{21} I_2 \tag{10}$$

It turns out that the mutual inductances are the same:

$$M = L_{12} = L_{21} \tag{11}$$

2.3. Coils

A coil is used to run a current through a closed loop. If a coil has N coil turns, the current in each turn will add to the magnetic flux density. As a consequence, magnetic flux density B is proportional to the number N of turns carrying the current I.

$$B \propto \mathrm{NI} \tag{12}$$

The flux linkage Ψ is determined by:

$$\Psi = \mathrm{N}\Phi \tag{13}$$

The flux linkage Ψ can be used to calculate the self-inductance L of the coil.

$$L = \frac{\Psi}{I} \tag{14}$$

To sum up, self-inductance L is proportional to NΦ, Φ is proportional to B, and B is proportional to NI. This means that the self-inductance is proportional to the square of the number of turns of the coil.

$$L \propto \mathrm{N}^2 \tag{15}$$

In correspondence with the self-inductance, the following can be applied concerning the mutual inductance M. A current I_1 flows through a coil with N_1 turns, causing a magnetic flux density B_1.

$$B_1 \propto \mathrm{N_1 I_1} \tag{16}$$

The flux density B_1 will enable a mutual flux Φ_{12} , which links with the second coil.

$$\Phi_{12} = \oint_{S_2} B_1 \cdot dS_2 \tag{17}$$

If the number of the turns of the second coils with which the mutual flux Φ_{12} links is N_2, the flux linkage Ψ_{12} becomes

$$\Psi_{12} = \mathrm{N}_2 \Phi_{12} \tag{18}$$

This flux linkage Ψ_{12} can be used to calculate the mutual inductance M of the coils.

$$M = \frac{\Psi_{12}}{I_1} \tag{19}$$

To sum up, mutual inductance M is proportional to $N_2\Phi_{12}$, Φ_{12} is proportional to B_1, and B_1 is proportional to $N_1 I_1$. This means that the mutual inductance is proportional to the product of the number of turns each coil.

$$M \propto N_1 N_2 \tag{20}$$

The inductance of a coil is determined by the geometrical shape and the physical arrangement of the conductor as well as the permeability of the medium. The mutual inductance between two coils is further dependent on the distance and relative position of the two coils.

The coupling coefficient k is defined by

$$k = \frac{M}{\sqrt{L_1 L_2}} \tag{21}$$

For the coupling coefficient k, we have that $0 \leq k \leq 1$. This coefficient measures the magnetic coupling between the coils and is independent of the number of turns in the coils. It only depends on the relative positions of the two coils and the physical properties of the media in the vicinity of these coils.

2.4. Mutual inductance model

According to Faraday's law, as stated above, an alternating flux linkage causes an induced electromotive force (voltage).

$$u_2(t) = -\frac{d\Psi_{12}(t)}{dt} \tag{22}$$

The negative sign is compensated by changing the direction of the winding of the secondary coil. The current through the primary coil induces a voltage in the

secondary coil. If the secondary coil is part of a closed circuit, a current will flow. This current will cause a magnetic flux density, which in turn will cause a magnetic flux. This flux will oppose the mutual flux from the first coil. Using superposition the total flux linkage of the second coil will be described as a combination of the self-flux linkage and the mutual flux linkage.

$$\Psi_2(t) = \Psi_{12}(t) - \Psi_{22}(t) \tag{23}$$

Some flux from the current in the second coil will link with the first coil, and the total flux linkage of the first coil is defined in the same way.

$$\Psi_1(t) = \Psi_{11}(t) - \Psi_{21}(t) \tag{24}$$

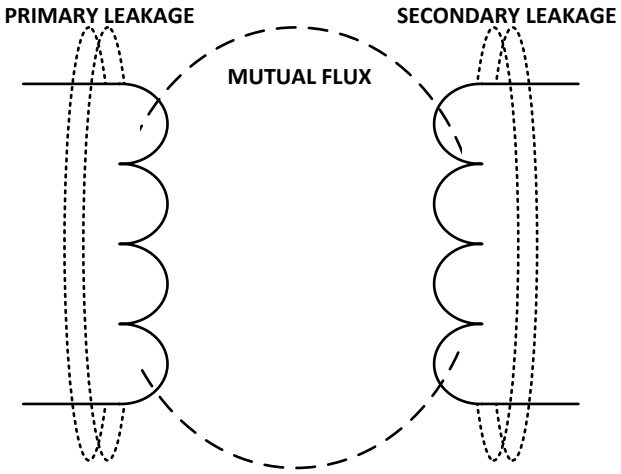

Figure 2-III Mutual and leakage fluxes

The primary leakage is the flux that is generated in the primary side that does not link with the secondary side; this is called primary leakage-flux (φ_1). A secondary leakage-flux (φ_2) is also generated. The mutualflux (φ_m) is the flux that links both sides in the transformer. These fluxes are electrically represented as inductances. Therefore, they are described as primary leakage inductance (L_1), secondary leakage-inductance (L_2) and mutual-inductance (L_m).

The equations are now described in terms of inductances.

$$\Psi_1(t) = L_1 i_1(t) - M i_2(t) \tag{25}$$

$$\Psi_2(t) = M i_1(t) - L_2 i_2(t) \tag{26}$$

Using Faraday's law on the total flux linkages of each coil, assuming the inductances are time invariant leads to the relationship between input voltage and current and output voltage and current.

$$u_1(t) = L_1 \frac{di_1(t)}{dt} - M \frac{di_2(t)}{dt} \tag{27}$$

$$u_2(t) = M \frac{di_1(t)}{dt} - L_2 \frac{di_2(t)}{dt} \tag{28}$$

If we assume that all the currents are sinusoidal in the steady state, these equations can also take a phasor form.

$$U_1 = j\omega L_1 I_1 - j\omega \mathrm{M} \mathrm{I}_2 \tag{29}$$

$$U_2 = j\omega \mathrm{M} I_1 - j\omega L_2 \mathrm{I}_2 \tag{30}$$

Finally, if we take into consideration the ohmic losses, which can be represented by resistances in series with the inductances, the above equations take the following form, which can be expressed by the following equivalent circuit diagram.

$$U_1 = R_1 I_1 + j\omega L_1 I_1 - j\omega \mathrm{M} \mathrm{I}_2 \tag{31}$$

$$U_2 = -R_2 I_2 + j\omega \mathrm{M} I_1 - j\omega L_2 \mathrm{I}_2 \tag{32}$$

2.5. Leakage Flux

The self-flux linkages are composed of two parts. The main flux linkage that connects with other coils and the leakage flux linkage that does not connect with any other coil. The name main flux linkage comes from the fact that in transformers the main flux linkage is the dominant part of the flux linkage. This is not the case with inductive power transfer.

$$\Psi_{11} = \Psi_{11}^m + \Psi_{11}^l \tag{33}$$

The main flux linkage is the mutual flux linkage linked with the coil that produced it.

$$\Psi_{11}^m = N_1 \Phi_1 \tag{34}$$

The main flux linkage is scaled by a factor N_1/N_2 and expressed as a scaling of the mutual inductance.

$$\mathrm{N}_1 \Phi_{12} = \frac{\mathrm{N}_1}{\mathrm{N}_2} \mathrm{N}_2 \Phi_{12} \Rightarrow \Psi_{11}^m = \frac{\mathrm{N}_1}{\mathrm{N}_2} M I_1 \tag{35}$$

The main inductance is then

$$L_1^m = \frac{\Psi_{11}^m}{I_1} = \frac{\mathrm{N}_1}{\mathrm{N}_2} M \tag{36}$$

This gives the leakage inductance expressed in inductances

$$L_1^l = L_1 - L_1^m \tag{37}$$

In the case of no secondary coil, the mutual inductance is zero, and the self-inductance consists only of the leakage inductance. If the coupling coefficient k goes to one, then the leakage inductance goes to zero.

2.6. Inductive Power Transfer (IPT) transformer

Inductive charging was developed from the electromagnetic theory, which is also the case for electrical transformers. An electrical transformer transfers power from a primary coil to a secondary coil. The source is isolated from the load but they are magnetically coupled. This magnetic coupling is physically achieved by a magnetic core. To determine the quality of coupling in an electrical transformer, we use the coupling coefficient k, which is obviously very high in electrical transformers (close to unity).

Following the same concept, it is possible to remove the magnetic core and achieve magnetic coupling between the primary coil and the secondary coil through the air. This modification leads to what is called an Inductive Power Transfer (IPT) transformer. In this way, electrical power could be transferred “wirelessly”.

An IPT transformer is composed by a primary winding and a secondary winding, which are separated by an air gap. The primary leakage is the flux that is generated in the primary side that does not link with the secondary side. A secondary leakage-flux is also generated. The mutual flux is the flux that links both sides in the IPT transformer. These fluxes are electrically represented as inductances. Therefore, they are described as primary leakage inductance L_a, secondary leakage inductance L_b and mutual-inductance M.

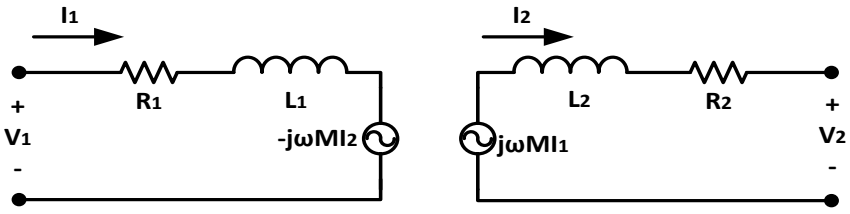

Figure 2-IV IPT transformer

In order to analyze the behavior of this system, the above presented equivalent circuit is sufficient. Each element can be identified as follows. The mutual inductance M becomes an important factor in the analysis of the IPT transformer. Because of the large air gap in an IPT transformer, the leakage-flux in each side is very high, consequently increasing the leakage inductances and decreasing the mutual inductance. Therefore, the coupling coefficient k is affected to a point where it becomes weak or very small. Logically, the power transfer capability is enormously affected.

The coupling model shown in the previous figure represents how the primary side is induced in the secondary side and how the secondary side is reflected to the primary side. Therefore, the analysis of this model could lead to an equivalent circuit to facilitate the study of the system. The equivalent secondary impedance Z_2 can be determined. Also, this secondary impedance could be reflected to the primary side. The equivalent secondary impedance reflected to the primary side is determined by the following equation.

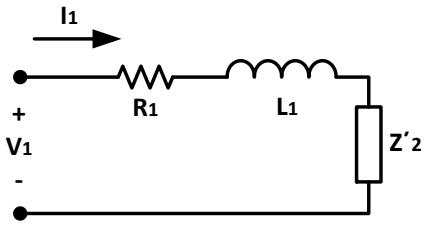

Figure 2-V Equivalent secondary impedance reflected to the primary side

The equivalent secondary impedance that is reflected to the primary side is nothing more than the load effect of the secondary side reflected to the primary side.

L_1 primary self inductance

L_2 secondary self inductance

L_a, L_b leakage inductances

M mutual inductance

$$L_1 = L_a + M$$

$$L_2 = L_b + M$$

$$n = \frac{N_1}{N_2} = 1, \qquad so\ \grave{L_2} = L_2$$

$$Z_2' = \frac{\omega^2 M^2}{Z_2}$$

The resulting equivalent impedance of the IPT transformer is defined by:

$$Z_{eq} = R_1 + j\omega L_1 + \left[\frac{\omega^2 \mathrm{M}^2}{R_2 + R_L + j\omega L_2}\right] \tag{38}$$

When an IPT transformer is magnetically coupled; the self-inductance of the primary side L_1 is equivalent to $L_a + M$ and the self-inductance of the secondary side L_2 is equivalent to $L_b + M$. Therefore, the above equation can be represented as follows.

$$Z_{eq} = R_1 + j\omega(L_a + M) + \left[\frac{\omega^2 \mathrm{M}^2}{R_2 + R_L + j\omega(L_b + M)}\right] \tag{39}$$

It can be presented graphically with the following equivalent circuit:

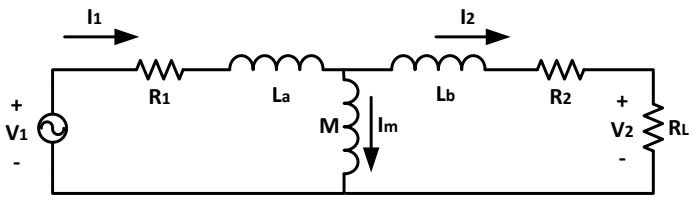

Figure 2-VI Equivalent circuit if IPT transformer

V_1 is a sinusoidal voltage source, I_1 is the current in the primary side, I_M is the magnetizing current, I_2 is the current in the secondary side V_2 is the voltage in the output of the IPT transformer and R_L a resistive load. This approach makes the analysis easier.

2.7. Power transfer capability

Because of the large air gap in an IPT transformer, the leakage-flux in each side is very high. This can be translated by increasing leakage-inductances and decreasing the mutual inductance between the primary and the secondary coils. Therefore, the coupling coefficient k is reduced in air gap transformers. The equivalent impedance of an IPT transformer has an inductive load characteristic. The more inductive the impedance is, the lowest the power factor will become affecting significantly the power transfer capability. Based in all the concepts that have been reviewed so far, the following general analysis is possible to be made; the larger the air gap in the IPT transformer, the larger will be the leakage-flux and leakage inductance. Therefore, the system will become more inductive and consequently the power factor will decrease affecting the power transfer capability.

In order to be able to transfer energy efficiently with relatively low coupling factor the reactive power of the leakage inductances needs to be compensated by capacitors. [6, 8, 9]

3. Coil Topologies

3.1. Magnetic coupling

Most modern cars have clearance to ground around 15 to 20 cm; so an air gap of 20 cm would be optimum to be used in the study for Inductive Power Transfer (IPT) transformers, which can be used for wireless charging of electric vehicles. The size of coils is restricted by the bottom surface size of the vehicle.

The current density in the primary coils generates a magnetic field rotating around the conductor:

$$\nabla \times \overrightarrow{H_p} = \overrightarrow{J_p} \tag{40}$$

This magnetic field is partially coupled with the secondary coil and is divided into two parts; the used field $\overrightarrow{H_{use}}$, which establishes an electric field in the secondary coil and the leakage field $\overrightarrow{H_{leak}}$, which does not participate in the establishment of an electric field in the secondary coil. [10]

The ratio of these two parts of the magnetic field strength is determined by the geometry and material of the coil system components and can be described by the coupling factor k or the leakage factor σ. These factors can be calculated through the inductances of the equivalent coil system, like in the case of a transformer.

$$k = \frac{M}{\sqrt{L_1 L_2}} \tag{41}$$

$$\sigma = 1 - k^2 \tag{42}$$

As it has already been stated, the magnetic flux is represented by inductances in the equivalent circuit to simplify the calculation.

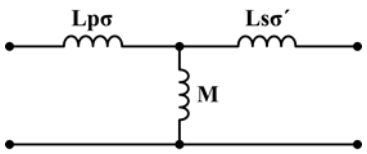

Figure 3-I Simplified equivalent circuit

Only the effective magnetic field $\overrightarrow{H_{use}}$ establishes an electric field in the secondary coil. This electric field creates a voltage in the conductor of the secondary coil and a current density, if the conductor is connected to a closed circuit.

$$\overrightarrow{B_s} = \mu \cdot \overrightarrow{H_{use}} \tag{43}$$

$$\nabla \times \overrightarrow{E_s} = -\frac{\partial \overrightarrow{B_s}}{\partial t} \tag{44}$$

This phenomenon is called coupling of the magnetic field. The coupling factor is a very important term for the energy transfer efficiency and therefore it must be as increased as possible. It strongly depends on the coil geometry and air gap. The changes in the air gap can only be of a small range but the customization possibilities are far better.

Many structures of the geometry of the coil system have been investigated. Different coil geometries could be used for the energy transfer system. However, only the simplest system with two round coils can be calculated analytically. The equation systems from other coil systems are too complex to be analytically calculated. This is the reason why all of the systems proposed are simulated numerically with Finite Element Modeling (FEM) and measured with real coils.

3.2. Field concentration

A piece of magnetic material with a high permeability used to confine and guide magnetic fields can prove to be of great usefulness for the Inductive Power Transfer (IPT) Transformer. It is made of ferromagnetic metal such as iron, or ferromagnetic compounds such as ferrites. The high permeability, relative to the surrounding air, causes the magnetic field lines to be concentrated in the core material. The magnetic field is often created by a coil of wire around the core that carries a current. The presence of the high permeability material can increase the magnetic field of a coil by a factor of several thousand over what it would be without the core. In this way, the magnetic flux can be "guided" through desired paths, which are decided by the topology geometry and could allow an improvement of the coupling between the primary and the secondary.

Ferrite ceramics are used for high-frequency applications. The ferrite materials can be engineered with a wide range of parameters. As ceramics, they are essentially insulators, which prevents eddy currents, although losses such as hysteresis losses can still occur.

Electrically well conducting layers like Copper or Aluminum are well able to shield alternating magnetic fields, due to induced eddy currents. Skin effect arises when the eddy currents flowing in the layer at any depth produce magnetic fields which oppose the primary field, thus reducing the net magnetic flux and causing a decrease in current flow as the depth increases. Therefore, Eddy Currents near the

surface can be viewed as shielding the magnetic field on the layer, thereby weakening the magnetic field at greater depths and reducing induced currents.

3.3. Planar coils

The simplest system is a pair of ring coils. They are really easy to build, but they do not offer the optimum solution for leading the magnetic field. [10, 11]

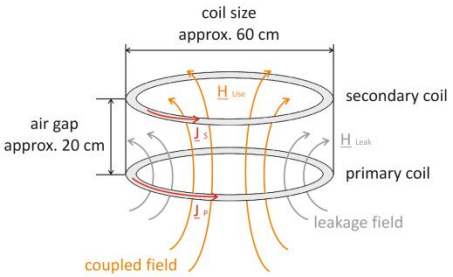

Figure 3-II Magnetic flux in a planar coil system

- Diameter of the coil area: D ≈ 580 mm
- Air gap: g ≈ 200 mm
- Diameter of the coil conductor: d ≈ 3 mm
- Turns of coils: N = 8

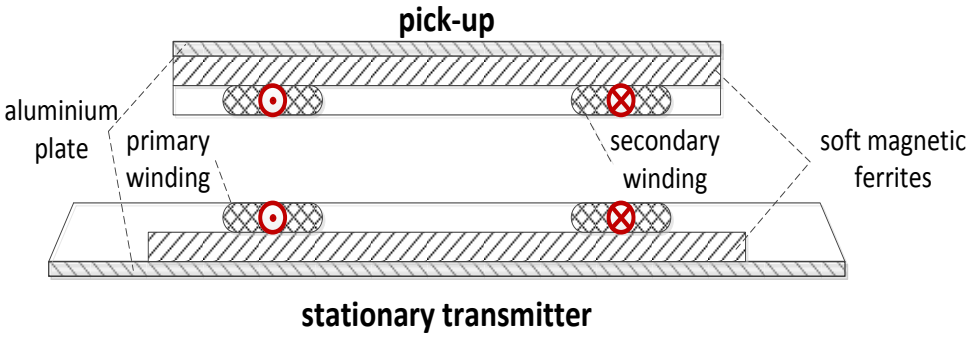

Figure 3-III Planar coil system

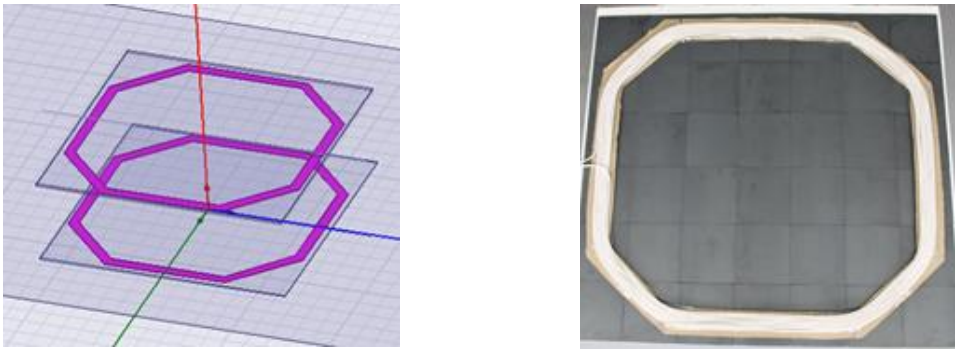

Figure 3-IV Planar coils FEM Simulation Model and Planar coil photo

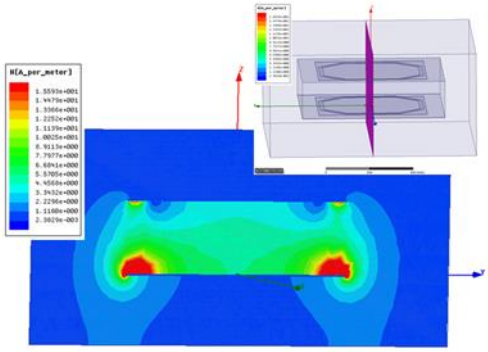

Figure 3-V Magnetic field strength (H) in planar coil system

The planar coil system design can achieve coupling, but not quite tight. It requires the use of much ferrite, because the flux is led outside the rings, a fact that makes it cost ineffective. Finally, it can be introduced for bidirectional operation, due to its symmetrical design.

3.4. Double D coils

Another way to lead the magnetic field is the “double D” structure. Instead of two plane ring coils with a unidirectional coupling of the magnetic fields, four coils are installed in order to couple the magnetic field in both directions. [10, 11]

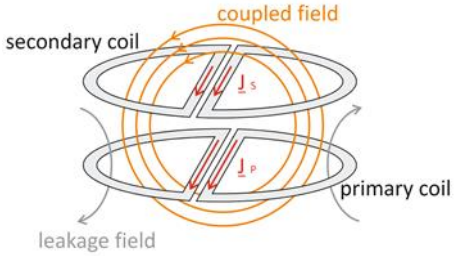

Figure 3-VI Magnetic field flux in the double D coils

Diameter of the coil area: D ≈ 580 mm
Air gap: g ≈ 200 mm
Diameter of the coil conductor: d ≈ 3 mm.
Turns of coils: N = 6

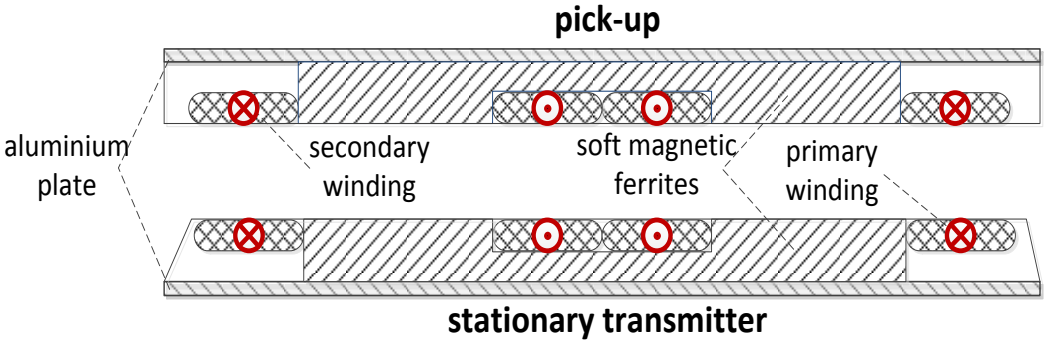

Figure 3-VII Double D coil system

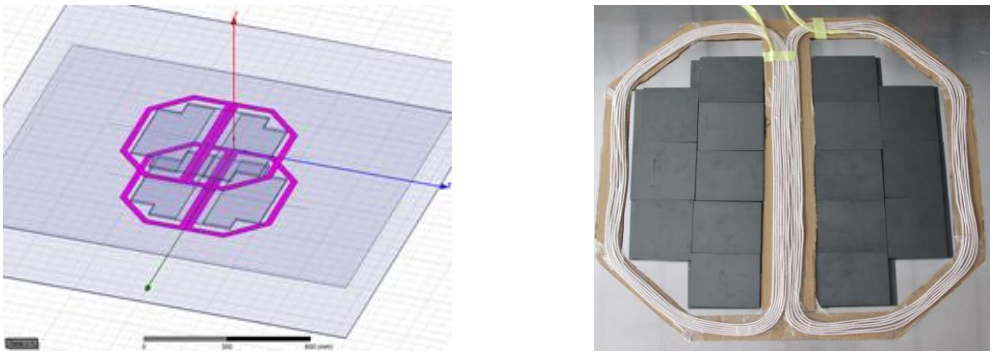

Figure 3-VIII Double D coils FEM Simulation Model and Double D coil photo

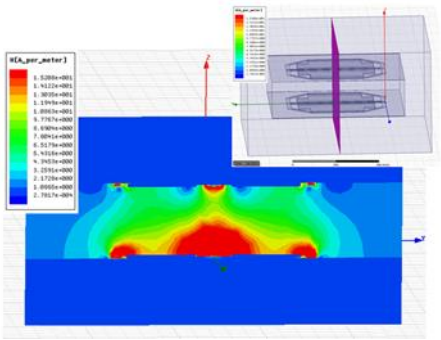

Figure 3-IX Magnetic field strength (H) in Double D coil system

The double D topology achieves a sufficient coupling factor, even for larger distances and it can be also applied for bidirectional operation. Additionally, it requires less ferrite, in comparison with the planar coil design Combination

3.5. Double D and Solenoid coils

The use of different coil geometries in one system is important for the interoperability of different inductive charging systems. In this case, the magnetic field must be correctly led between the primary and secondary side. This implies that the coils must be mounted in the appropriate position, which allows the magnetic field lines to travel through the whole area of the coils, according to the induction and Ampere´s law. [10]

In the double D coil topology the generated field lines are led from one "D" to the other "D". A solenoid coil can be put on their way to couple with these field lines. The solenoid is lighter, smaller and therefore simpler to be mounted underneath the car.

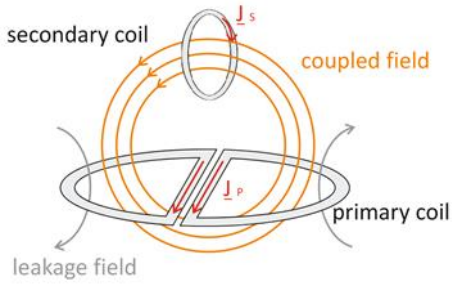

Figure 3-X Magnetic field flux of the combination in double D and solenoid coils

Diameter of the stationary coil area: $D_P \approx 580$ mm
Air gap: g ≈ 200 mm
Diameter of the coil conductor: d ≈ 3 mm.
Length of the secondary coil: $L_s \approx 210$ mm
Turns stationary coil: $N_P = 6$
Turns pick-up coil $N_S = 18$

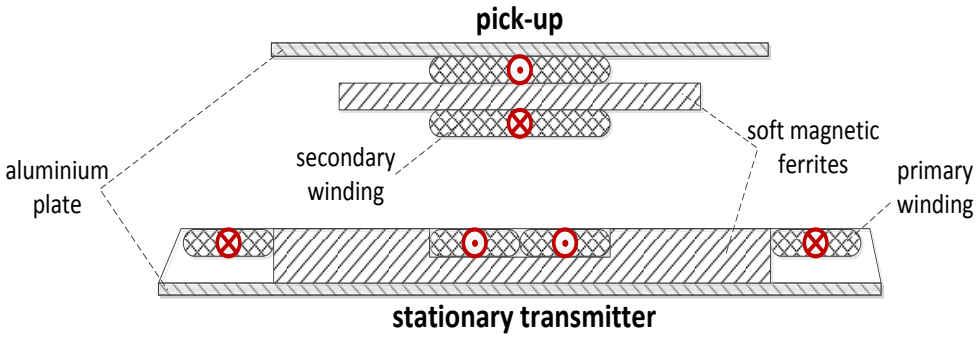

Figure 3-XI Combination of double D and Solenoid coil system

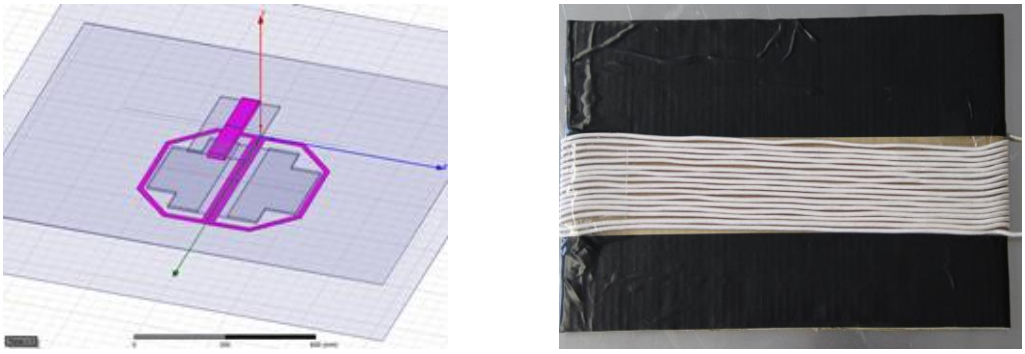

Figure 3-XII Double D and Solenoid coil System FEM Simulation Model and photo of solenoid pick-up coil

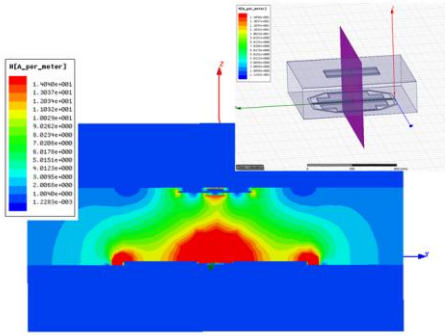

Figure 3-XIII Magnetic field strength (H) in combination of double D and solenoid coil system

This topology can offer a solution in case of lack of available space. However, it does not have very good coupling performance and, of course, it cannot operate in both directions of power flow.

3.6. Inductance Characterization of High-Leakage Transformers

High-leakage transformers play an important role in power conversion in areas ranging from resonant conversion for DC/DC applications to the separable-transformer based systems used in automotive power transfer. It is out of the question that transformer leakage can critically affect the operation of standard transformers and converters.

Thus, we are interested in quantifying the magnitude of the leakage parameters associated with the transformer primary and secondary windings. Characterization of these discrete leakages can be especially important for optimizing the functionality, efficiency, and modeling of applications using loosely-coupled transformers.

Significant research has been done in the analysis and calculation of leakage inductance, and measurements in these references are largely based on a standard test with approaches, featuring primary open-circuit and short-circuit tests. However, this two-test approach may lose its accuracy, as the impedance of the leakage inductance and the winding series resistance increase to a point that it is no longer accurate to consider them insignificant in comparison with the magnetizing inductance impedance. Additionally, the primary and secondary leakage inductances are very likely to differ due to different winding geometries and configurations. These test inaccuracies can be overcome by the implementation of a third test, which is based on the secondary open circuit inductance. [12]

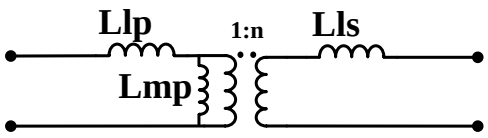

Figure 3-XIV Equivalent circuit of loosely coupled coils

The inductance measured at the primary with the secondary shorted, $L_{p(ss)}$, is given by:

$$L_{p(ss)} = L_{lp} + L_{mp} \,//\, \frac{L_{ls}}{n^2} = L_{lp} + \frac{L_{mp}L_{ls}}{n^2 L_{mp} + L_{ls}} \tag{45}$$

where L_{ls} is the secondary leakage inductance and 1:n is the primary-secondary turns ratio.

In the first approach, which is commonly used, the magnetizing inductance is determined by measuring the open-circuit secondary voltage $V_{s(oc)}$ in response to an exciting voltage $V_{p(oc)}$ applied to the primary winding.

$$L_{mp} = L_p \frac{V_{s(oc)}}{n \cdot V_{p(oc)}} \tag{46}$$

$$L_{lp} = L_p - L_{mp} \tag{47}$$

$$L_{ls} = \frac{n^2 L_{mp}\left(L_{p(ss)} - L_{lp}\right)}{L_{mp} + L_{lp} - L_{p(ss)}} \tag{48}$$

There is also a second approach, in which the secondary open-circuit inductance L_s is directly measured. This test is used for characterization, as it is consistent with the measurements of open-circuit and short-circuit inductances, which

are carried out using a LCR meter. The expression for the mutual inductance, M, is easily derived, and can be expressed in terms of the three test parameters L_p, L_s, and $L_{p(ss)}$:

$$M = \sqrt{\left(L_p - L_{p(ss)}\right) L_s} \tag{49}$$

Inductances L_{lp}, L_{ls}, and L_{mp}, and secondary-referenced magnetizing inductance L_{ms} are then calculated:

$$L_{mp} = \frac{1}{n} M \tag{50}$$

$$L_{ms} = nM \tag{51}$$

$$L_{lp} = L_p - L_{mp} \tag{52}$$

$$L_{ls} = L_s - L_{ms} \tag{53}$$

3.7. Coupling factor experimental calculation

The coil topology which is of most interest is the double D topology. It achieves a sufficient coupling factor, even for larger distances, it can be also applied for bidirectional operation and requires less ferrite, in comparison with the planar coil design, which also offers bidirectionality. In this section, the coupling factor that can be achieved through this topology is investigated, concerning several displacements of the secondary with respect to the primary.

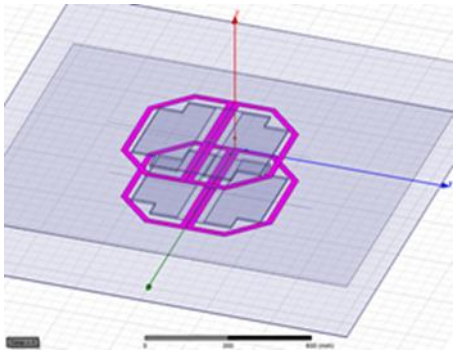

Figure 3-XV X, Y, Z dimensions of the double D coils

3.8. Coupling factor with respect to distance between primary and secondary

The three test approach was followed for aligned primary and secondary for different distances between them (12cm-21cm). The results are presented in the table below:

Distance(cm)	Lp(µH)	Ls(µH)	Lpss(µH)	Lm(µH)	Lrp(µH)	Lrs(µH)	k(%)
12	154,2	147,02	111,56	79,18	75,02	67,84	52,59
14	143,54	136,22	117,38	59,70	83,84	76,52	42,69
16	138,34	130,81	120,32	48,55	89,79	82,26	36,09
17	135,38	131,52	119,76	45,32	90,06	86,20	33,97
18	135,14	127,6	122,1	40,79	94,35	86,81	31,06
20	131,94	126,04	122,94	33,68	98,26	92,36	26,12
21	132,14	123,5	124,89	29,92	102,22	93,58	23,42

Table 3-1 Three test approach for aligned primary and secondary

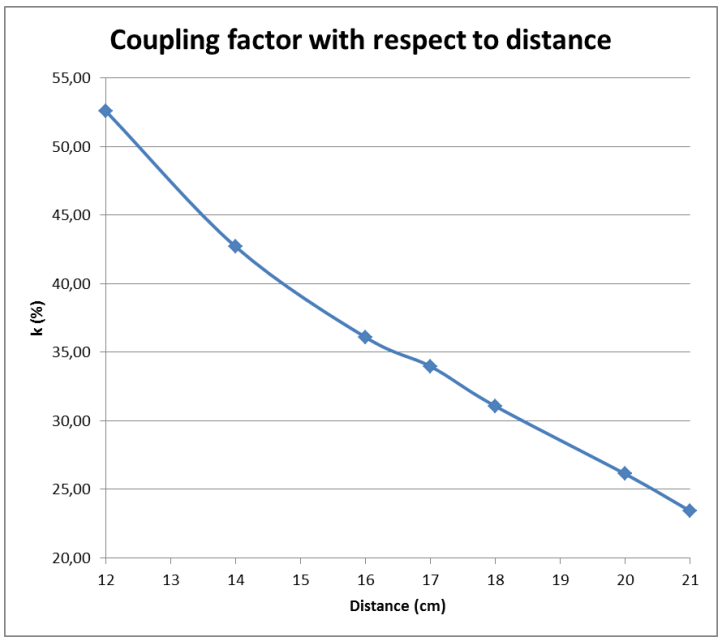

Figure 3-XVI Coupling factor with respect to distance

The two coils are tightly coupled for small distances. As expected the coupling factor degrades with the distance. However, a coupling factor of 26,12% for a distance 20cm is a quite satisfying value. With proper capacitive compensation, it can accomplish wireless power transfer.

3.9. Coupling factor with respect to displacement of the secondary

The three test approach was also followed for different displacements of the secondary with respect to the primary. The distance between them was 20cm, and measurements took place for displacements along the X axis (0-15cm) and the Y axis(0-15cm). The results are presented in the table below:

#	X(cm)	Y(cm)	Z(cm)	Lp(µH)	Ls(µH)	Lpss(µH)	Lm(µH)	Lrp(µH)	Lrs(µH)	k(%)
1	0	0	20	118,6	125,78	110,35	32,21	86,39	93,57	26,37
2	0	5	20	117,94	125,3	110,6	30,33	87,61	94,97	24,95
3	0	10	20	118,26	123,5	112,92	25,68	92,58	97,82	21,25
4	0	15	20	128,46	121,68	125,7	18,33	110,13	103,35	14,66
5	5	0	20	131,94	126,04	122,94	33,68	98,26	92,36	26,12
6	5	5	20	121,22	124,98	113,32	31,42	89,80	93,56	25,53
7	5	10	20	120,32	123,3	114,78	26,14	94,18	97,16	21,46
8	5	15	20	118,74	120,78	116,32	17,10	101,64	103,68	14,28
9	10	0	20	118,16	125,26	110,54	30,89	87,27	94,37	25,39
10	10	5	20	117,88	124,4	111,2	28,83	89,05	95,57	23,80
11	10	10	20	130,96	122,84	126,12	24,38	106,58	98,46	19,22
12	10	15	20	114,7	121,16	112,72	15,49	99,21	105,67	13,14
13	15	0	20	130,82	123,86	123,38	30,36	100,46	93,50	23,85
14	15	5	20	131,7	123,54	125,16	28,42	103,28	95,12	22,28
15	15	10	20	129,75	122,04	126,18	20,87	108,88	101,17	16,59
16	15	15	20	114,4	120,12	112,86	13,60	100,80	106,52	11,60

Table 3-2 Results of the three test approach for aligned primary and secondary

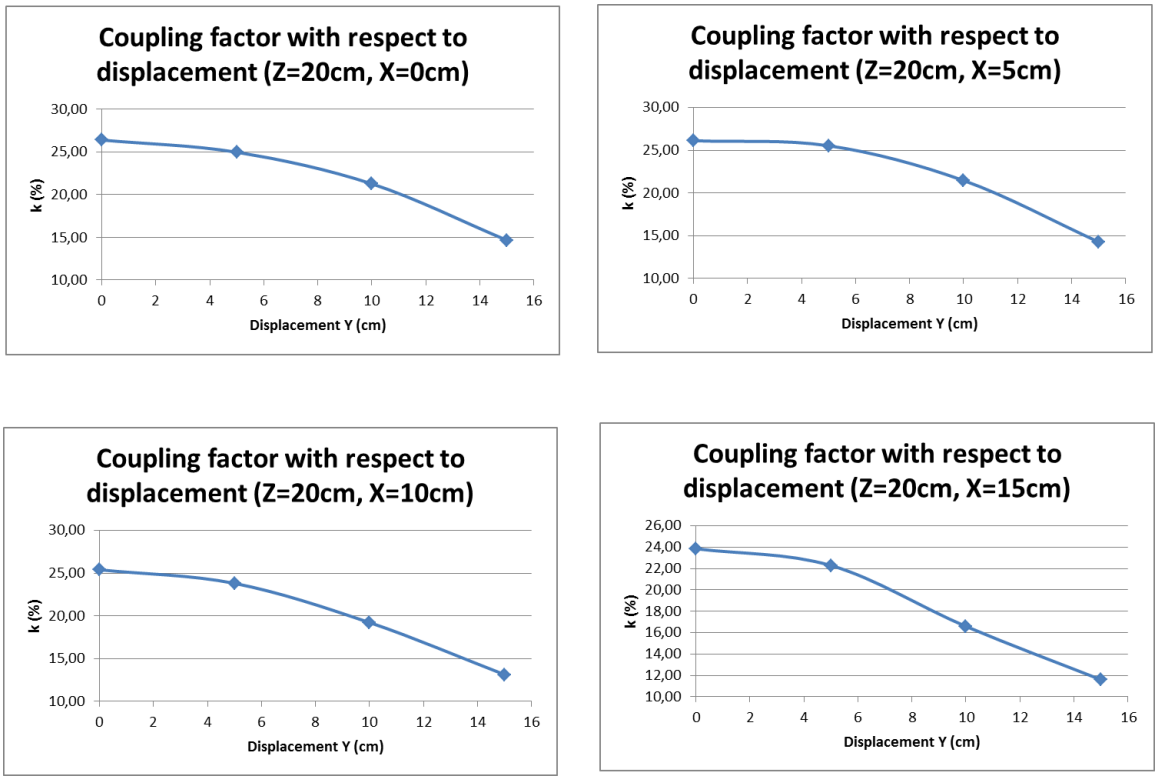

Figure 3-XVII Coupling factor with respect to several displacements

It can be seen that the coupling factor is sufficiently high, even for bigger displacements along the X axis.

4. Analysis of operation

4.1. Resonant Converter

A CLLC resonant converter is a transformer coupled dc/dc converter whose output voltage is controlled by the switching frequency. A rectangular voltage waveform with variable frequency is created. As it can be seen by the transfer function characteristics, the output voltage can be controlled by setting the switching frequency. The key elements of a CLLC resonant converter are already mentioned in its name – two inductors and two capacitors. The resonant inductivity Lr, the main inductivity Lm of the transformer, and the resonant capacitors Cr form the resonant tank. Resonant converters are commonly selected for applications which demand for a high power density and a high energy efficiency. By featuring soft-switching, the switching frequency can in general be chosen much higher than the switching frequency of a comparable hard-switching converter.

For the built wireless power transfer system, a bidirectional full-bridge CLLC resonant converter using a new symmetric CLLC-type resonant network is proposed. The bidirectional CLLC resonant converter with a full bridge configuration approach is depicted below. It has a structure of two symmetric full bridges, one for the primary inverting stage and one for the secondary rectifying stage, with a symmetric Inductive Power Transfer high frequency transformer between them. Power switches in the primary inverting stage convert power from dc to ac, in order to transfer it through the transformer, which is modeled with the magnetizing inductance Lm and the transformer's turn ratio of 1:1. It is usual that the load is represented as an equivalent resistance. [8] The leakage inductance of the primary and secondary windings of the transformer is merged to the resonant inductors Lr1 and Lr2 respectively. The resonant capacitors Cr1 and Cr2 in combination with Lr1 and Lr2 constitute the resonant tank, which has high resonant frequencies.

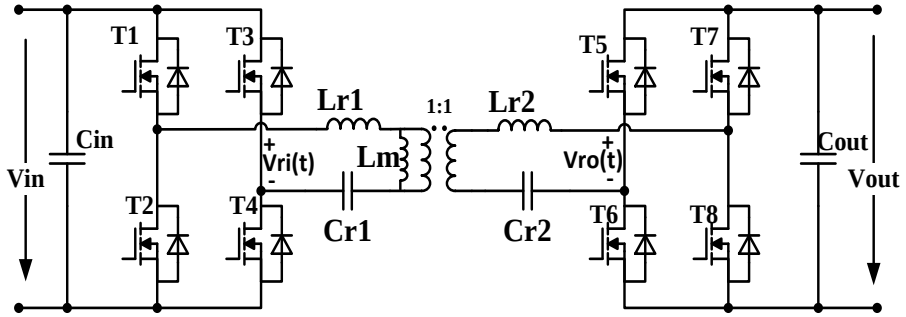

Figure 4-IFull Bridge CLLC resonant converter

Since the resonant capacitor Cr2 is added to the resonant network in the secondary side, the resonance in the resonant network is more complicated than the resonance of a conventional converter's resonant network, and one more resonant peak is added to the gain curve with respect to the switching frequency.

4.2. First Harmonic Approximation Model and Gain Characteristics

The CLLC resonant tank behaves like a band-pass filter. By taking that into account, it could be assumed that only the fundamental components of the voltage and current in the resonant tank are responsible for the power transfer. [13] This assumption can lead to sufficiently accurate results and is called the first harmonic approximation (FHA). The fundamental harmonic component can be derived by the Fourier series expansion, and other harmonics are neglected. First harmonic approximation can be used for the analysis of the gain curve characteristic of the symmetric resonant network in the frequency domain. In the following section, the Fourier series analysis of the waveforms that can be met during the operation of the converter is presented. All the detailed calculations can be found in the appendix.

$$V(t)=\begin{cases}-V, for -\pi \le \omega t \le 0\\ V, for\ 0 \le \omega t \le \pi\end{cases}$$

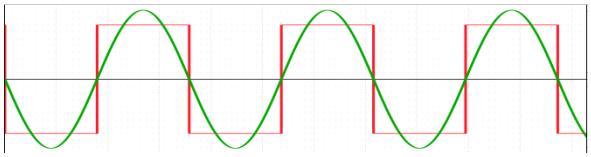

Figure 4-II First harmonic of square wave

$$a_n=\frac{1}{\pi}\int_{-\pi}^{\pi}V(t)\cos(n\omega t)\,d\omega t, n\ge 0 \tag{54}$$

$$b_n=\frac{1}{\pi}\int_{-\pi}^{\pi}V(t)\sin(n\omega t)\,d\omega t, n\ge 0 \tag{55}$$

$$a_0=\frac{1}{\pi}\int_{-\pi}^{\pi}V(t)\,d\omega t=\frac{1}{\pi}\left(\int_{-\pi}^{0}(V)\,d\omega t+\int_{0}^{\pi}V d\omega t\right)=0 \tag{56}$$

$$a_1=\frac{1}{\pi}\int_{-\pi}^{\pi}V(t)\cos(\omega t)\,d\omega t=0 \tag{57}$$

$$b_1=\frac{1}{\pi}\int_{-\pi}^{\pi}V(t)\sin(\omega t)\,d\omega t=\frac{4}{\pi}V \tag{58}$$

$$V(t)=\begin{cases}0, for -\pi \le \omega t \le 0\\ V, for\ 0 \le \omega t \le \pi\end{cases}$$

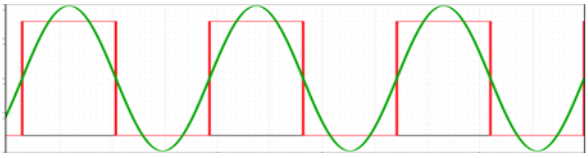

Figure 4-III First harmonic of square wave

$$a_n=\frac{1}{\pi}\int_{-\pi}^{\pi}V(t)\cos(n\omega t)\,d\omega t, n\ge 0 \tag{59}$$

$$b_n=\frac{1}{\pi}\int_{-\pi}^{\pi}V(t)\sin(n\omega t)\,d\omega t, n\ge 0 \tag{60}$$

$$a_0=\frac{1}{\pi}\int_{-\pi}^{\pi}V(t)\,d\omega t=\frac{V}{2} \tag{61}$$

$$a_1=\frac{1}{\pi}\int_{-\pi}^{\pi}V(t)\cos(\omega t)\,d\omega t=0 \tag{62}$$

$$b_1=\frac{1}{\pi}\int_{-\pi}^{\pi}V(t)\sin(\omega t)\,d\omega t=\frac{2}{\pi}V \tag{63}$$

4.3. Full bridge configuration-FHA model

The switching scheme that is suitable for the resonant converter is a 50% duty cycle for each switch of the full bridge legs. The output $V_{ri}(t)$ of the full bridge in the primary side of the Wireless Power Transfer converter is

$$V_{ri}(t)=\begin{cases}-V_d, for -\pi \le \omega t \le 0\\ V_d, for\ 0 \le \omega t \le \pi\end{cases} \tag{64}$$

The fundamental harmonic component of this voltage is $u_{ri,FHA}(t)$:

$$u_{ri,FHA}(t)=\frac{4}{\pi}\cdot V_d\cdot\sin(2\pi f_s\cdot t) \tag{65}$$

the rms value of $u_{ri,FHA}(t)$ is $V_{ri,FHA}$:

$$V_{ri,FHA}=\frac{2\sqrt{2}}{\pi}\cdot V_d \tag{66}$$

The input $V_{ro}(t)$ of the output rectifier in the secondary side of the Wireless Power Transfer converter is

$$V_{ro}(t)=\begin{cases}-V_o,\ for-\pi\le\omega t\le 0\\ V_o,\ for\,0\le\omega t\le\pi\end{cases} \tag{67}$$

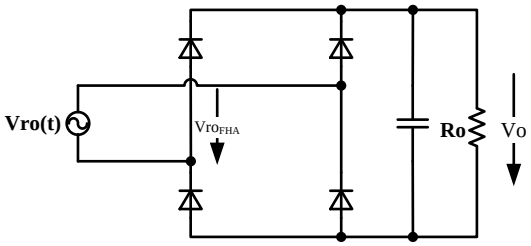

Figure 4-IV Output rectifier

The fundamental harmonic component of this voltage is $u_{ro,FHA}(t)$:

$$u_{ro,FHA}(t)=\frac{4}{\pi}\cdot V_o\cdot\sin(2\pi f_s\cdot t-\varphi) \tag{68}$$

The rms value of $u_{ro,FHA}(t)$ is $V_{ro,FHA}$:

$$V_{ro,FHA}=\frac{2\sqrt{2}}{\pi}\cdot V_o \tag{69}$$

For the rectifier current $i_{rct,FHA}(t)$, we have:

$$i_{rct,FHA}(t)=\sqrt{2}\cdot I_{rct,FHA}\cdot\sin(2\pi f_s\cdot t-\varphi) \tag{70}$$

Where $I_{rct,FHA}$ is the rms value of the fundamental harmonic component of the rectifier current.

The average value output current I_o is given by:

$$I_o=\frac{2}{T_s}\int_0^{\frac{T_s}{2}}\left|i_{rct,FHA}(t)\right|dt=\frac{2\sqrt{2}}{\pi}\cdot I_{rct,FHA} \tag{71}$$

$u_{ro,FHA}(t)$ and $i_{rct,FHA}(t)$ are in phase, so the resistive load of the resonant network $R_{o,e}$ can be given by the ratio of the instantaneous voltage and current:

$$R_{o,e}=\frac{u_{ro,FHA}(t)}{i_{rct,FHA}(t)}=\frac{8}{\pi^2}R_o \tag{72}$$

The FHA equivalent model of the bidirectional CLLC converter is presented below:

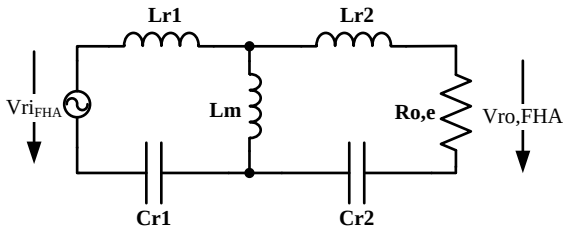

Figure 4-V FHA equivalent model of the bidirectional CLLC converter

$$\frac{V_{ro,FHA}}{V_{ri,FHA}} = \frac{L_m // \left(\boldsymbol{j}\omega \cdot L_{r2} + R_{o,e} + \frac{1}{\boldsymbol{j}\omega \cdot C_{r2}} \right)}{\frac{1}{\boldsymbol{j}\omega \cdot C_{r1}} + \boldsymbol{j}\omega \cdot L_{r1} + \left[L_m // \left(\boldsymbol{j}\omega \cdot L_{r2} + R_{o,e} + \frac{1}{\boldsymbol{j}\omega \cdot C_{r2}} \right) \right]} \cdot \frac{R_{o,e}}{\boldsymbol{j}\omega \cdot L_{r2} + R_{o,e} + \frac{1}{\boldsymbol{j}\omega \cdot C_{r2}}}$$

$$\frac{V_o}{V_d} = \frac{L_m // \left(\boldsymbol{j}\omega \cdot L_{r2} + \frac{8}{\pi^2} R_o + \frac{1}{\boldsymbol{j}\omega \cdot C_{r2}} \right)}{\frac{1}{\boldsymbol{j}\omega \cdot C_{r1}} + \boldsymbol{j}\omega \cdot L_{r1} + \left[L_m // \left(\boldsymbol{j}\omega \cdot L_{r2} + \frac{8}{\pi^2} R_o + \frac{1}{\boldsymbol{j}\omega \cdot C_{r2}} \right) \right]} \cdot \frac{\frac{8}{\pi^2} R_o}{\boldsymbol{j}\omega \cdot L_{r2} + \frac{8}{\pi^2} R_o + \frac{1}{\boldsymbol{j}\omega \cdot C_{r2}}} \quad (73)$$

This transfer function leads to the following transfer characteristic:

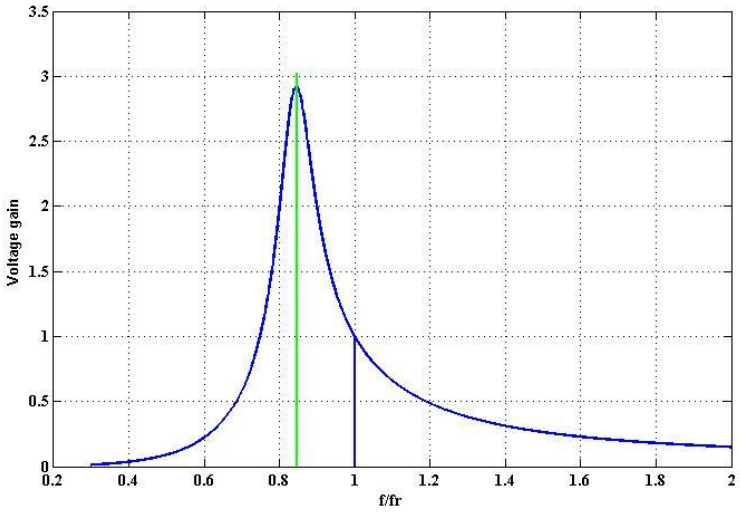

Figure 4-VI Transfer characteristic of the full bridge CLLC resonant converter

There are **two resonant frequencies** observed in the transfer characteristic of the converter. The primary one is:

$$f_r = \frac{1}{2\pi\sqrt{Lr_1 \cdot Cr_1}} \quad (74)$$

There is also a secondary resonant frequency, that is given by:

$$f_{r2} = \frac{1}{2\pi\sqrt{(Lr_1 + L_m)\cdot Cr_1}} \tag{75}$$

The transfer characteristic also depends on the load connected to the secondary side and on the coupling that has been achieved for the IPT transformer. The dependence on these two important factors is shown below.

The quality factor Q is a factor that depends directly on the load connected to the secondary side:

$$Q = \frac{\omega_0 L_r}{R_{o,e}} \tag{76}$$

As it can be seen from the characteristic shown below, the quality factor Q affects the peak gain of the converter.

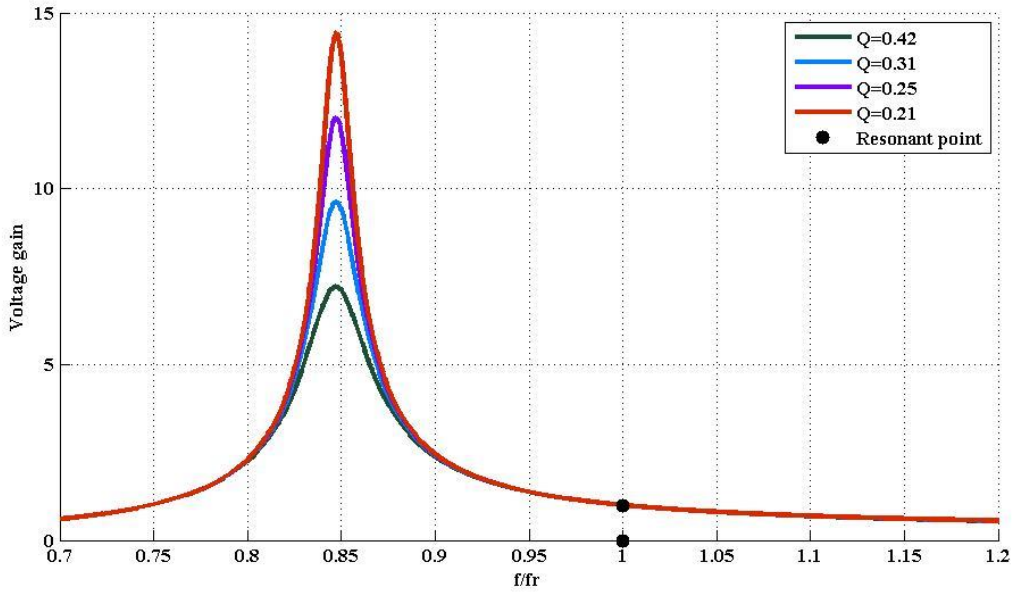

Figure 4-VII Transfer characteristic for different quality factor values

The gain has a peak value at the low resonant frequency which contains the magnetizing inductance as a resonant component. At the primary resonant frequency f_r, converter operates with unity gain. In the light-load condition, the gain is high and the slope of the gain curve is sharp. However, the overall value of the gain curve is decreasing under the heavy-load condition.

The coupling factor k is a factor that expresses how well the primary and the secondary sides of the IPT transformer are coupled, and is given by:

$$k = \frac{M}{\sqrt{L_1 L_2}} \tag{77}$$

As it can be seen from the characteristic shown below, the coupling factor k affects the bandwidth of the converter.

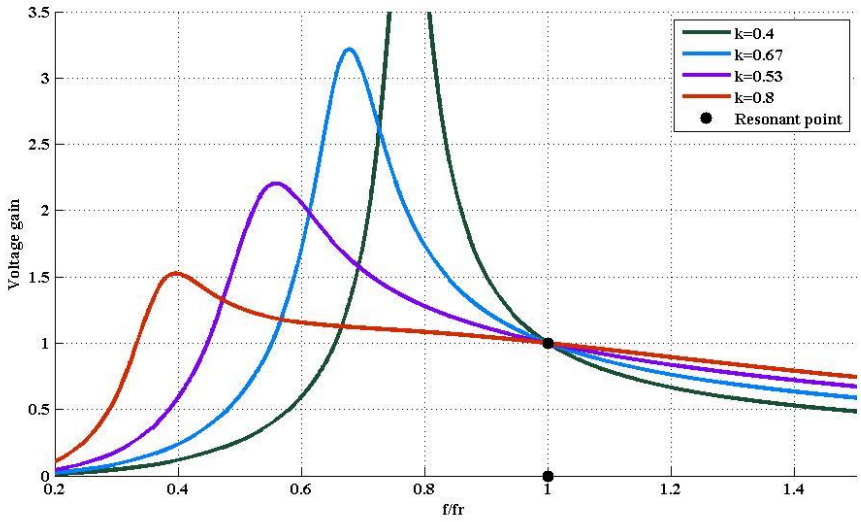

Figure 4-VIII Transfer characteristic for different coupling factor values

As it can be easily realized by the above presented characteristics, the output of the converter can be controlled by controlling the frequency. The problem that arises is that for the case of wireless charging of electric vehicles the factors Q and k will change from case to case. Every car is going to constitute a different load and the coupling achieved will never be identical to any other, as it depends on the relative position of the vehicle, which is random. In order to overcome these difficulties, the suitable way to operate the converter is to continuously try to operate at the primary resonant frequency f_r. Operation at the primary resonant frequency f_r results in a unity gain, regardless of the load connected or the coupling that has been achieved, so it gives the opportunity to control the output voltage under any circumstances and conditions. [13, 14, 14, 15, 15–20]

4.4. Half bridge configuration-FHA model

The IPT transformer of a wireless power transfer system, can also be utilized using a half bridge configuration, as depicted below. It has a structure of two

symmetric half bridges, one for the primary inverting stage and one for the secondary rectifying stage, with a symmetric Inductive Power Transfer high frequency transformer between them. Power switches in the primary inverting stage convert power from dc to ac, in order to transfer it through the transformer, which is modeled with the magnetizing inductance Lm and the transformer's turn ratio of 1:1. The leakage inductance of the primary and secondary windings of the transformer is merged to the resonant inductors Lr1 and Lr2 respectively. The resonant capacitors Cr1 and Cr2 make automatic flux balancing with Lr1 and Lr2 at high resonant frequency.

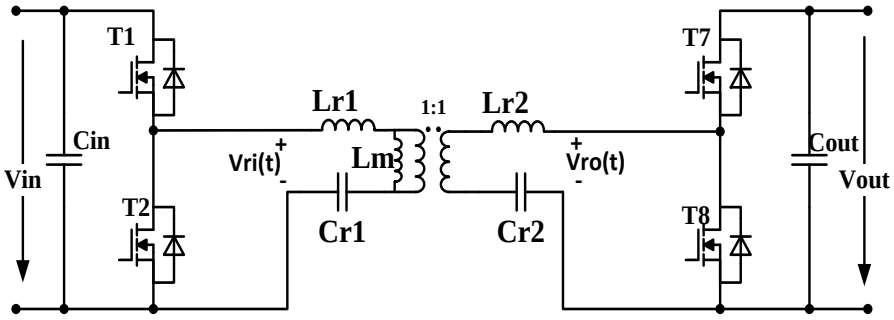

Figure 4-IX Half Bridge CLLC resonant converter

The switching scheme that is suitable for the resonant converter is a 50% duty cycle for each switch of the half bridge leg. The output $V_{ri}(t)$ of the half bridge in the primary side of the Wireless Power Transfer converter is

$$V_{ri}(t)=\begin{cases}0,\ for-\pi\le\omega t\le 0\\ V_d,\ for\ 0\le\omega t\le\pi\end{cases} \tag{78}$$

The fundamental harmonic component of this voltage is $u_{ri,FHA}(t)$

$$u_{ri,FHA}(t)=\frac{2}{\pi}\cdot V_d\cdot\sin(2\pi f_s\cdot t) \tag{79}$$

The rms value of $u_{ri,FHA}(t)$ is $V_{ri,FHA}$

$$V_{ri,FHA}=\frac{\sqrt{2}}{\pi}\cdot V_d \tag{80}$$

The input $V_{ro}(t)$ of the output rectifier in the secondary side of the Wireless Power Transfer converter is

$$V_{ro}(t)=\begin{cases}0,\ for-\pi\le\omega t\le 0\\ V_o,\ for\,0\le\omega t\le\pi\end{cases} \tag{81}$$

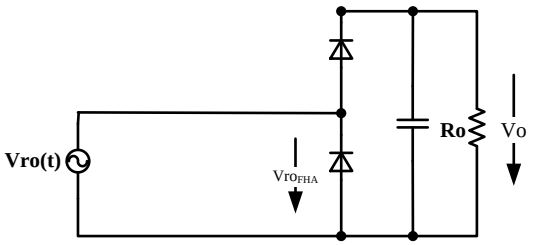

Figure 4-X Output diode for half-bridge configuration

The fundamental harmonic component of this voltage is $u_{ro,FHA}(t)$:

$$u_{ro,FHA}(t)=\frac{2}{\pi}\cdot V_o\cdot\sin\left(2\pi f_s\cdot t-\varphi\right) \tag{82}$$

the rms value of $u_{ro,FHA}(t)$ is $V_{ro,FHA}$:

$$V_{ro,FHA}=\frac{2\sqrt{2}}{\pi}\cdot V_o \tag{83}$$

For the rectifier current $i_{rct,FHA}(t)$,we have:

$$i_{rct,FHA}(t)=\sqrt{2}\cdot I_{rct,FHA}\cdot\sin\left(2\pi f_s\cdot t-\varphi\right) \tag{84}$$

Where $I_{rct,FHA}$ is the rms value of the fundamental harmonic component of the rectifier current.

The average value output current I_o is given by:

$$I_o=\frac{1}{T_s}\int_0^{T_s}\left|i_{rct,FHA}(t)\right|dt=\frac{\sqrt{2}}{\pi}\cdot I_{rct,FHA} \tag{85}$$

$u_{ro,FHA}(t)$ and $i_{rct,FHA}(t)$ are in phase, so the resistive load of the resonant network $R_{o,e}$ can be given by the ratio of the instantaneous voltage and current:

$$R_{o,e}=\frac{u_{ro,FHA}(t)}{i_{rct,FHA}(t)}=\frac{2}{\pi^2}R_o \tag{86}$$

The FHA equivalent model of the bidirectional LLC converter is presented again below:

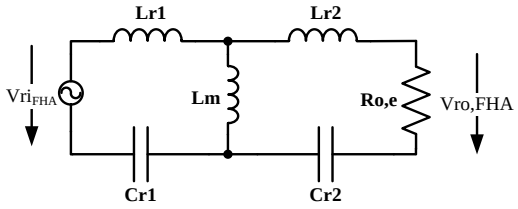

Figure 4-XI FHA equivalent model of the bidirectional CLLC converter

$$\frac{V_{ro,FHA}}{V_{ri,FHA}} = \frac{L_m // \left(\boldsymbol{j\omega} \cdot L_{r2} + R_{o,e} + \frac{1}{\boldsymbol{j\omega} \cdot C_{r2}} \right)}{\frac{1}{\boldsymbol{j\omega} \cdot C_{r1}} + \boldsymbol{j\omega} \cdot L_{r1} + \left[L_m // \left(\boldsymbol{j\omega} \cdot L_{r2} + R_{o,e} + \frac{1}{\boldsymbol{j\omega} \cdot C_{r2}} \right) \right]} \cdot \frac{R_{o,e}}{\boldsymbol{j\omega} \cdot L_{r2} + R_{o,e} + \frac{1}{\boldsymbol{j\omega} \cdot C_{r2}}}$$

$$\frac{V_o}{V_d} = \frac{L_m // \left(\boldsymbol{j\omega} \cdot L_{r2} + \frac{2}{\pi^2} R_o + \frac{1}{\boldsymbol{j\omega} \cdot C_{r2}} \right)}{\frac{1}{\boldsymbol{j\omega} \cdot C_{r1}} + \boldsymbol{j\omega} \cdot L_{r1} + \left[L_m // \left(\boldsymbol{j\omega} \cdot L_{r2} + \frac{2}{\pi^2} R_o + \frac{1}{\boldsymbol{j\omega} \cdot C_{r2}} \right) \right]} \cdot \frac{\frac{2}{\pi^2} R_o}{\boldsymbol{j\omega} \cdot L_{r2} + \frac{2}{\pi^2} R_o + \frac{1}{\boldsymbol{j\omega} \cdot C_{r2}}} \quad (87)$$

This transfer function leads to the following transfer characteristic:

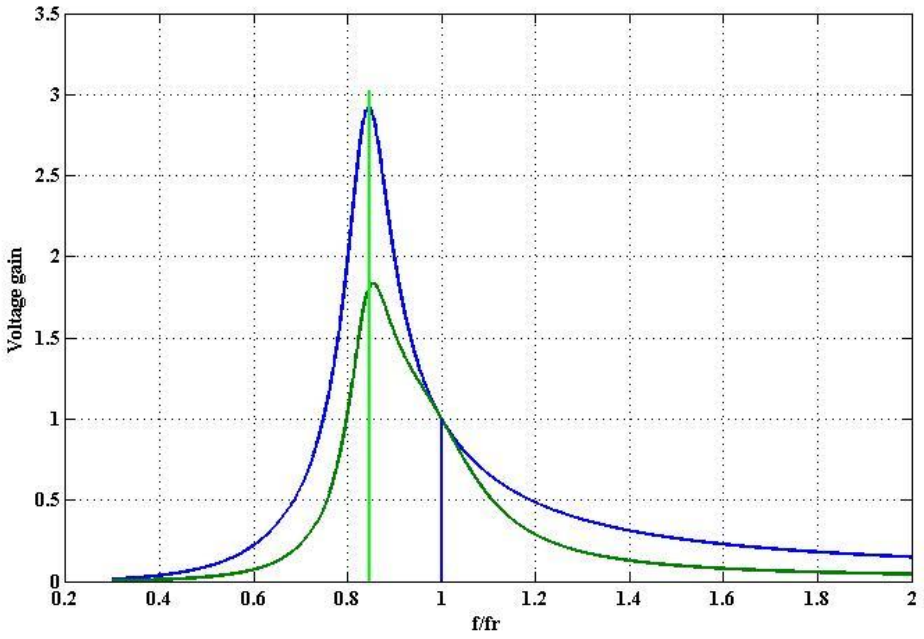

The dependence on the quality factor Q and the coupling factor k, is similar to the dependence of the full bridge configuration on these two factors. The First Harmonic Approximation models analyzed above, show that it is necessary to always

try to operate the system at the primary resonant frequency, in order to ensure controllability.

Full bridge configuration

4.5. Zero Voltage Switching

The input voltage of the system is 400V DC. The advantage of this topology is that it allows the switches to turn-on under Zero Voltage Switching (ZVS) Conditions. The initial currents that flow through a MOSFET during the turn on and turn off process are first utilized for the discharging and charging of the capacitances between the Drain and the Source of the MOSFET, respectively. The charging and discharging process of a single bridge leg is depicted below:

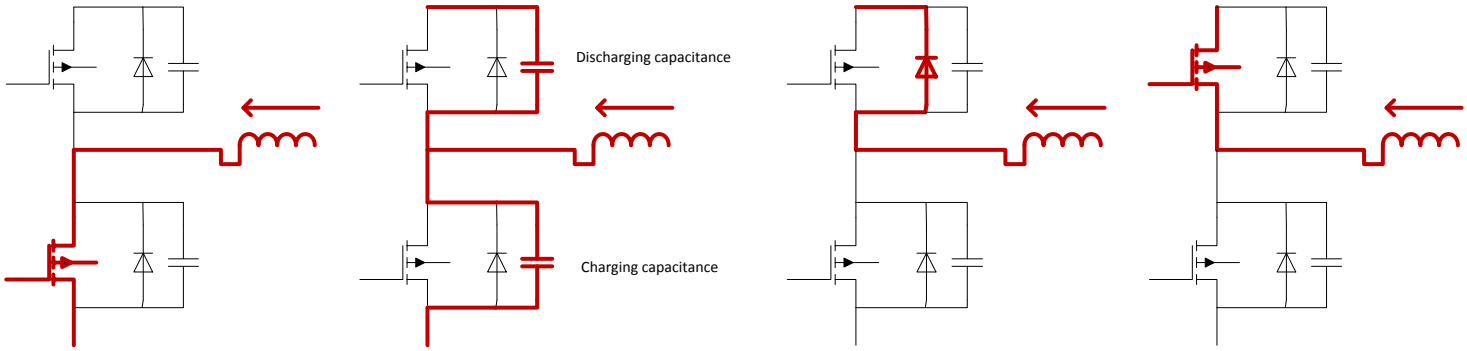

Figure 4-XII Charging and discharging process of a single bridge leg

During the dead time duration, while none of the switches is on, the primary current charges the output capacitance of the primary switches T_2 and T_3, and discharges the output capacitance of T_1 and T_4. After the charge and discharge processes, the primary current will pass through the antiparallel diode of T_1 and T_4, which makes the switches operate under the ZVS condition. The operation of the primary power MOSFETs is one of the most significant factors for the optimal efficient design of the bidirectional full-bridge CLLC resonant converter. The primary current is always negative during the dead time before the turn on of the T_1 and T_4 switches, so it flows through their antiparallel diodes, a fact which creates the conditions for Zero Voltage Switching ZVS. Similarly, the switches T_2 and T_3 turn on under the Zero Voltage Switching ZVS condition because of the positive direction of the primary current (through their antiparallel diodes) during the dead time before their turn on. Therefore, the primary current should discharge the output capacitance of four primary switches within the dead time interval, in order to ensure their Zero Voltage Switching (ZVS) turn-on. This clearly means that the ZVS condition of the

switches depends highly on the magnetizing inductance Lm and the dead-time duration t_{dead}.

$$t_{dead} \geq \frac{4V_d C_{Si}}{i_p} \Rightarrow t_{dead} \geq 16 C_{Si}\ f_r L_m \quad (88)$$

A small value of L_m can guarantee the ZVS of the primary switches. However, an extremely small value of L_m significantly increases the conduction losses of the primary power MOSFETs and diodes of the output rectifier in the secondary side. [17]

4.6. Theoretical simulations and waveforms

The theoretical simulations and waveforms of the converter under heavy load conditions, show clearly the ZVS, that leads to good performance regarding efficiency. Below, there is an analysis of the operation of the converter for three cases of operation, one below the primary resonant frequency (between the two resonant frequencies), one at the primary resonant frequency and one above.

The stages for operation below the primary resonant frequency are depicted below. We can easily observe that the Zero Voltage transmission is achieved.

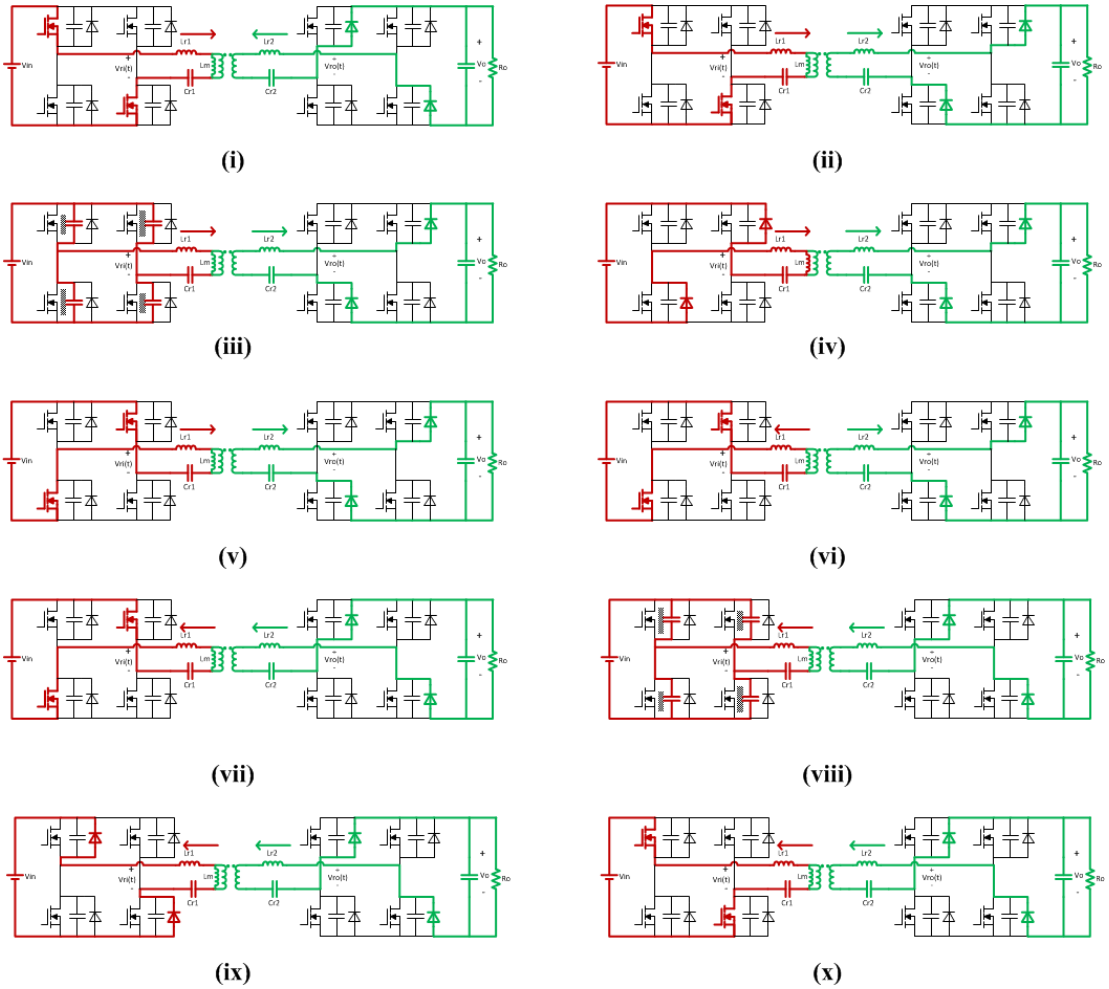

Figure 4-XIII Operation below the primary resonant frequency – ZVS

The most important waveforms are depicted below:

Figure 4-XIV Operation below the primary resonant frequency - Waveforms

The stages for operation at the primary resonant frequency are depicted below. We can easily observe that the Zero Voltage transmission is achieved.

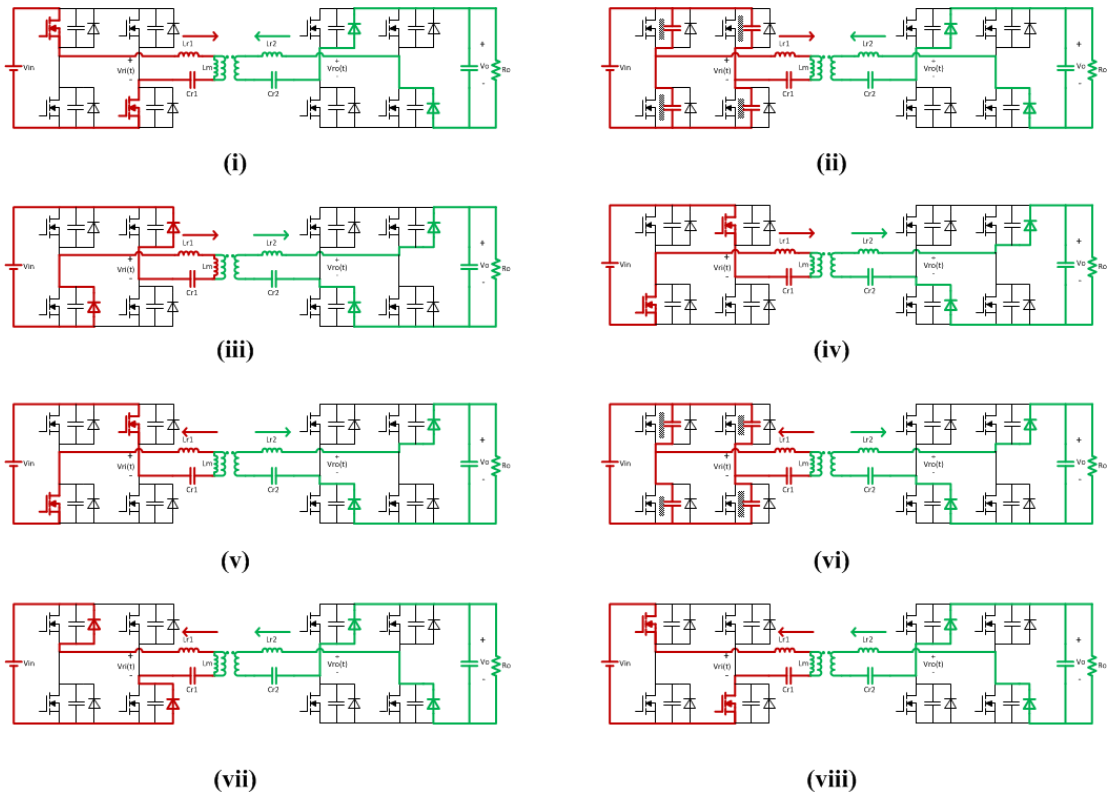

Figure 4-XV Operation at the primary resonant frequency – ZVS

The most important waveforms are depicted below:

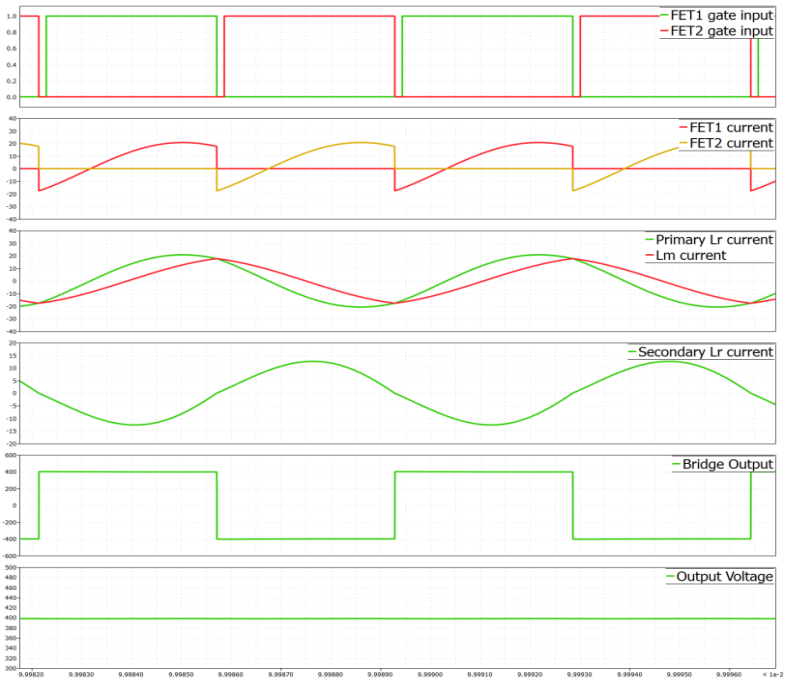

Figure 4-XVI Operation at the primary resonant frequency - Waveforms

The stages for operation above the primary resonant frequency are depicted below. We can easily observe that the Zero Voltage transmission is achieved.

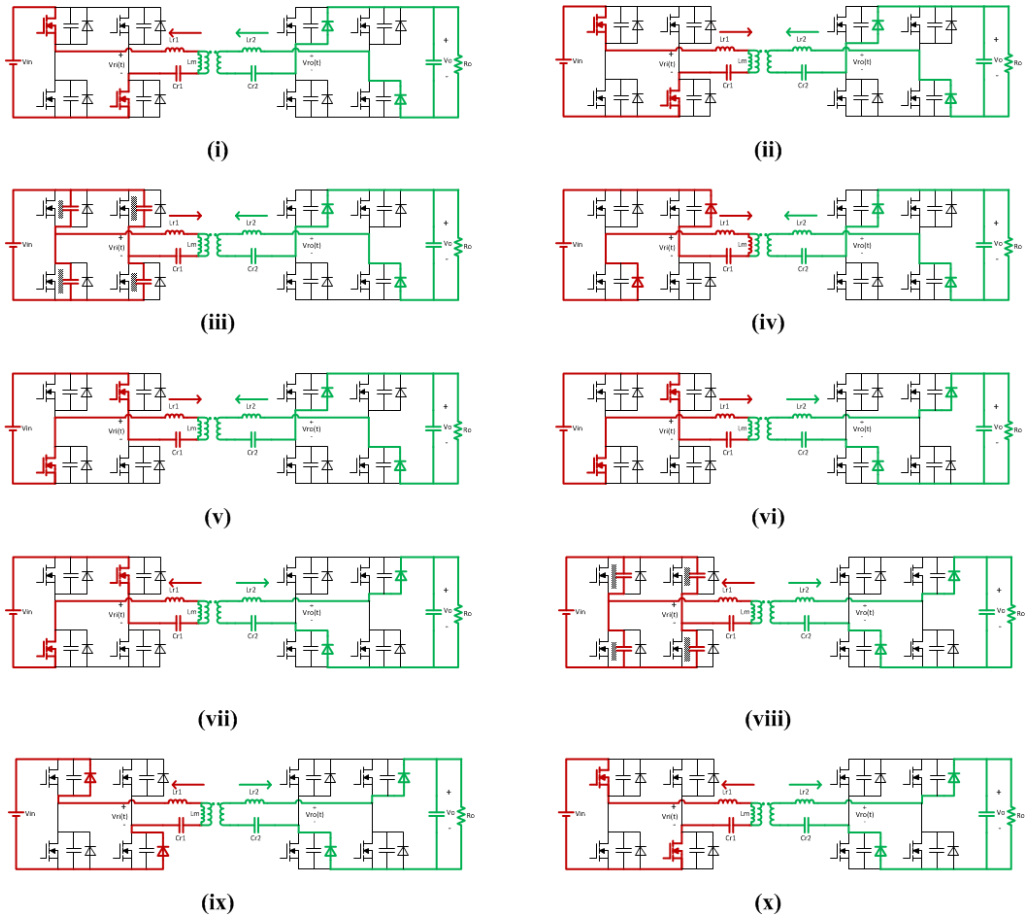

Figure 4-XVII Operation above the primary resonant frequency – ZVS

The most important waveforms are depicted below:

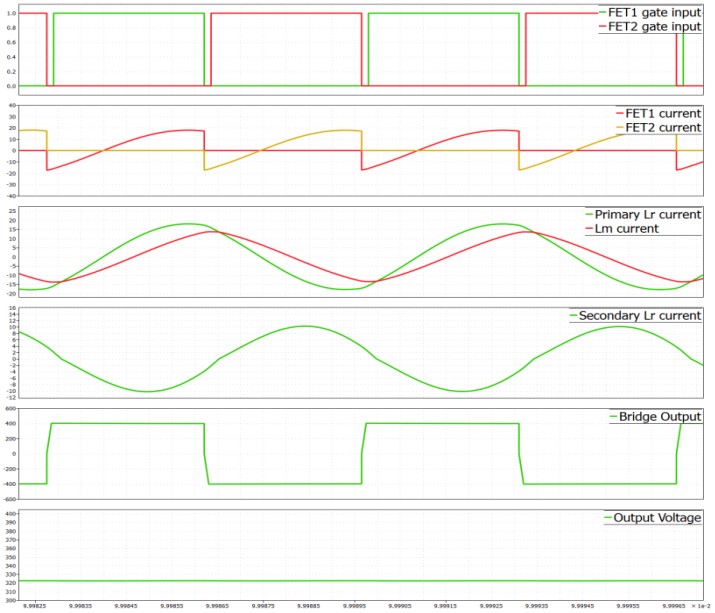

Figure 4-XVIII Operation above the primary resonant frequency - Waveforms

4.7. Theoretical calculations

The waveforms of the currents that flow in the circuit at the resonant frequency are depicted below:

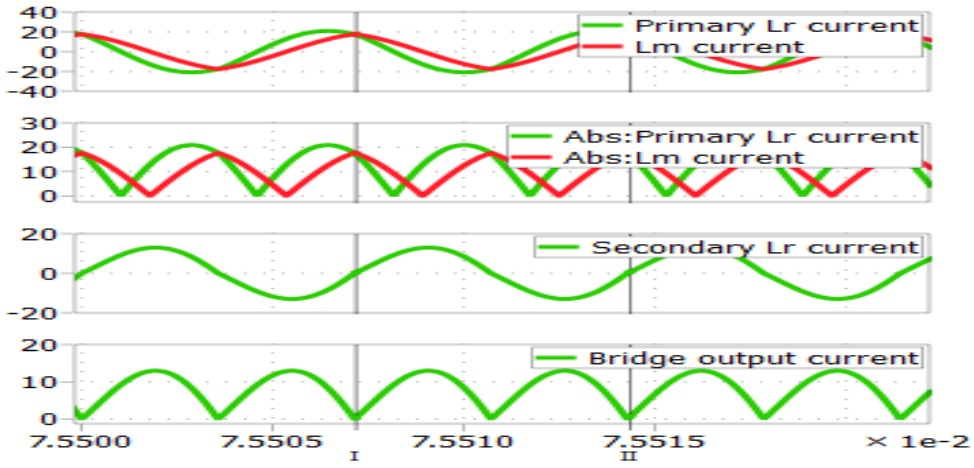

Figure 4-XIX Waveforms of the currents at the resonant frequency

$$i_m(t)=\begin{cases}\dfrac{V_o T_s}{4L_m}-\dfrac{V_o}{L_m}t,\ for\ 0\le t\le \dfrac{T_s}{2}\\ -\dfrac{V_o T_s}{4L_m}+\dfrac{V_o}{L_m}\left(t-\dfrac{T_s}{2}\right),\ for\ \dfrac{T_s}{2}\le t\le T_s\end{cases} \tag{89}$$

The rms value I_m of the magnetizing current $i_m(t)$ is given by:

$$I_m = \sqrt{\frac{2}{T_s} \cdot \int_0^{\frac{T_S}{2}} i_m^2(t)\,dt} \Rightarrow I_m = \frac{1}{\sqrt{48}} \cdot \frac{V_o T_s}{L_m} \tag{90}$$

By making the assumption that the forward voltage drop of the diodes and that the dead time is negligible in respect to the duration of a period we can reform the primary current $i_p(t)$ to: [17] [16]

$$i_p(t) = \sqrt{2} I_p \sin(2\pi f_r t + \varphi) \tag{91}$$

Where I_p is the rms value of the primary current $i_p(t)$ and the phase angle φ is given by:

$$\varphi = \sin^{-1}\left(\frac{V_o T_s}{4\sqrt{2} L_m I_p}\right) \tag{92}$$

The secondary current $i_s(t)$ is given by:

$$i_s(t) = i_p(t) - i_m(t) \tag{93}$$

From the waveforms it can easily be seen

$$\left|i_p(t) - i_m(t)\right| = \begin{cases} -\left(i_p(t) - i_m(t)\right), \text{ for } 0 \le t \le \frac{T_s}{2} \\ i_p(t) - i_m(t), \text{ for } \frac{T_s}{2} \le t \le T_s \end{cases} \tag{94}$$

The average output current I_o is given by the rectified waveform of $i_s(t)$:

$$I_o = \frac{P_{out}}{V_o} = \frac{V_o}{R_o} = \frac{1}{T_s} \int_0^{T_s} \left|i_s(t)\right| dt \tag{95}$$

By combining all the above, the rms value of the primary current $i_p(t)$ can be calculated:

$$i_s(t) = i_p(t) - i_m(t) \Rightarrow \left|i_s(t)\right| = \left|i_p(t) - i_m(t)\right| \Rightarrow I_p = \sqrt{\frac{\pi^2 V_o^2}{8R_o^2} + \frac{V_o^2 T_s^2}{32 L_m^2}} \tag{96}$$

The secondary current $i_s(t)$ is given by:

$$i_s(t) = i_p(t) - i_m(t) \tag{97}$$

The rms value of the secondary current $i_s(t)$ is I_s and is given by:

$$I_s = \sqrt{\frac{2}{T_s}\cdot\int_0^{\frac{T_S}{2}} i_s^2(t)\,dt} = \sqrt{\frac{2}{T_s}\cdot\int_0^{\frac{T_S}{2}} \left(\mathrm{i_p(t)} - i_m(t)\right)^2 dt} \Rightarrow$$
$$I_s^2 = I_p^2 + I_m^2 - \frac{2\sqrt{2}\mathrm{I_p}V_o}{\omega L_m}cos\varphi + \frac{2\sqrt{2}\mathrm{I_p}}{\pi}\frac{V_o}{\omega L_m}\cdot\left(\pi cos\varphi - 2sin\varphi\right) \quad (98)$$

The current flowing through the primary leakage inductance Lr_1 , which serves as resonant inductance of the resonant tank is $i_p(t)$.

The voltage $v_{Lr_1}(t)$ across it is given by:

$$v_{Lr_p}(t) = Lr_1\cdot\frac{di_p(t)}{dt} = \sqrt{2}\mathrm{I_p}Lr_1\cdot\omega\cos\left(\omega t + \varphi\right) \quad (99)$$

The rms value V_{Lr_p} of the voltage $v_{Lr_p}(t)$ is:

$$V_{Lr_1} = X_{Lr_p}\cdot I_p = \left(\omega Lr_1\right)\cdot I_p \quad (100)$$

The same current $i_p(t)$. is the current of the resonant capacitor Cr_1

The voltage $v_{Cr_1}(t)$ across the capacitor is

$$i_p(t) = Cr_1\cdot\frac{dv_{Cr_1}(t)}{dt} \Rightarrow v_{Cr_1}(t) = \frac{1}{Cr_1}\int_0^t i_p(t)\,dt + v_{Cr_1}(0) \Rightarrow$$
$$v_{Cr_1}(t) = \frac{\sqrt{2}\mathrm{I_p}}{\omega Cr_1}\cdot\left[-cos\left(\omega t + \varphi\right) + cos\varphi\right] + v_{Cr_1}(0) \quad (101)$$

The rms value V_{Cr_1} of the voltage $v_{Cr_1}(t)$ is:

$$V_{Cr_1} = X_{Cr_1}\cdot I_p = \frac{1}{\omega Cr_1}\cdot I_p \quad (102)$$

The current flowing through the secondary leakage inductance Lr_2 , which serves as resonant inductance of the resonant tank is $i_s(t)$.

The voltage $v_{Lr_2}(t)$ across it is given by:

$$v_{Lr_2}(t) = Lr_2 \cdot \frac{di_s(t)}{dt} \Rightarrow v_{Lr_2}(t) = Lr_2 \cdot \frac{d\mathrm{i_p(t)}}{dt} - Lr_2 \cdot \frac{di_m(t)}{dt} \Rightarrow$$

$$v_{Lr_2}(t) = \sqrt{2}\mathrm{I_p} Lr_2 \cdot \omega \cos(\omega \mathrm{t} + \varphi) - Lr_2 \cdot \frac{di_m(t)}{dt} \Rightarrow \quad (103)$$

$$v_{Lr_2}(t) = \begin{cases} \sqrt{2}\mathrm{I_p} Lr_2 \cdot \omega \cos(\omega \mathrm{t} + \varphi) + Lr_2 \cdot \frac{V_o}{L_m}, \; for \; 0 \le t \le \frac{\mathrm{T_s}}{2} \\ \sqrt{2}\mathrm{I_p} Lr_2 \cdot \omega cos(\omega t + \varphi) - Lr_2 \cdot \frac{V_o}{L_m}, \; for \; \frac{\mathrm{T_s}}{2} \le t \le \mathrm{T_s} \end{cases}$$

The rms value V_{Lr_2} of the voltage $v_{Lr_2}(t)$ can be estimated by:

$$V_{Lr_2} = X_{Lr_2} \cdot I_s = (\omega Lr_2) \cdot I_s \quad (104)$$

The same current $i_s(t)$. is the current of the resonant capacitor Cr_2.

The voltage $v_{Cr_2}(t)$ across the capacitor is

$$v_{Cr_2}(t) = \begin{cases} \frac{1}{Cr_2} \int_0^t \left(\mathrm{i_p(t)} - \frac{V_o T_s}{4L_m} + \frac{V_o}{L_m} t \right) dt + v_{Cr_2}(0), \; for \; 0 \le t \le \frac{\mathrm{T_s}}{2} \\ \frac{1}{Cr_2} \int_0^{\frac{\mathrm{T_s}}{2}} \left(\mathrm{i_p(t)} - \frac{V_o T_s}{4L_m} + \frac{V_o}{L_m} t \right) dt + \frac{1}{Cr_2} \int_{\frac{\mathrm{T_s}}{2}}^t \left(\mathrm{i_p(t)} + \frac{V_o T_s}{4L_m} - \frac{V_o}{L_m} t \right) dt + v_{Cr_2}(0), \; for \; \frac{\mathrm{T_s}}{2} \le t \le \mathrm{T_s} \end{cases} \quad (105)$$

The rms value V_{Cr_2} of the voltage $v_{Cr_2}(t)$ can be estimated by:

$$V_{Cr_2} = X_{Cr_2} \cdot I_s = \frac{1}{\omega Cr_2} \cdot I_s \quad (106)$$

The expected currents through the leakage inductances and the expected voltages across the resonant capacitors are simulated below:

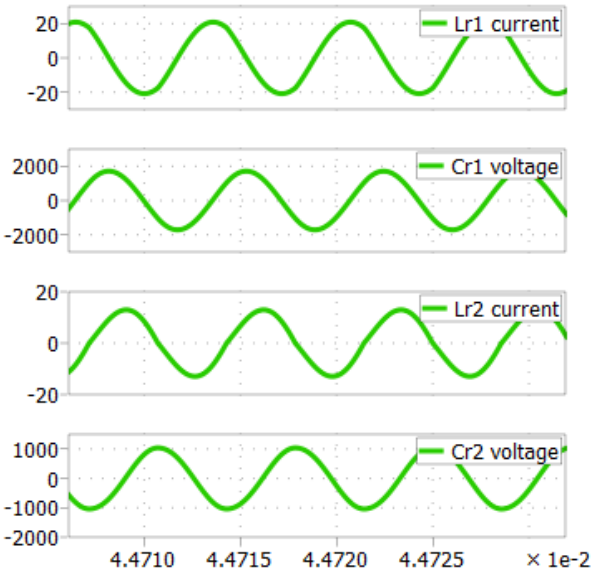

Figure 4-XX Currents through leakage inductances and voltages across resonant capacitors

All the detailed calculations can be found in the appendix.

4.8. Currents through primary MOSFETs

The currents that flow through the MOSFETs of a single leg of the primary Full-Bridge are presented below:

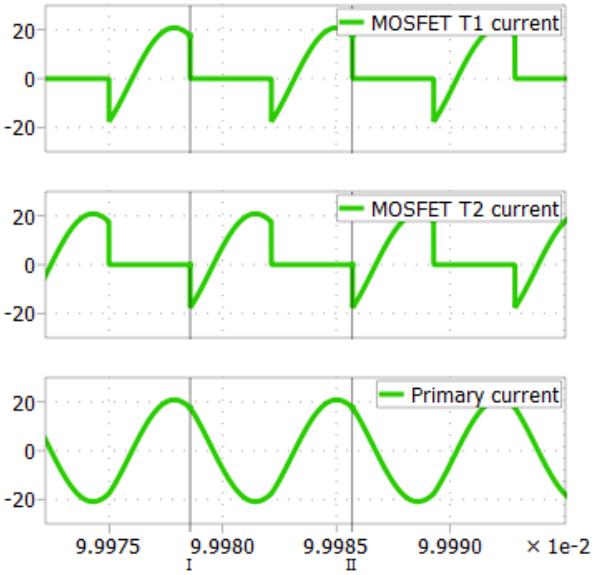

Figure 4-XXI Currents through the MOSFETs of a full bridge single leg

The current flowing through the MOSFETs T_1 and T_4 is:

$$i_{T1,4}(t)=\begin{cases} 0,\ for\ 0\le t\le \dfrac{T_s}{2} \\ i_p(t),\ for\ \dfrac{T_s}{2}\le t\le T_s \end{cases} \tag{107}$$

The current flowing through the MOSFETs T_2 and T_3 is:

$$i_{T2,3}(t)=\begin{cases} -i_p(t),\ for\ 0\le t\le \dfrac{T_s}{2} \\ 0,\ for\ \dfrac{T_s}{2}\le t\le T_s \end{cases} \tag{108}$$

The rms value of the currents $i_{T1,4}(t)$ and $i_{T2,3}(t)$ is I_S and is given by:

$$I_{sw}=\sqrt{\frac{1}{T_s}\cdot\int_0^{T_s} i_{T2,3}^2(t)\,dt}=\sqrt{\frac{1}{T_s}\cdot\int_0^{\frac{T_s}{2}} i_p^2(t)\,dt}=\frac{1}{\sqrt{2}}\cdot\sqrt{\frac{2}{T_s}\cdot\int_0^{\frac{T_s}{2}} i_p^2(t)\,dt}=\frac{I_p}{\sqrt{2}} \tag{109}$$

4.9. Currents through secondary rectifier

The currents that flow through the diodes of the secondary rectifier bridge are presented below:

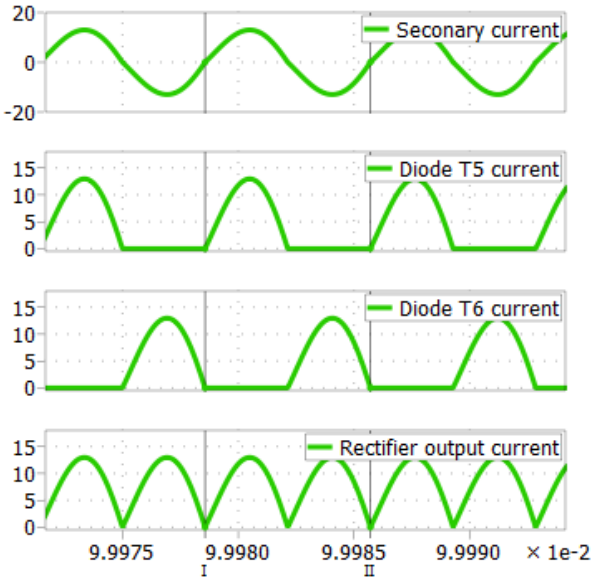

Figure 4-XXII Currents through the diodes of the secondary rectifier bridge

The current flowing through the diodes T_5 and T_8 is:

$$\mathrm{i}_{\mathrm{D5,8}}(\mathrm{t}) = \begin{cases} i_s(t),\ for\ 0 \le t \le \dfrac{\mathrm{T_s}}{2} \\ 0,\ for\ \dfrac{\mathrm{T_s}}{2} \le t \le \mathrm{T_s} \end{cases} \tag{110}$$

The current flowing through the diodes T_6 and T_7 is:

$$\mathrm{i}_{\mathrm{D6,7}}(\mathrm{t}) = \begin{cases} 0,\ for\ 0 \le t \le \dfrac{\mathrm{T_s}}{2} \\ -i_s(t),\ for\ \dfrac{\mathrm{T_s}}{2} \le t \le \mathrm{T_s} \end{cases} \tag{111}$$

The rms value of the currents $\mathrm{i}_{\mathrm{D5,8}}(\mathrm{t})$ and $\mathrm{i}_{\mathrm{D6,7}}(\mathrm{t})$ is I_D and is given by:

$$I_D = \sqrt{\frac{1}{T_s}\cdot\int_0^{T_s}\mathrm{i}_{\mathrm{D5,8}}^2(t)\,dt} = \sqrt{\frac{1}{T_s}\cdot\int_0^{\frac{T_s}{2}} i_s^2(t)\,dt} = \frac{1}{\sqrt{2}}\cdot\sqrt{\frac{2}{T_s}\cdot\int_0^{\frac{T_s}{2}} i_s^2(t)\,dt} = \frac{I_s}{\sqrt{2}} \tag{112}$$

The mean value of each of the currents $\mathrm{i}_{\mathrm{D5,8}}(\mathrm{t})$ and $\mathrm{i}_{\mathrm{D6,7}}(\mathrm{t})$ is $\overline{I_D}$ and is given by:

$$\overline{I_D} = \frac{1}{T_s}\cdot\int_0^{T_s}\mathrm{i}_{\mathrm{D5,8}}(\mathrm{t})\,dt = \frac{1}{T_s}\cdot\int_0^{\frac{T_s}{2}} i_s(t)\,dt = \frac{I_o}{2} = \frac{V_o}{2R_o} \tag{113}$$

Half bridge configuration

4.10. Theoretical calculations

The waveforms of the currents that flow in the circuit at the resonant frequency are depicted below:

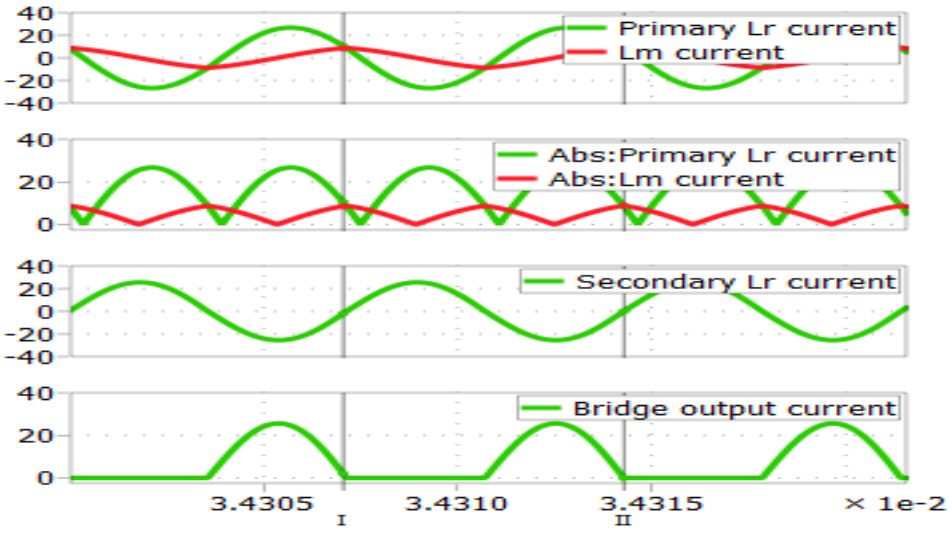

Figure 4-XXIII Waveforms of the currents at the resonant frequency

The magnetizing inductance L_m is always clamped at the input voltage of the secondary rectifier bridge. The magnetizing current $i_m(t)$, which flows through the magnetizing inductance L_m in the equivalent circuit is:

$$i_m(t)=\begin{cases}\dfrac{V_o T_s}{8L_m}-\dfrac{V_o}{2L_m}t,\ for\ 0\le t\le \dfrac{T_s}{2}\\ -\dfrac{V_o T_s}{8L_m}+\dfrac{V_o}{2L_m}\left(t-\dfrac{T_s}{2}\right),\ for\ \dfrac{T_s}{2}\le t\le T_s\end{cases} \tag{114}$$

The rms value I_m of the magnetizing current $i_m(t)$ is given by:

$$I_m=\sqrt{\frac{2}{T_s}\cdot\int_0^{\frac{T_s}{2}} i_m^2(t)\,dt}\Rightarrow I_m=\frac{1}{2\sqrt{48}}\cdot\frac{V_o T_s}{L_m} \tag{115}$$

By making the assumption that the forward voltage drop of the diodes and that the dead time is negligible in respect to the duration of a period we can reform the primary current $i_p(t)$ to:

$$i_p(t)=\sqrt{2}I_p\sin(2\pi f_r t+\varphi) \tag{116}$$

Where I_p is the rms value of the primary current $i_p(t)$ and the phase angle φ is given by:

$$\varphi = \sin^{-1}\left(\frac{V_o T_s}{8\sqrt{2} L_m I_p}\right) \tag{117}$$

The secondary current $i_s(t)$ is given by:

$$i_s(t) = i_p(t) - i_m(t) \tag{118}$$

From the waveforms it can easily be seen

$$\left|i_p(t) - i_m(t)\right| = \begin{cases} -\left(i_p(t) - i_m(t)\right), \; for \; 0 \le t \le \dfrac{T_s}{2} \\ i_p(t) - i_m(t), \; for \; \dfrac{T_s}{2} \le t \le T_s \end{cases} \tag{119}$$

The average output current I_o is given by the rectified waveform of $i_s(t)$:

$$I_o = \frac{P_{out}}{V_o} = \frac{V_o}{R_o} = \frac{1}{T_s}\int_0^{T_s} \left|i_s(t)\right| dt \tag{120}$$

By combining all the above, the rms value of the primary current $i_p(t)$ can be calculated:

$$i_s(t) = i_p(t) - i_m(t) \Rightarrow \left|i_s(t)\right| = \left|i_p(t) - i_m(t)\right| \Rightarrow I_p = \sqrt{\frac{\pi^2 V_o^2}{2R_o^2} + \frac{V_o^2 T_s^2}{128 L_m^2}} \tag{121}$$

The secondary current $i_s(t)$ is given by:

$$i_s(t) = i_p(t) - i_m(t) \tag{122}$$

The rms value of the secondary current $i_s(t)$ is I_s and is given by:

$$\begin{aligned} I_s &= \sqrt{\frac{2}{T_s} \cdot \int_0^{\frac{T_S}{2}} i_s^2(t)\, dt} = \sqrt{\frac{2}{T_s} \cdot \int_0^{\frac{T_S}{2}} \left(i_p(t) - i_m(t)\right)^2 dt} \Rightarrow \\ I_s^2 &= I_p^2 + I_m^2 - \frac{\sqrt{2} I_p V_o}{\omega L_m} cos\varphi + \frac{\sqrt{2} I_p}{\pi} \frac{V_o}{\omega L_m} \cdot \left(\pi cos\varphi - 2 sin\varphi\right) \end{aligned} \tag{123}$$

The expected currents through the leakage inductances and the expected voltages across the resonant capacitors are simulated below:

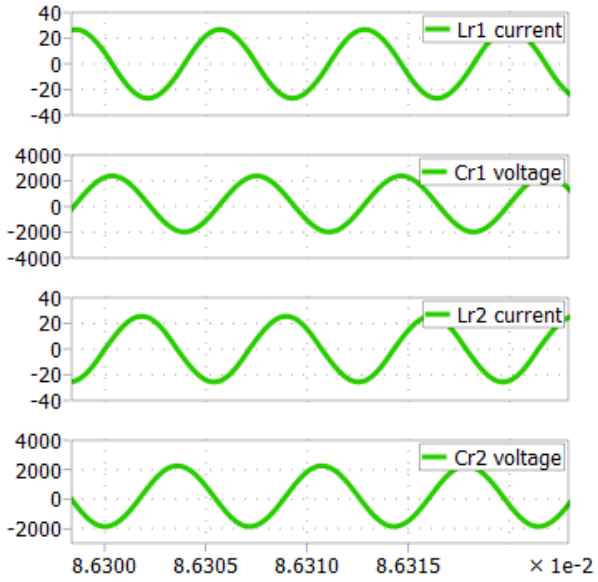

Figure 4-XXIV Currents through leakage inductances and voltages across resonant capacitors

All the detailed calculations can be found in the appendix.

4.11. Currents through primary MOSFETs

The currents that flow through the MOSFETs the primary Half-Bridge are presented below:

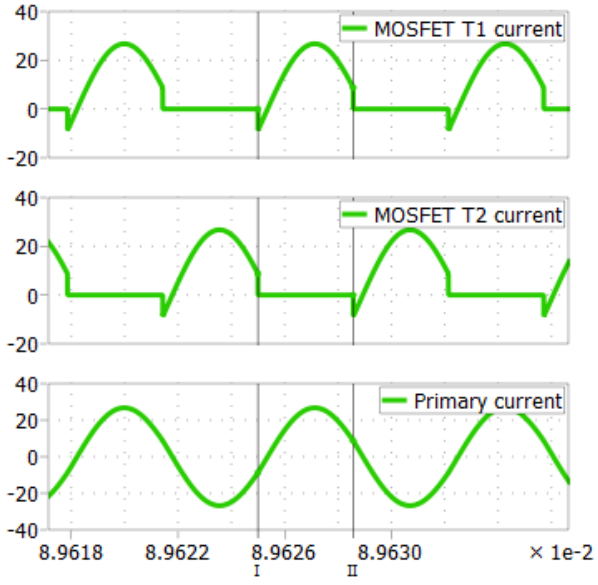

Figure 4-XXV Currents through the MOSFETs of a full bridge single leg

The current flowing through the MOSFET T_1 is:

$$i_{T1}(t)=\begin{cases}0,\ for\ 0\le t\le \dfrac{T_s}{2}\\ i_p(t),\ for\ \dfrac{T_s}{2}\le t\le T_s\end{cases} \tag{124}$$

The current flowing through the MOSFET T_2 is:

$$i_{T2}(t)=\begin{cases}-i_p(t),\ for\ 0\le t\le \dfrac{T_s}{2}\\ 0,\ for\ \dfrac{T_s}{2}\le t\le T_s\end{cases} \tag{125}$$

The rms value of the currents $i_{T1}(t)$ and $i_{T2}(t)$ is I_S and is given by:

$$I_{sw}=\sqrt{\frac{1}{T_s}\cdot\int_0^{T_s} i_{T2}^2(t)\,dt}=\sqrt{\frac{1}{T_s}\cdot\int_0^{\frac{T_s}{2}} i_p^2(t)\,dt}=\frac{1}{\sqrt{2}}\cdot\sqrt{\frac{2}{T_s}\cdot\int_0^{\frac{T_s}{2}} i_p^2(t)\,dt}=\frac{I_p}{\sqrt{2}} \tag{126}$$

4.12. Currents through secondary rectifier

The currents that flow through the diodes of the secondary rectifier bridge are presented below:

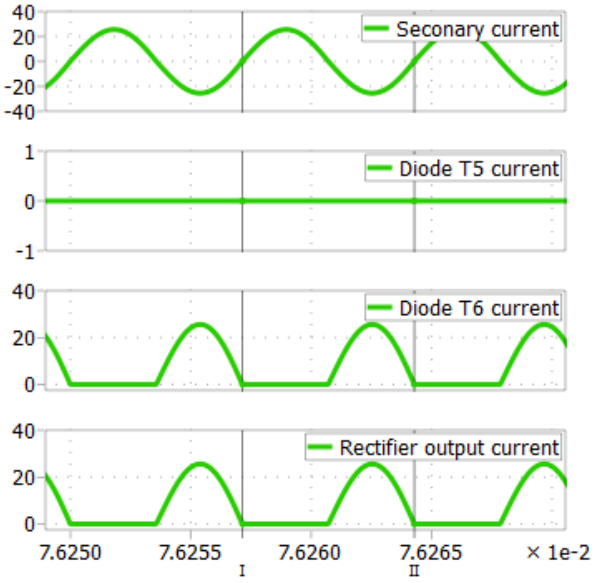

Figure 4-XXVI Currents through the diodes of the secondary rectifier bridge

The current flowing through the diode T_5 is:

$$\mathrm{i_{D5}(t)} = \begin{cases} 0,\ for\ 0 \le t \le \dfrac{\mathrm{T_s}}{2} \\ 0,\ for\ \dfrac{\mathrm{T_s}}{2} \le t \le \mathrm{T_s} \end{cases} \tag{127}$$

The current flowing through the diode T_6 is:

$$\mathrm{i_{D6}(t)} = \begin{cases} i_s(t),\ for\ 0 \le t \le \dfrac{\mathrm{T_s}}{2} \\ 0,\ for\ \dfrac{\mathrm{T_s}}{2} \le t \le \mathrm{T_s} \end{cases} \tag{128}$$

The rms value of the currents $\mathrm{i_{D5}(t)}$ is I_D and is given by:

$$I_D = \sqrt{\frac{1}{T_s} \cdot \int_0^{T_s} \mathrm{i_{D6}^2}(t)\,dt} = \sqrt{\frac{1}{T_s} \cdot \int_0^{\frac{T_s}{2}} i_s^2(t)\,dt} = \frac{1}{\sqrt{2}} \cdot \sqrt{\frac{2}{T_s} \cdot \int_0^{\frac{T_s}{2}} i_s^2(t)\,dt} = \frac{I_s}{\sqrt{2}} \tag{129}$$

The mean value of each of the currents $\mathrm{i_{D5,8}(t)}$ and $\mathrm{i_{D6,7}(t)}$ is $\overline{I_D}$ and is given by:

$$\overline{I_D} = \frac{1}{T_s} \cdot \int_0^{T_s} \mathrm{i_{D6}}(t)\,dt = \frac{1}{T_s} \cdot \int_0^{\frac{T_s}{2}} i_s(t)\,dt = I_o = \frac{V_o}{R_o} \tag{130}$$

5. Theoretical calculation of losses

5.1. Conduction losses of a power MOSFET

Conduction losses in power MOSFET can be calculated using a MOSFET-approximation with the drain-source on-state resistance $R_{DS_{on}}$:

$$U_{DS}\left(i_D\right) = R_{DS_{on}}\left(i_D\right) \cdot i_D \tag{131}$$

$U_{DS}$and i_D are the drain-source voltage and the drain current, respectively. The typical $R_{DS_{on}}$ can be read from the data-sheet diagrams. [21]

The instantaneous value of the MOSFET conduction losses is:

$$p_{CM}\left(t\right) = u_{DS}\left(t\right) \cdot i_D\left(t\right) = R_{DS_{on}} \cdot i_D^2\left(t\right) \tag{132}$$

Integration of the instantaneous power losses over the switching cycle gives an average value of the MOSFET conduction losses:

$$P_{CM} = \frac{1}{T_s} \cdot \int_0^{T_S} p_{CM}\left(t\right) dt = \frac{1}{T_s} \cdot \int_0^{T_S} R_{DS_{on}} \cdot i_D^2\left(t\right) dt = R_{DS_{on}} \cdot \frac{1}{T_s} \cdot \int_0^{T_S} i_D^2\left(t\right) dt = R_{DS_{on}} \cdot I_{D,rms}^2 \tag{133}$$

Where $I_{D,rms}$ is the rms value of the MOSFET on-state current.

The conduction losses of the anti-parallel diode can be estimated using a diode approximation with a series connection of DC voltage source U_{D0} representing diode on-state zero-current voltage and a diode on-state resistance R_D, $u_D$being the voltage across the diode and $i_F$the current through the diode:

$$u_D\left(i_F\right) = U_{D0} + R_D \cdot i_F \tag{134}$$

5.2. Switching losses of a power MOSFET

For the engineering calculations of the power loss balance, a linear approximation of the MOSFET switching process is sufficient and, as will be shown later, presents the worst case calculation. The idealised switching process of the power MOSFET is presented in the figure below. The uppermost part (A) presents the gate voltage (u_{GS}) and current (i_G); the next one (B) shows the drain-source voltage (u_{DS}) and the drain current (i_D) without taking the reverse recovery of the free-wheeling diode into account. The part C gives a qualitative overview of the power losses, while the part D shows the reverse-recovery effects on the switching losses.

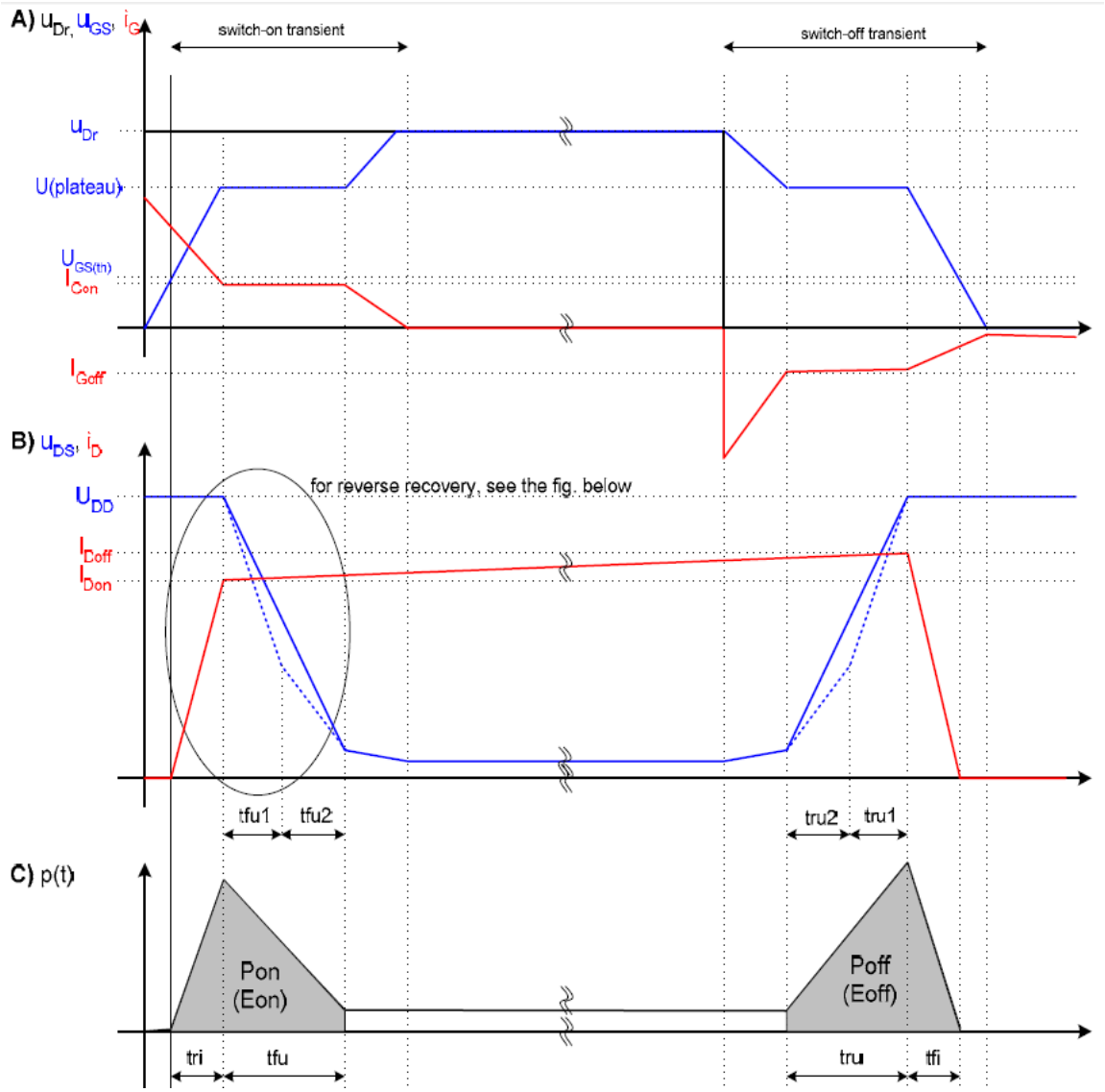

Figure 5-I Switch-on and Switch-off transients of a power MOSFET

Switch-on transient

Driver circuit changes its state from 0V to U_{Dr}, the gate voltage rises to the threshold voltage ($U_{GS(th)}$), with the time-constant defined by the gate resistor and the equivalent MOSFET input capacitance ($C_{iss} = C_{GD} + C_{GS}$). Until the gate voltage reaches the $U_{GS(th)}$, the output does not change.

After the $U_{GS(th)}$ has been reached, the drain current rises and takes over the load current. The worst case value of the current rise-time (t_{ri}) between zero and I_{Don} (defined by the application) can be read from the MOSFET data-sheet. During the current rise-time, the free-wheeling diode is still conducting and the drain-source voltage is U_{DD}.

In order for the diode to switch off, all the minority carriers stored in it have to be removed. This reverse-recovery current has to be absorbed by the circuit,

causing additional power losses. The worst-case values of the reverse-recovery charge (Q_{rr}) and duration (t_{rr}), which will be used in the power loss calculation, can again be read from the MOSFET data-sheet.

After the diode has been switched off, the drain-source voltage is falling from $u_{DS} = U_{DD}$ to its on-state value $u_{DS} = R_{DS_{on}} \cdot I_{on}$. The Miller effect takes place and the gate-source voltage is clamped at the $u_{GS} = U_{(plateau)}$. The slope of the drain-source voltage is dictated through the gate current flowing through the gate-drain capacitance ($C_{GD} = C_{rss}$). In order to calculate the voltage fall-time (t_{fu}) with a reasonable accuracy, the non-linearity of the gate-drain capacitance has to be taken into account. The typical dependence of the gate-drain capacitance on the drain-source voltage is shown in the datasheet of the MOSFET. Such non-linearity can not be easily incorporated into the engineering calculations. That is why a two-point approximation is used. It is supposed that if the drain-source voltage is in the range $u_{DS} \in \left[\frac{U_{DD}}{2}, U_{DD}\right]$, then the gate-drain capacitance takes value of $C_{GD1} = C_{GD}(U_{DD})$. On the other hand, if the drain-source voltage is in the range $u_{DS} \in \left[0V, \frac{U_{DD}}{2}\right]$, then the gate-drain capacitance takes the value of $C_{GD2} = C_{GD}(R_{DS_{on}} \cdot I_{on})$. The way to determine those capacitances is shown below:

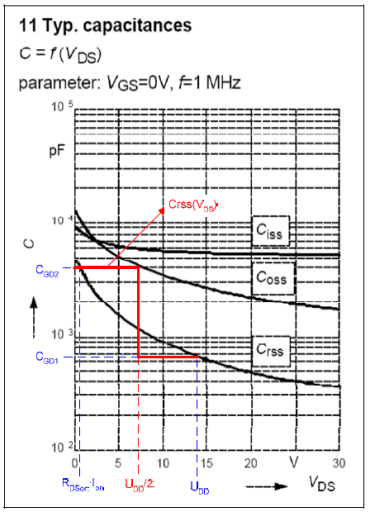

Figure 5-II Typical capacitances of a power MOSFET

The drain-source voltage during the fall time, with the two-point approximation being taken into account, is shown in the previous figure with the dotted line. Since this approximation is used only to determine the voltage fall time (as well as the rise time during switch off) and the drain-source voltage is assumed to have the linear form (solid line in in the previous figure), it becomes clear that this analysis presents the worst case for the switching losses calculation.

The gate current during tfu can be calculated as:

$$I_{Gon} = \frac{U_{Dr} - U_{(plateau)}}{R_G} \tag{135}$$

The voltage fall time can now be calculated as a median of the fall times defined through the gate current and the capacitances C_{GD1} and C_{GD2}.

$$t_{fu} = \frac{t_{fu1} + t_{fu2}}{2} \tag{136}$$

where:

$$t_{fu1} = \left(U_{DD} - R_{DS_{on}} \cdot I_{D_{on}}\right) \cdot \frac{C_{GD1}}{I_{Gon}} = \left(U_{DD} - R_{DS_{on}} \cdot I_{D_{on}}\right) \cdot R_G \cdot \frac{C_{GD1}}{U_{Dr} - U_{(plateau)}} \tag{137}$$

$$t_{fu2} = \left(U_{DD} - R_{DS_{on}} \cdot I_{D_{on}}\right) \cdot \frac{C_{GD2}}{I_{Gon}} = \left(U_{DD} - R_{DS_{on}} \cdot I_{D_{on}}\right) \cdot R_G \cdot \frac{C_{GD2}}{U_{Dr} - U_{(plateau)}} \tag{138}$$

Switch-off transient

Switch-off process corresponds to the switching-on process of the MOSFET in the reverse order. Two important differences are that no reverse recovery takes place and the gate current I_{Goff} and the voltage rise time t_{ru} can be expressed as:

$$I_{Goff} = -\frac{U_{(plateau)}}{R_G} \tag{139}$$

The voltage fall time can now be calculated as a median of the fall times defined through the gate current and the capacitances C_{GD1} and C_{GD2}.

$$t_{ru} = \frac{t_{ru1} + t_{ru2}}{2} \tag{140}$$

where:

$$t_{ru1} = \left(U_{DD} - R_{DS_{on}} \cdot I_{D_{on}}\right) \cdot \frac{C_{GD1}}{I_{Goff}} = \left(U_{DD} - R_{DS_{on}} \cdot I_{D_{on}}\right) \cdot R_G \cdot \frac{C_{GD1}}{U_{(plateau)}} \tag{141}$$

$$t_{ru2} = \left(U_{DD} - R_{DS_{on}} \cdot I_{D_{on}}\right) \cdot \frac{C_{GD2}}{I_{Goff}} = \left(U_{DD} - R_{DS_{on}} \cdot I_{D_{on}}\right) \cdot R_G \cdot \frac{C_{GD2}}{U_{(plateau)}} \tag{142}$$

Switching Energies and Losses

According to previous considerations, the worst case turn-on energy losses in power MOSFET (E_{onM}) can be calculated as the sum of the switch-on energy without taking the reverse recovery process into account (E_{onMi}) and the switch-on energy caused by the reverse-recovery of the free-wheeling diode (E_{onMrr}):

$$E_{onM} = \int_0^{t_{ri}+t_{fu}} U_{DS}(t) \cdot i_D(t)\, dt = E_{onMi} + E_{onMrr} = U_{DD} \cdot I_{D_{on}} \cdot \frac{t_{ri} + t_{fu}}{2} + Q_{rr} \cdot U_{DD} \tag{143}$$

The peak of the reverse-recovery current can be calculated as:

$$I_{Frr_{peak}} = \frac{2Q_{rr}}{t_{rr}} \tag{144}$$

Turn-on energy in the diode consists mostly of the reverse-recovery energy (E_{onD}):

$$E_{onD} = \int_0^{t_{ri}+t_{fu}} U_D(t) \cdot i_F(t)\, dt \approx E_{onDrr} = \frac{1}{4} \cdot Q_{rr} \cdot U_{Drr} \tag{145}$$

where U_{Drr} is the voltage across the diode during reverse recovery. For the worst case calculation this voltage can be approximated with a supply voltage ($U_{Drr} = U_{DD}$).

The switch-off energy losses in the MOSFET can now be calculated in a similar manner. The switch-off losses in the diode are normally neglected. Therefore:

$$E_{offM} = \int_0^{t_{ru}+t_{fi}} U_{DS}(t) \cdot i_D(t)\, dt = U_{DD} \cdot I_{D_{off}} \cdot \frac{t_{ru}+t_{fi}}{2} \tag{146}$$

The switch-off losses in the MOSFET and the diode are the product of switching energy and the switching frequency f_s:

$$P_{swM} = \left(E_{onM} + E_{offM}\right) \cdot f_s \tag{147}$$

$$P_{swD} = \left(E_{onD} + E_{offD}\right) \cdot f_s \approx E_{onD} \cdot f_s \tag{148}$$

5.3. Diode Losses

Diode forward characteristics, forward current I_F and voltage V_F can be modeled by a straight line defined by a threshold voltage V_T and a dynamic resistance R_D.

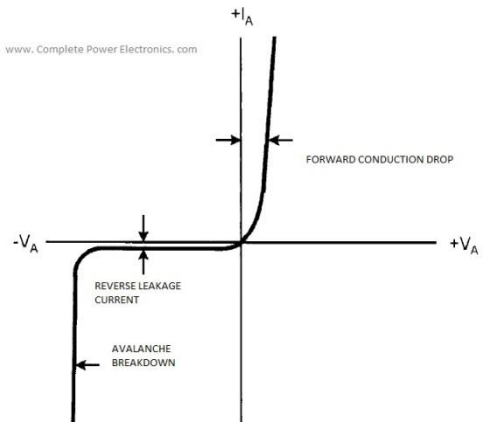

Figure 5-III Typical diode characteristic

Thus we can write:

$$V_F(t) = V_T + R_D \cdot I_F(t) \tag{149}$$

The losses can then be expressed as:

$$P_{cond} = \frac{1}{T} \cdot \int_0^T V_F(t) \cdot I_F(t)\, dt =>$$

$$P_{cond} = \frac{1}{T} \cdot \int_0^T \left(V_T + R_D \cdot I_F(t)\right) \cdot I_F(t)\, dt =>$$

$$P_{cond} = \frac{1}{T} \cdot \int_0^T \left(V_T \cdot I_F(t) + R_D \cdot I_F^2(t)\right) dt =>$$

$$P_{cond} = \frac{1}{T} \cdot \left(\int_0^T V_T \cdot I_F(t)\, dt + \int_0^T R_D \cdot I_F^2(t)\, dt \right) =>$$

$$P_{cond} = V_T \cdot \frac{1}{T} \int_0^T I_F(t)\, dt + R_D \cdot \frac{1}{T} \int_0^T I_F^2(t)\, dt =>$$

$$P_{cond} = V_T \cdot I_{F(av)} + R_D \cdot I_{F(rms)}^2 \tag{150}$$

Where $I_{F(av)}$ is the forward average current and $I_{F(rms)}$ is the forward root mean square current flowing through the diode.

5.4. Losses though the common mode chokes

Common-mode chokes, where two coils are wound on a single core, are useful for prevention of electromagnetic interference (EMI) and radio frequency interference (RFI) from power supply lines and for prevention of malfunctioning of electronic equipment. They pass differential currents (equal but opposite), while blocking common-mode currents. [22]

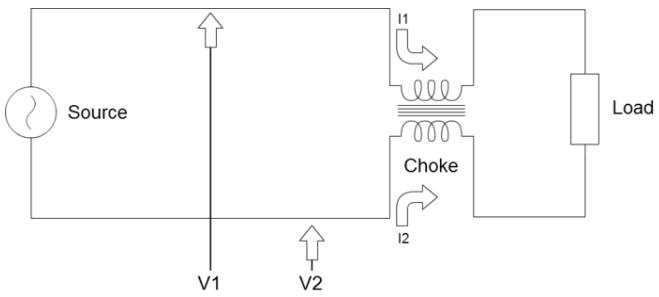

Figure 5-IV Common-mode chokes

Magnetic fields produced by differential-mode currents in the windings tend to cancel each other out; thus the choke presents little inductance or impedance to

differential-mode currents. This also means the core will not saturate even for large differential-mode currents, and the maximum current rating is instead determined by the heating effect of the winding resistance. Common-mode currents, however, see a high impedance due to the combined inductance of the windings.

The losses in each of the common mode chokes are:

$$P_{choke} = I_{in(rms)}^2 \cdot R_{choke} \tag{151}$$

5.5. Losses across the resonant capacitors

An ideal capacitor only stores and releases electrical energy, without dissipating any. In reality, all capacitors have imperfections within the capacitor's material that create resistance. This is specified as the equivalent series resistance or ESR of a component. This adds a real component to the impedance. [23]

$$Z_c = \frac{1}{j\omega C} + R_{ESR} \tag{152}$$

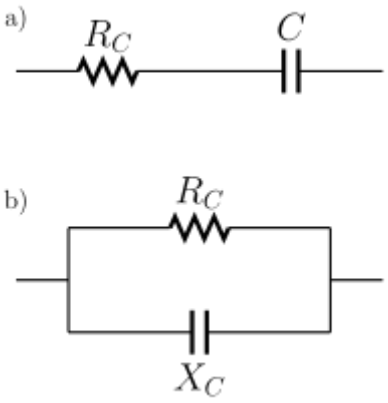

Figure 5-V Equivalent ESR of a capacitor

As frequency approaches infinity, the capacitive impedance (or reactance) approaches zero and the ESR becomes significant. As the reactance becomes negligible, power dissipation approaches:

$$P_{C\,rms} = \frac{V_{rms}^2}{R_{ESR}} \tag{153}$$

5.6. Losses in the IPT Transformer

The losses in the Inductive Power Transfer Transformer consist of two main parts; the losses due to the resistance of the windings of the primary and the secondary and the core losses of the ferrite plates that are used for the coupling of the primary and the secondary.

Losses in the ferrite material

The ferrite material has a characteristic of core losses related to the magnetic flux density. If we simulate the coil configuration with Maxwell in order to determine the flux density and then integrate in the volume of the ferrite body with the losses kW/m^3, as they are given in the ferrite material datasheet, we can estimate the core losses of the ferrite plates.

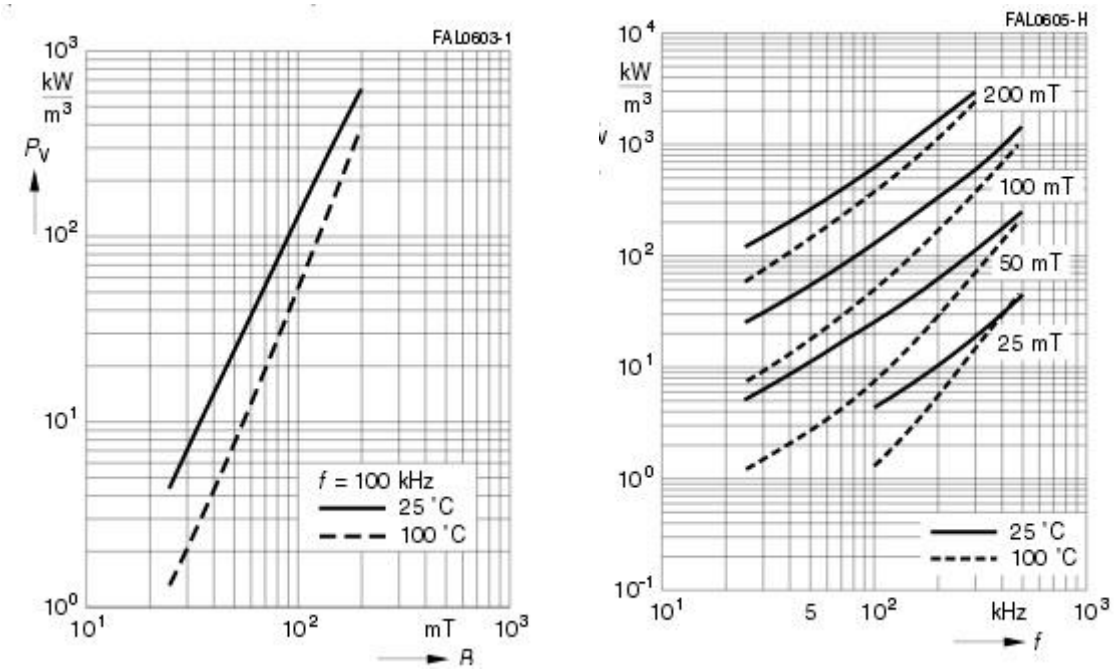

Figure 5-VI Core losses, as given in ferrite material datasheet

The flux density distribution can be simulated with the Maxwell software. An example of a simulation is depicted below:

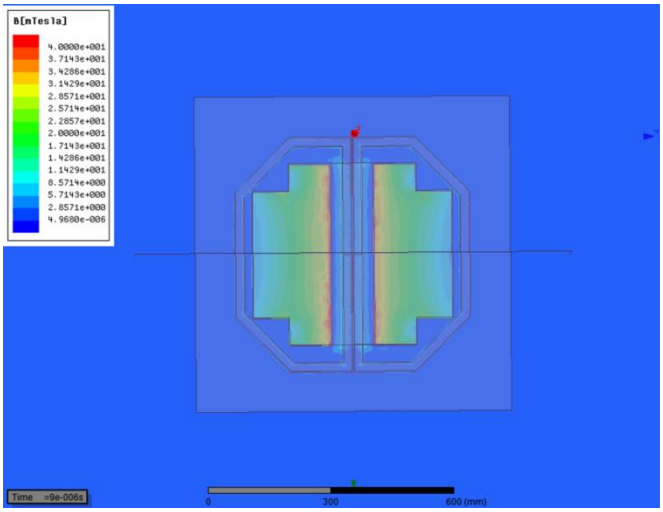

Figure 5-VII Example of flux density simulation using Maxwell

After simulating the flux density distribution in space with Maxwell we can estimate the losses by integrating. For the double-D configuration the ferrite losses dependence to the current flowing through a double D coil is presented below:

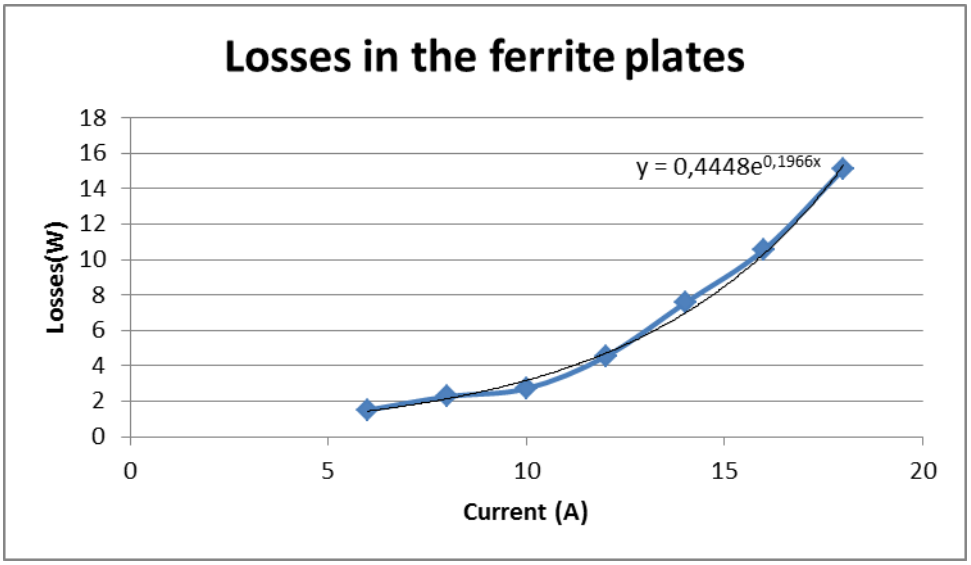

Figure 5-VIII Losses in the ferrite plates in double-D configuration

Skin effect

It is known that a time-invariant current in a homogeneous cylindrical conductor is distributed uniformly over the conductor cross section. In the case of a non-cylindrical conductor, the time invariant current in it is not uniformly distributed, but it exists in the entire conductor. It I known, that a time-variant current has the tendency to concentrate near the surfaces of the conductors. If the frequency is very

high, the current is restricted to a very thin layer near the conductor surfaces, practically on the surfaces themselves. This entire phenomenon of non-uniform distribution of time varying currents in conductors is known as the skin effect.

The cause of skin effect is electromagnetic induction. A time varying magnetic field is accompanied by a time varying induced electric field, which in turn induces secondary time varying currents and a secondary magnetic field. From Lentz's law, it is known that the induced currents produce the magnetic flux, which is opposite to the external flux, which is the flux that produced the induced currents, so that the total flux is reduced. The induced currents are larger with larger conductivity and the flux reduction is more pronounced with larger permeability. Consequently, both the total time varying magnetic field and induced currents inside conductors are reduced when compared with the case of DC.

The skin effect is of considerable practical importance. It is met in all conductors, but the tendency of current and magnetic flux to be restricted to a thin layer on the conductor surface is much more pronounced for ferromagnetic conductors that for non-ferromagnetic conductors of the same conductivity.

Proximity effect

The term proximity effect refers to the influence of alternating current in one conductor on the current distribution in another, nearby conductor.

If we consider a coaxial cable of finite length and assume that an alternating current flows only in the inner conductor and that the outer conductor is not connected to anything. If the outer conductor is much thicker that the skin depth, there is practically no magnetic field inside the outer conductor. By application of Ampere's law to a coaxial circular contour contained in that conductor, it follows that the induced current on the inside surface of the outer conductor is exactly equal and opposite to the current in the inner conductor. This is an example of the proximity effect.

The current from the inner surface of the outer conductor must close into itself over the outside surface of the outer conductor, so that on that surface the same current exists as in the inner conductor. If now, we have normal cable current in the outer conductor, it is the same, but opposite to the current on the conductor outer surface, so the two cancel out. The result is a current over the inner conductor and a current over the inside surface of the outer conductor. This is a combination of skin effect and proximity effect. This encountered effect is combined, but is usually called proximity effect. The analysis of the proximity effect is rather complicated.

Transformer winding AC losses

Transformer winding AC losses due to skin effect and proximity effect are limited, as the appropriate Litz wire was used.

The losses of the transformer windings are given by:

$$P_L = R_{@\,freq} \cdot I_L^2 \tag{154}$$

6. Results and Conclusions

6.1. Description of the tests

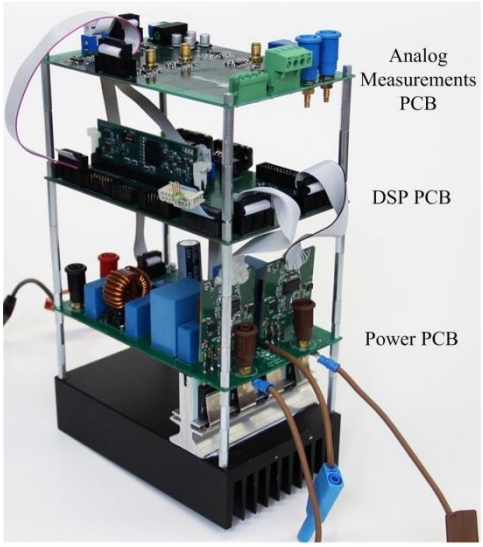

Figure 6-I Full Bridge converter protorype

In this chapter, some practical results and measurements are going to be presented. A complete IPT system was built in the lab, using the double-D topology for the primary and the secondary coils.

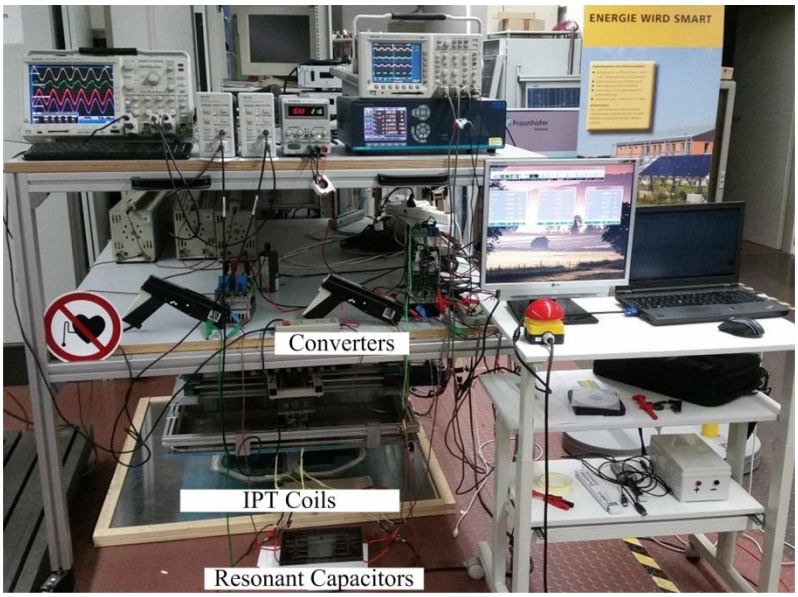

Figure 6-II Test Setup

The tests took place for different distances and displacements of the secondary with respect to the primary. Both full bridge and half bridge configurations were tested, in order to examine and compare their behavior. The X and Y axis of the displacements are depicted below. The Z axis represents the distance between the primary and the secondary.

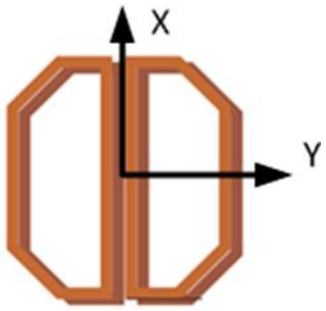

Figure 6-III X and Y axis of displacement

The cases examined are:

- 15cm distance, no misalignment, full bridge configuration
- 15cm distance, no misalignment, half bridge configuration
- 20cm distance, no misalignment, full bridge configuration
- 20cm distance, no misalignment, half bridge configuration
- 20 cm distance, X=15cm,Y=0, full bridge configuration
- 20 cm distance, X=15cm,Y=5cm, full bridge configuration
- 20 cm distance, X=15cm,Y=5cm, half bridge configuration

6.2. Test procedure

The first step for each test was to measure the parameters of the IPT transformer. The three test approach described in chapter 3.6 was used to determine the mutual and the leakage inductances of the IPT transformer for each test.

The parameters calculated from this test were used in the formulas presented in chapter 4, to theoretically estimate the rms values of the currents that flow through the circuit during operation and the expected efficiency. The parameters calculated, were also used for simulation of the system operation using Matlab/PLECS software.

During the operation of the system, the switching frequency was equal to the primary resonant frequency of each test setup, which means a gain of 1 for the output with respect to the input, as described in chapter 4. The system is designed so that this frequency is near 140kHz, which is the suggestion introduced so far by the industry.

Efficiency measurements were taken in the lab for a wide range of output power load in each case.

Some important facts about the measurements have to be mentioned. The most important of all is that manual feedforward control was used in order to track the resonant frequency and determine the switching frequency (by comparing input and output, always in relation to the transfer characteristic). This could not always be quite precise and it could possibly lead to deviations between the calculations of the circuit quantities and reality. Another point is that, during the tests, for the secondary bridge rectifiers no recovery diodes were used, so the reverse recovery effects were eliminated.

6.3. Losses

The losses taken into account for the analysis are presented in the following table. The losses through the input common mode chokes were taken into account in the calculation of the overall efficiency, but they present no interest for the further analysis of the system losses.

Resonant capacitor losses	Pcap
Secondary rectifier losses	P_D
Primary bridge conduction losses	P_mos_con
Losses in the IPT transformer windings	P_L
Primary bridge switching losses	P_sw
Losses in the ferrite plates	P_core
Total loss(from bridge input to output)	P_loss

Table 6-1 Table of system losses

The current flowing through the primary resonant capacitor is $i_p(t)$ for both full and half bridge configurations. The current flowing through the primary resonant capacitor is $i_s(t)$ for both full and half bridge configurations. By knowing the ESR of the capacitors we can calculate their losses, as shown in chapter 5.

For the secondary rectifier in the full bridge configuration the losses of the 4 diodes are given by:

$$P\_D = 4\left(V_T \cdot \overline{I_D} + R_D \cdot I_D^2\right) \tag{155}$$

For the secondary rectifier in the half bridge configuration the losses of the diode are given by:

$$P\_D = V_T \cdot \overline{I_D} + R_D \cdot I_D^2 \tag{156}$$

For the primary full bridge, the conduction losses of the 4 MOSFETs are given by:

$$P\_mos\_con = 4 \cdot R_{DS_{on}} \cdot I_{sw}^2 \tag{157}$$

For the primary half bridge, the conduction losses of the 2 MOSFETs are given by:

$$P\_mos\_con = 2 \cdot R_{DS_{on}} \cdot I_{sw}^2 \tag{158}$$

The current flowing through the primary winding of the IPT transformer is $i_p(t)$ for both full and half bridge configurations. The current flowing through the secondary winding of the IPT transformer is $i_s(t)$ for both full and half bridge configurations. By knowing the resistance of the windings we can calculate their losses, as shown:

$$P\_L = R_{prim.winding} \cdot I_p^2 + R_{sec.winding} \cdot I_s^2 \tag{159}$$

The switch-off energy losses of the MOSFET are practically the area of the triangle that is formed from the product of the MOSFET turn off current and the MOSFET voltage. For hard switching this is given by:

$$E_{offM} = U_{DD} \cdot I_{D_{off}} \cdot \frac{t_{ru} + t_{fi}}{2} \tag{160}$$

,where $I_{D_{off}}$ is the current through the MOSFET at the moment of turn-off. This energy multiplied by the frequency gives us the switching power losses of a single MOSFET. In our case, due to the capacitance that was added in parallel between the drain and the source of the MOSFETs, according to section 4.5, the rise of the voltage is delayed and the current goes to zero before the voltage rises significantly. This reduces the overall area of the triangle mentioned above. As a result, the switching losses are limited. For the full bridge configuration the power loss is:

$$P\_sw = 4 \cdot E_{offM} \cdot f_{sw} \tag{161}$$

For the half bridge configuration the power loss is:

$$P\_sw = 2 \cdot E_{offM} \cdot f_{sw} \tag{162}$$

The reverse recovery energy of the diodes was also taken into account in the calculations, although it is quite small.

The losses in the ferrite plates P_core are given by the Maxwell simulations for both cases, taking into account the datasheet of the ferrites.

6.4. 15cm distance, no misalignment, full bridge configuration

The efficiency measurements carried out in the lab are summarized in the graph:

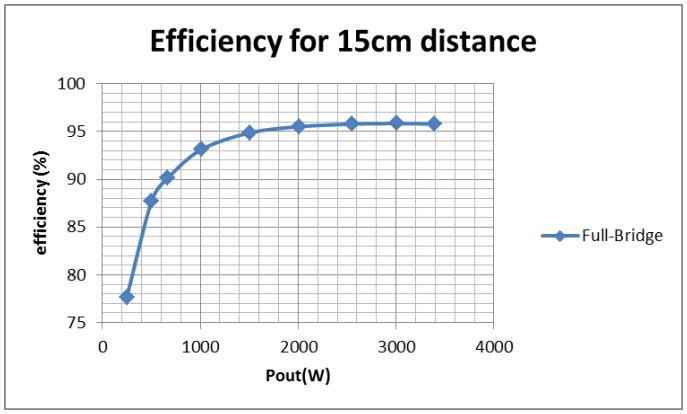

Figure 6-IV Measured Efficiency

The currents in the oscilloscope are shown below:

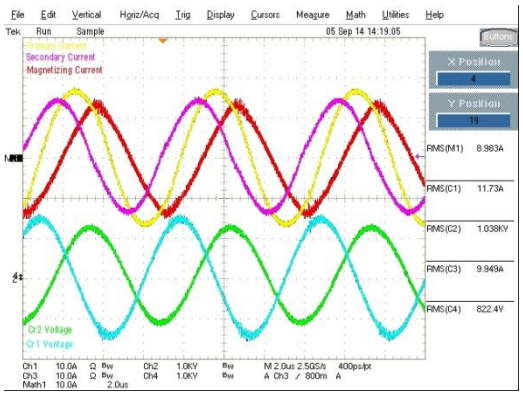

Figure 6-V Currents and resonant capacitor voltages in the oscilloscope

The results from the PLECS simulation for nominal operation are depicted below:

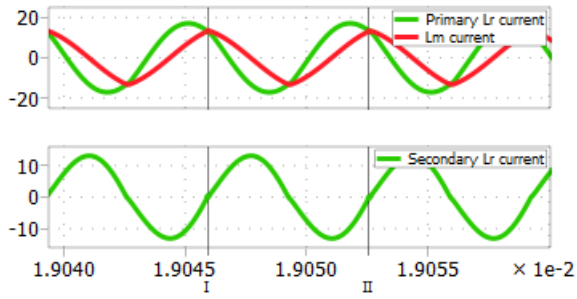

Figure 6-VI Simulation of the currents for nominal operation

The rms values of the currents for the whole power range are presented below:

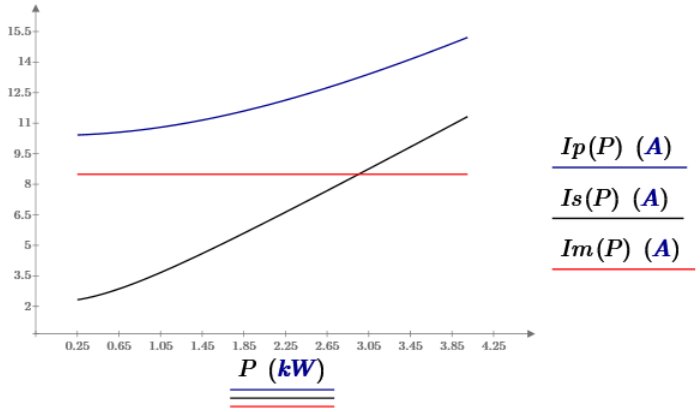

Figure 6-VII Calculated rms values of the currents for the whole power range

The estimated efficiency curve for the whole output power range is depicted below:

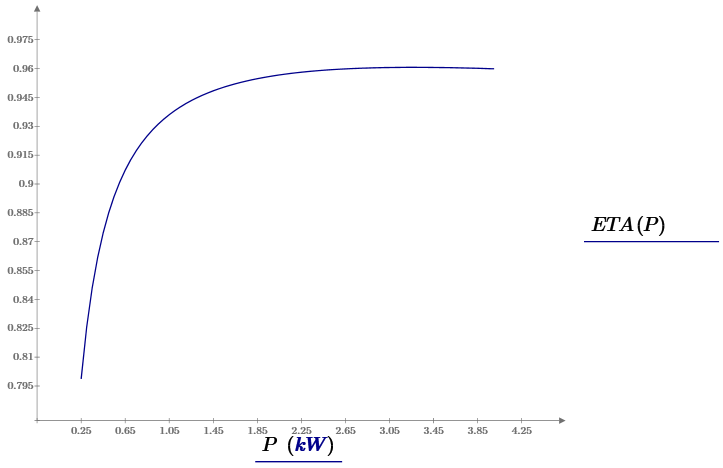

Figure 6-VIII Theoretically estimated efficiency curve

The power losses for the whole output power range are summarized:

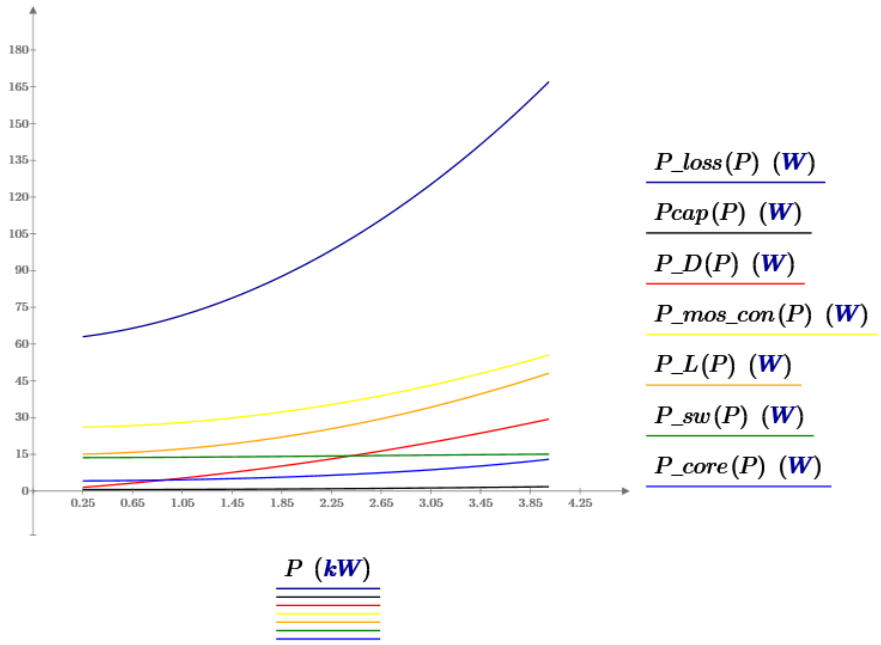

Figure 6-IX Theoretically calculated power losses for the whole output power range

The losses under nominal load conditions of operation (3,3kW) are presented here:

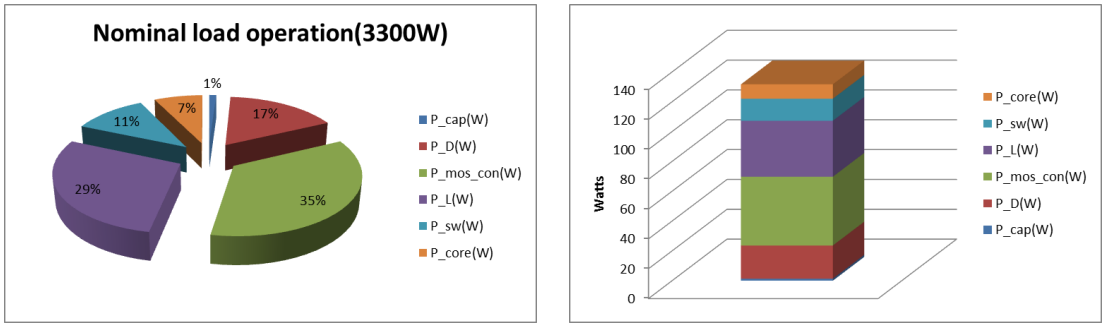

Figure 6-X Losses analysis for nominal load conditions of operation

6.5. 15cm distance, no misalignment, half bridge configuration

The efficiency measurements carried out in the lab are summarized in the graph:

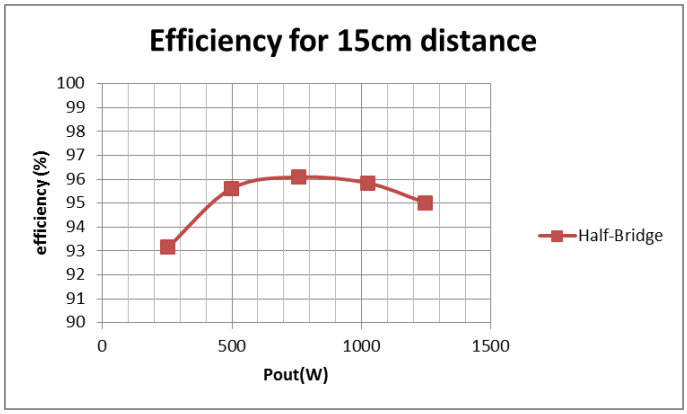

Figure 6-XI Measured Efficiency

The currents in the oscilloscope are shown below:

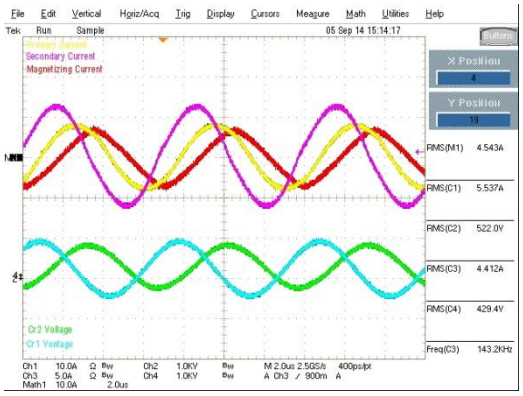

Figure 6-XII Currents and resonant capacitor voltages in the oscilloscope

The results from the PLECS simulation for nominal operation are depicted below:

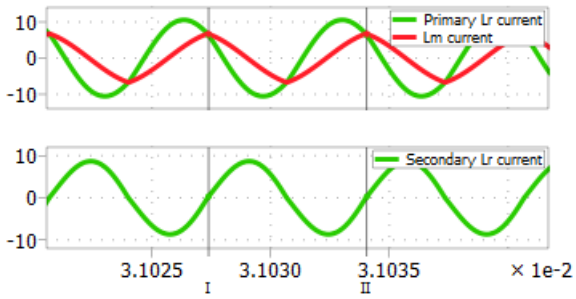

Figure 6-XIII Simulation of the currents for nominal operation

The rms values of the currents for the whole power range are presented below:

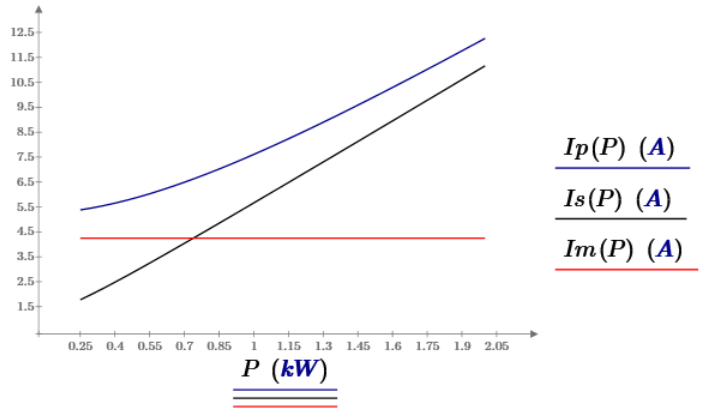

Figure 6-XIV Calculated rms values of the currents for the whole power range

The estimated efficiency curve for the whole output power range is depicted below:

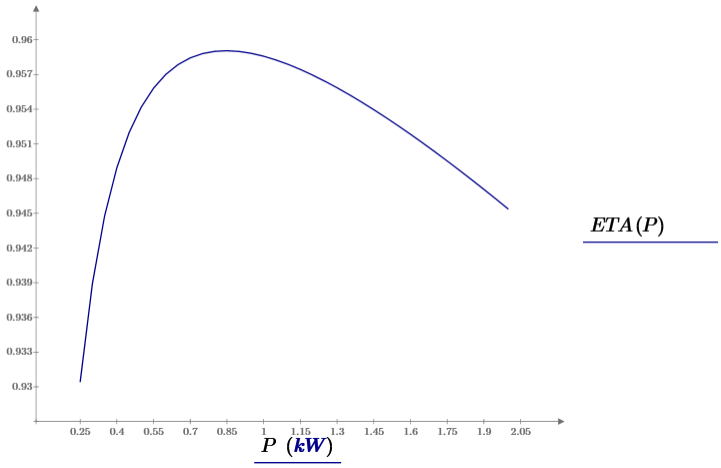

Figure 6-XV Theoretically estimated efficiency curve

The power losses for the whole output power range are summarized:

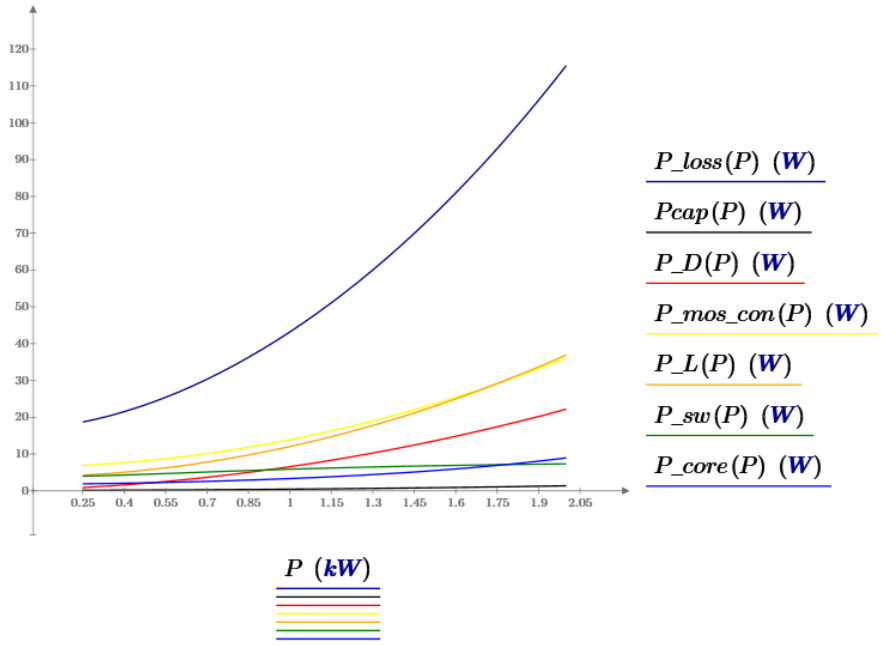

Figure 6-XVI Theoretically calculated power losses for the whole output power range

The losses under nominal load conditions of operation (1,1kW) are presented here:

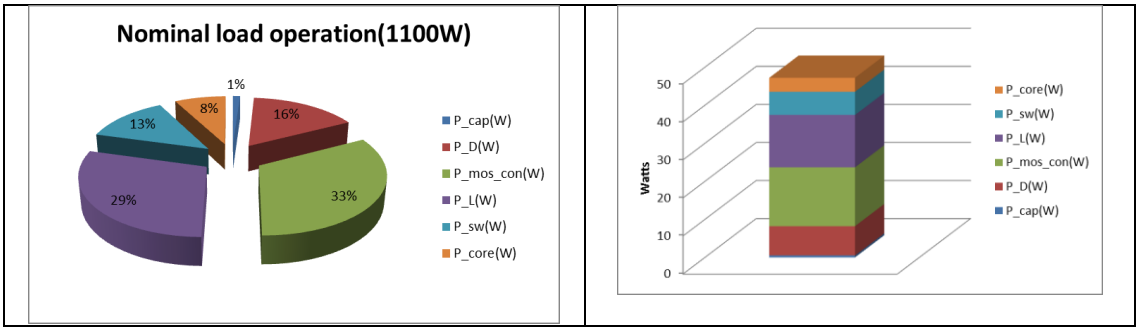

Figure 6-XVII Losses analysis for nominal load conditions of operation

6.6. 20cm distance, no misalignment, full bridge configuration

The efficiency measurements carried out in the lab are summarized in the graph:

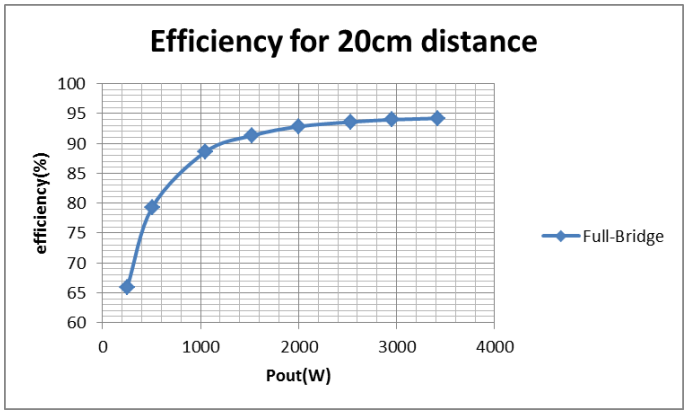

Figure 6-XVIII Measured Efficiency

The currents in the oscilloscope are shown below:

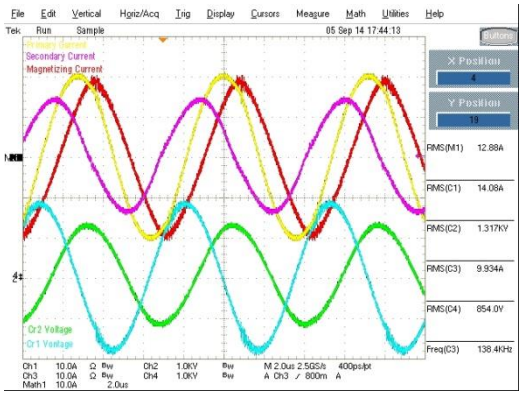

Figure 6-XIX Currents and resonant capacitor voltages in the oscilloscope

The results from the PLECS simulation for nominal operation are depicted below:

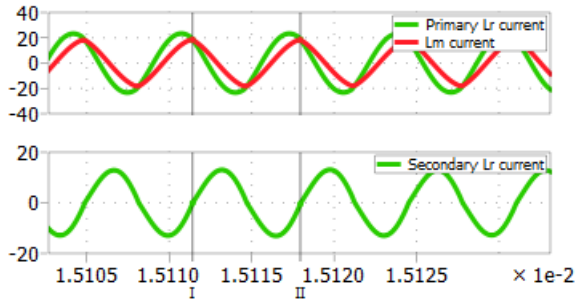

Figure 6-XX Simulation of the currents for nominal operation

The rms values of the currents for the whole power range are presented below:

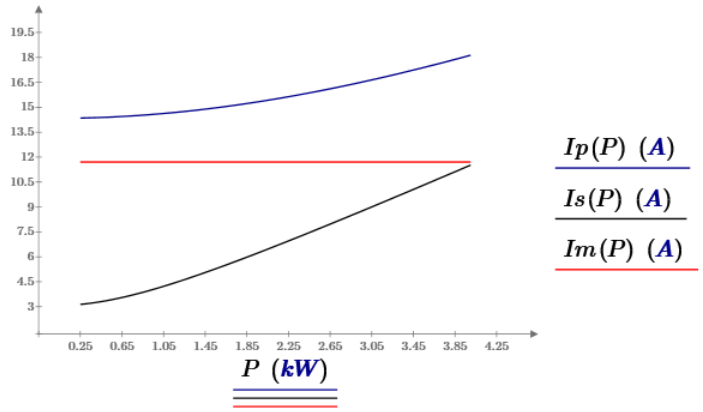

Figure 6-XXI Calculated rms values of the currents for the whole power range

The estimated efficiency curve for the whole output power range is depicted below:

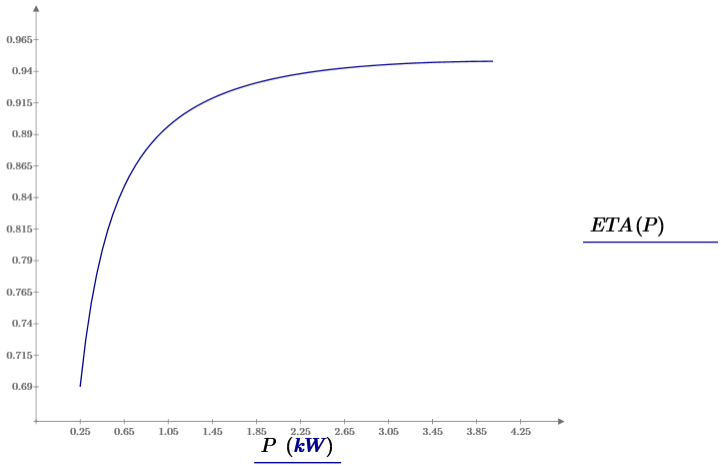

Figure 6-XXII Theoretically estimated efficiency curve

The power losses for the whole output power range are summarized:

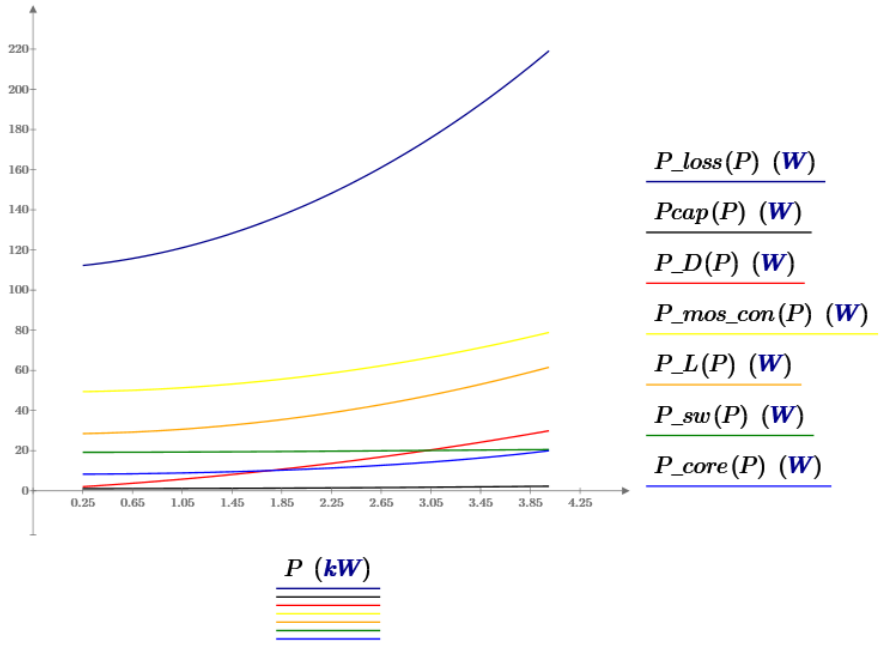

Figure 6-XXIII Theoretically calculated power losses for the whole output power range

The losses under nominal load conditions of operation (3,3kW) are presented here:

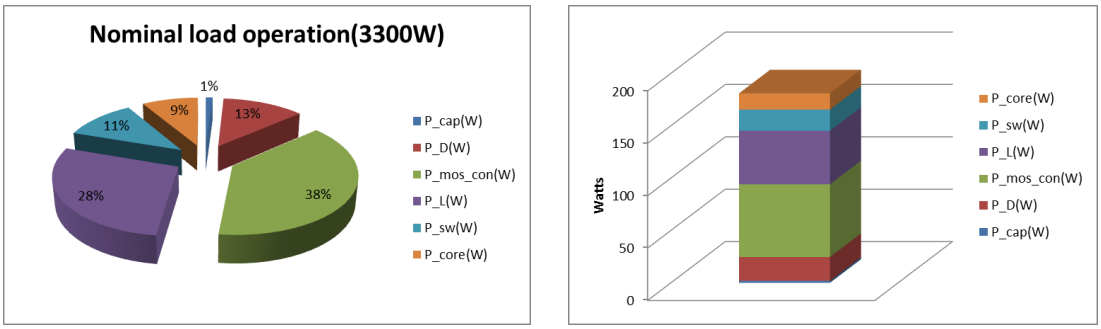

Figure 6-XXIV Losses analysis for nominal load conditions of operation

6.7. 20cm distance, no misalignment, half bridge configuration

The efficiency measurements carried out in the lab are summarized in the graph:

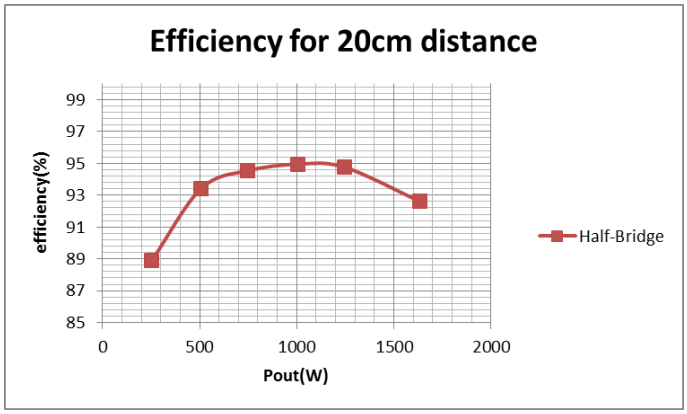

Figure 6-XXV Measured Efficiency

The currents in the oscilloscope are shown below:

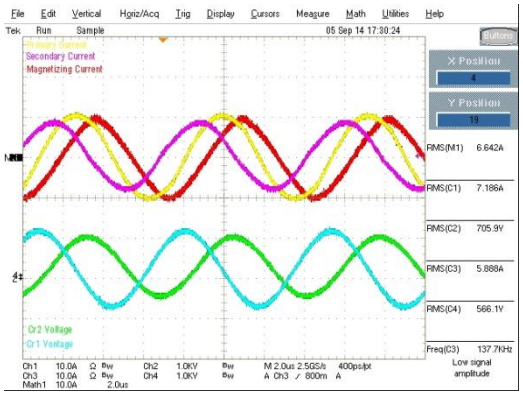

Figure 6-XXVI Currents and resonant capacitor voltages in the oscilloscope

The results from the PLECS simulation for nominal operation are depicted below:

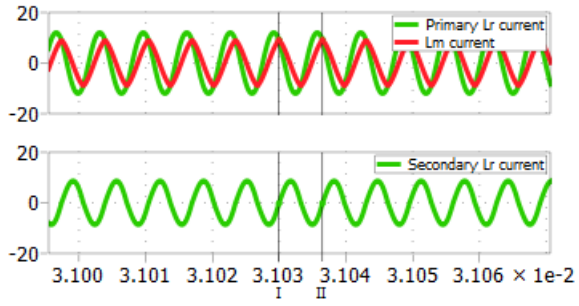

Figure 6-XXVII Simulation of the currents for nominal operation

The rms values of the currents for the whole power range are presented below:

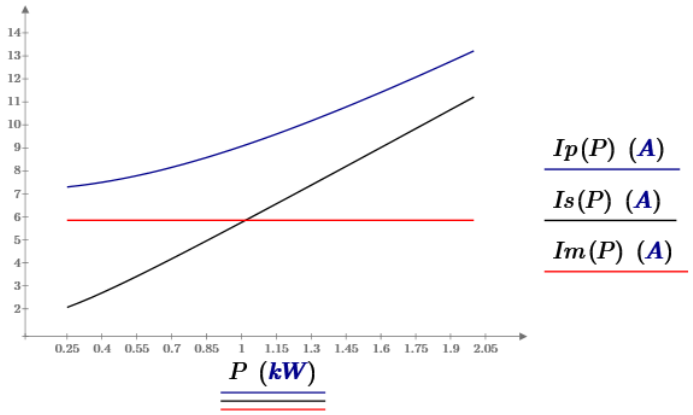

Figure 6-XXVIII Calculated rms values of the currents for the whole power range

The estimated efficiency curve for the whole output power range is depicted below:

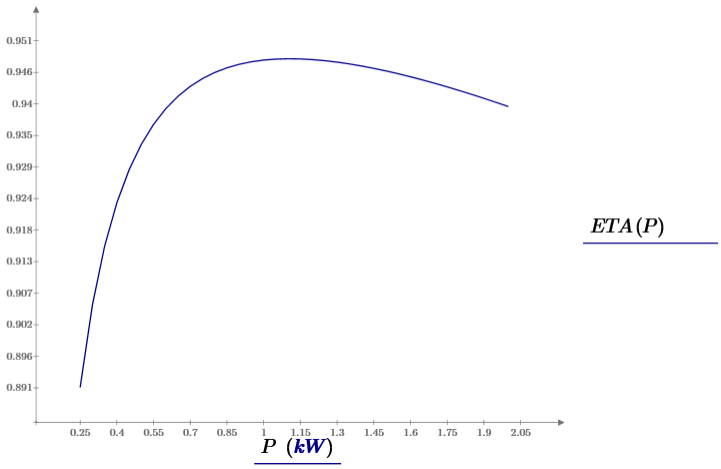

Figure 6-XXIX Theoretically estimated efficiency curve

The power losses for the whole output power range are summarized:

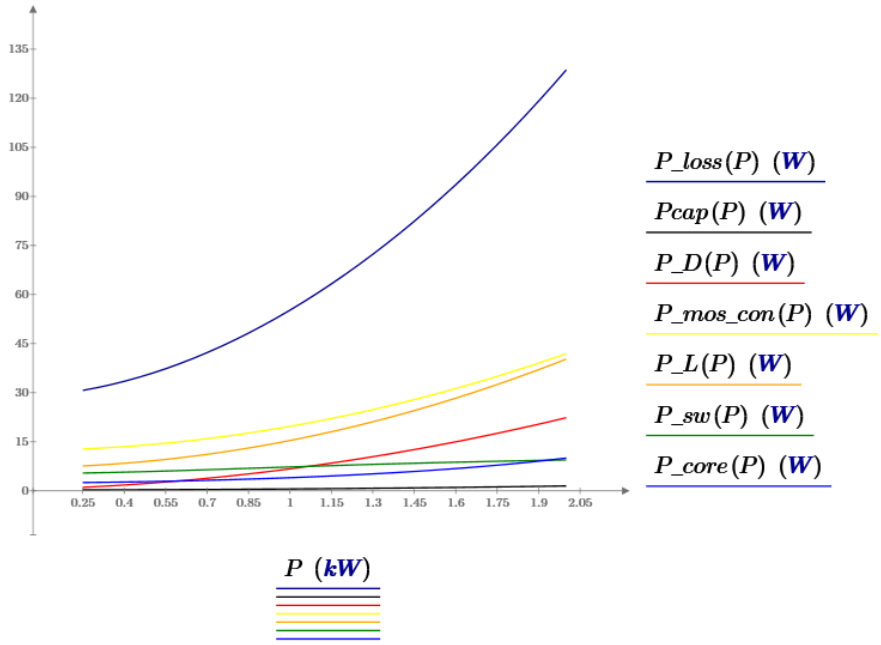

Figure 6-XXX Theoretically calculated power losses for the whole output power range

The losses under nominal load conditions of operation (1,1kW) are presented here:

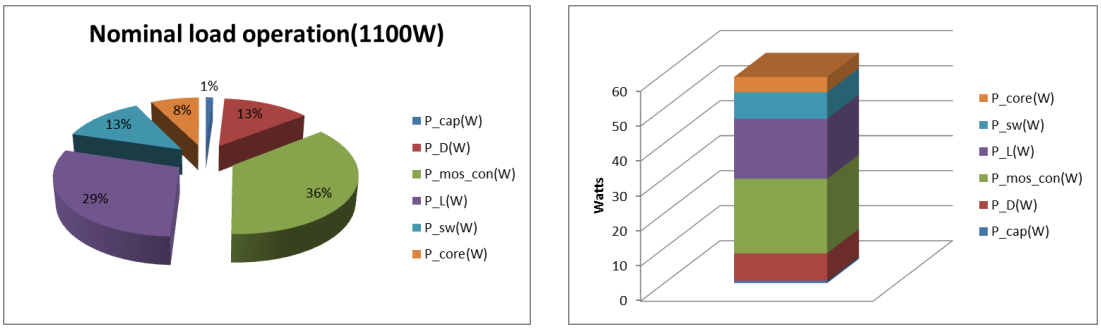

Figure 6-XXXI Losses analysis for nominal load conditions of operation

7. Conclusions and Recommendations

7.1. Conclusions

Commercially available electric vehicles use cables to connect the vehicle to the grid, although this involves certain disadvantages such as risk of vandalism, additional effort for the user and present safety issues such as electrical hazard due to the open contacts and hanging charging cables in public areas. Another drawback is that the car could be left unplugged so the battery will stay uncharged, which causes a minimization of the available driving range. An alternative is contactless charging based on Inductive Power Transfer (IPT). This technology provides galvanic isolation, has no open contacts and no hanging charging cables allowing an automatic, reliable and safe charging process. Therefore, it is expected to improve the user acceptance of electric vehicles and contribute to the integration of electric vehicles into the market. Thus it will support the full exploitation of the benefits of electro-mobility.

Wireless transmission of energy using induction is based on the electromagnetic theory. A current through a conductor produces a magnetic field. Variations in the magnetic field create an electric field. The electric field causes the electrical charges to move, producing a current. The couplers of IPT systems are loosely coupled transformers in which there is no core that links the primary and secondary coils. Therefore the coupler has to transfer the power across the air-gap.

Depending on the distance between the coils, only a fraction of the magnetic flux generated by the primary coil penetrates the secondary coil and contributes to the power transmission. The more flux reaches the secondary, the better the coils are coupled. The grade of coupling is expressed by the coupling factor k. The coupling factor k can be calculated from equation and is decreased with increase of the distance between the coils and increased with the increase of the diameter of the coils. In case of an EV the distance between the primary and secondary coil of the IPT system is relatively high: up to 25cm. In addition there are size and weight limitations, especially for the coil that is placed in the EV. As a consequence, the coupling factor is affected to a point where it becomes weak or very small.

In order to be able to transfer energy efficiently with relatively low coupling factor the reactive power of the leakage inductances needs to be compensated by capacitors. The optimal way to do that is the use of a resonant converter. This fact in combination with the need for bidirectional power flow lead to the choice of a Bidirectional CLLC Series Resonant Converter (CLLC-SRC), which utilizes the leakage inductance as part of a resonant tank.

The IPT system that was introduced reaches high efficiency rates, mainly because the resonant converter operates under Zero Voltage Transmission during turn on.

However, as seen in chapter 6, the efficiency is reduced with the reduction of the coupling factor.

As it can be seen from the experimental results, the most important factor for the efficiency of the IPT system is the magnetizing current. It adds up to the primary current and therefore plays a major role in almost all the losses of the primary side, especially the conduction losses and the losses in the primary of the IPT transformer. The magnetizing current is the current that is required to establish the magnetic field and the flux that links both sides of the loosely coupled transformer. It can easily be observed that it hardly changes for different power loads. This leads to low efficiency rates for low power loads, as it is comparable with the primary current at this low level of loads.

This is exactly the reason why for low load the half bridge configuration proves to perform better at low loads. For this configuration the rms value of the magnetizing current halves in comparison with the respective case of the full bridge configuration. At low loads, the secondary current that feeds the load is not very high. The combination of these two factors leads to a lower primary current, that causes less losses in the IPT transformer and has to flow from only 2 semiconductor devices, as a half bridge utilizes only one leg of a full bridge. In this way the conduction losses are significantly reduced and we are led to high efficiencies for low loads.

Consequently, the conclusion that can be excluded is that, in order to build an efficient wireless power transfer system, the most important factor that needs to be taken into account is the design of the coils that form the IPT transformer. A good design that improves the magnetic coupling leads to low magnetization currents, a fact which in turn reduces the overall current flowing through the primary circuit, reducing the conduction losses. With ZVT ensured and the switching losses limited, a reduction of the conduction losses can result in very high efficiency performances.

7.2. Recommendations

Inductive power transfer offers a feasible solution for the acceptance of EV and its adoption from the automotive industry is a matter of time. The two main problems that need to be overcome are the improvement of the poor coupling of the IPT transformer, which is loosely coupled and the introduction of control techniques that will give the ability to track the primary resonant frequency of the resonant tank, while remaining within the limits that the safety standards of the industry set. The improvement of coil designs is a sector of research than can really go into depth. Concerning the control of an IPT system for commercial use, it can be very challenging and difficult, because the standards are quite strict. For instance, the trend about control, is to avoid any communication between the primary and the secondary

or introduce a communication that is really slow (such as WiFi) in comparison with the traditional control systems.

8. References

[1] Chawla Tosunoglu, “State of the Art in Inductive Charging for Electronic Appliances and its Future in Transportation,” http://www.eng.fiu.edu/mme/robotics/elib/FCRAR2012-InductiveCharging.pdf.

[2] ZHEN NING LOW, “HIGH EFFICIENCY LOOSELY COUPLED WIRELESS POWER TRANSFER SYSTEM VIA MAGNETIC INDUCTION,” Dissertation, UNIVERSITY OF FLORIDA, 2009.

[3] H. H. Wu, A. Gilchrist, K. Sealy, P. Israelsen, and J. Muhs, “A review on inductive charging for electric vehicles,” in *Electric Machines Drives Conference (IEMDC), 2011 IEEE International*, 2011, pp. 143–147.

[4] A. Neves, D. M. Sousa, A. Roque, and J. M. Terras, “Analysis of an inductive charging system for a commercial electric vehicle,” in *Power Electronics and Applications (EPE 2011), Proceedings of the 2011-14th European Conference on*, 2011, pp. 1–10.

[5] Shuo Wang and D. Dorrell, “Review of wireless charging coupler for electric vehicles,” in *Industrial Electronics Society, IECON 2013 - 39th Annual Conference of the IEEE*, 2013, pp. 7274–7279.

[6] B. Peschiera and S. S. Williamson, “Review and comparison of inductive charging power electronic converter topologies for electric and plug-in hybrid electric vehicles,” in *Transportation Electrification Conference and Expo (ITEC), 2013 IEEE*, 2013, pp. 1–6.

[7] M. Cederlöf, “Inductive Charging of Electrical Vehicles: System Study,” Master Thesis, KTH, Stockholm Sweden, 2012.

[8] Chwei-Sen Wang, G. A. Covic, and O. H. Stielau, “Power transfer capability and bifurcation phenomena of loosely coupled inductive power transfer systems,” *Industrial Electronics, IEEE Transactions on*, vol. 51, no. 1, pp. 148–157, 2004.

[9] Chwei-Sen Wang, O. H. Stielau, and G. A. Covic, “Design considerations for a contactless electric vehicle battery charger,” *Industrial Electronics, IEEE Transactions on*, vol. 52, no. 5, pp. 1308–1314, 2005.

[10] G. Lempidis, Y. Zhang, M. Jung, R. Marklein, S. Sotiriou, and Y. Ma, Eds, Wired and wireless charging of electric vehicles: A system approach, 2014

[11] Rathge, “Systematically Design and Optimisation of Inductive Power Transmission Systems,”

[12] J. G. Hayes, N. O’Donovan, M. G. Egan, and T. O’Donnell, “Inductance characterization of high-leakage transformers,” in *Applied Power Electronics Conference and Exposition, 2003. APEC ’03. Eighteenth Annual IEEE*, 2003, pp. 1150-1156 vol.2.

[13] A. Hillers, D. Christen, and J. Biela, “Design of a Highly efficient bidirectional isolated LLC resonant converter,” in *Power Electronics and Motion Control Conference (EPE/PEMC), 2012 15th International*, 2012, pp. DS2b.13-1-DS2b.13-8.

[14] G. Pledl, M. Tauer, and D. Buecherl, “Theory of operation, design procedure and simulation of a bidirectional LLC resonant converter for vehicular applications,” in *Vehicle Power and Propulsion Conference (VPPC), 2010 IEEE*, 2010, pp. 1–5.

[15] Wei Chen, Ping Rong, and Zhengyu Lu, “Snubberless Bidirectional DC #x2013;DC Converter With New CLLC Resonant Tank Featuring Minimized Switching Loss,” *Industrial Electronics, IEEE Transactions on*, vol. 57, no. 9, pp. 3075–3086, 2010.

[16] Jee-Hoon Jung, Ho-Sung Kim, Jong-Hyun Kim, Myoung-Hyo Ryu, and Ju-Won Baek, “High efficiency bidirectional LLC resonant converter for 380V DC power distribution system using digital control scheme,” in *Applied Power Electronics Conference and Exposition (APEC), 2012 Twenty-Seventh Annual IEEE*, 2012, pp. 532–538.

[17] J.-. Jung, H.-. Kim, M.-. Ryu, and J.-. Baek, “Design Methodology of Bidirectional CLLC Resonant Converter for High-Frequency Isolation of DC Distribution Systems,” *Power Electronics, IEEE Transactions on*, vol. 28, no. 4, pp. 1741–1755, 2013.

[18] U. K. Madawala and D. J. Thrimawithana, “A Bidirectional Inductive Power Interface for Electric Vehicles in V2G Systems,” *Industrial Electronics, IEEE Transactions on*, vol. 58, no. 10, pp. 4789–4796, http://ieeexplore.ieee.org/stamp/stamp.jsp?arnumber=5711663, 2011.

[19] D. Seltzer, L. Corradini, D. Bloomquist, R. Zane, and D. Maksimovic, “Small signal phasor modeling of dual active bridge series resonant DC/DC converters with multi-angle phase shift modulation,” in *Energy Conversion Congress and Exposition (ECCE), 2011 IEEE*, 2011, pp. 2757–2764.

[20] Tianyang Jiang, Xiliang Chen, Junming Zhang, and Yousheng Wang, “Bidirectional LLC resonant converter for energy storage applications,” in *Applied Power Electronics Conference and Exposition (APEC), 2013 Twenty-Eighth Annual IEEE*, 2013, pp. 1145–1151.

[21] Dr . Dušan Graovac, Marco Pürschel, Andreas Kiep, “MOSFET Power Losses Calculation Using the Data- Sheet Parameters,” Application Note, V 1. 1 Jul. 2006.

[22] Wikipedia, *Choke (electronics) - Wikipedia, the free encyclopedia.* Available: http://en.wikipedia.org/w/index.php?oldid=618446528 (2014, Oct. 01).

[23] ____, *Capacitor - Wikipedia, the free encyclopedia.* Available: http://en.wikipedia.org/w/index.php?oldid=627527840 (2014, Oct. 01).

9. APPENDIX

9.1. Calculations

- **First Harmonic Approximation Model and Gain Characteristics (4.3)**

$$V(t) = \begin{cases} -V, for -\pi \le \omega t \le 0 \\ V, for\ 0 \le \omega t \le \pi \end{cases}$$

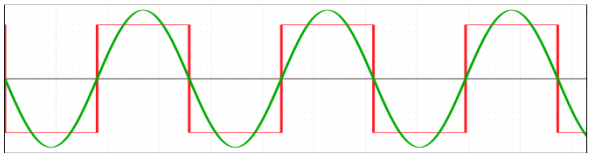

Figure 9-I First harmonic of square wave

$$a_n = \frac{1}{\pi}\int_{-\pi}^{\pi} V(t)\cos(n\omega t)d\omega t\,, n \ge 0$$

$$b_n = \frac{1}{\pi}\int_{-\pi}^{\pi} V(t)\sin(n\omega t)d\omega t\,, n \ge 0$$

$$a_0 = \frac{1}{\pi}\int_{-\pi}^{\pi} V(t)d\omega t = \frac{1}{\pi}\left(\int_{-\pi}^{0}(V)d\omega t + \int_{0}^{\pi} V d\omega t\right) = 0$$

$$a_1 = \frac{1}{\pi}\int_{-\pi}^{\pi} V(t)\cos(\omega t)\,d\omega t$$

$$= \frac{1}{\pi}\left(\int_{-\pi}^{0}(-V)\cos(\omega t)\,d\omega t + \int_{0}^{\pi} V\cos(\omega t)\,d\omega t\right)$$

$$= \frac{1}{\pi}([(-V)sin(\omega t)]_{-\pi}^{0} + [Vsin(\omega t)]_{0}^{\pi}) = 0$$

$$b_1 = \frac{1}{\pi}\int_{-\pi}^{\pi} V(t)\sin(\omega t)\,d\omega t$$

$$= \frac{1}{\pi}\left(\int_{-\pi}^{0}(-V)\sin(\omega t)\,d\omega t + \int_{0}^{\pi} V\sin(\omega t)\,d\omega t\right)$$

$$= \frac{1}{\pi}([Vcos(\omega t)]_{-\pi}^{0} + [(-V)cos(\omega t)]_{0}^{\pi}) = \frac{1}{\pi}(2V + 2V) = \frac{4}{\pi}V$$

$$V(t) = \begin{cases} 0, for -\pi \le \omega t \le 0 \\ V, for\ 0 \le \omega t \le \pi \end{cases}$$

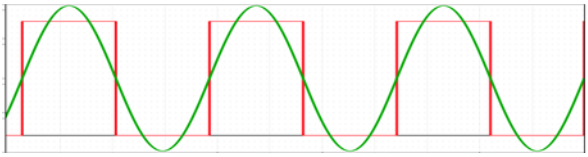

Figure 9-II First harmonic of square wave

$$a_n = \frac{1}{\pi}\int_{-\pi}^{\pi} V(t)\cos(n\omega t)d\omega t\,, n \ge 0$$

$$b_n = \frac{1}{\pi}\int_{-\pi}^{\pi} V(t)\sin(n\omega t)d\omega t\,, n \geq 0$$

$$a_0 = \frac{1}{\pi}\int_{-\pi}^{\pi} V(t)d\omega t = \frac{1}{\pi}\left(\int_{-\pi}^{0} 0d\omega t + \int_{0}^{\pi} Vd\omega t\right) = \frac{V}{2}$$

$$a_1 = \frac{1}{\pi}\int_{-\pi}^{\pi} V(t)\cos(\omega t)\,d\omega t = \frac{1}{\pi}\left(\int_{-\pi}^{0} 0d\omega t + \int_{0}^{\pi} V\cos(\omega t)\,d\omega t\right)$$
$$= \frac{1}{\pi}([Vsin(\omega t)]_0^{\pi}) = 0$$

$$b_1 = \frac{1}{\pi}\int_{-\pi}^{\pi} V(t)\sin(\omega t)\,d\omega t = \frac{1}{\pi}\left(\int_{-\pi}^{0} 0d\omega t + \int_{0}^{\pi} V\sin(\omega t)\,d\omega t\right)$$
$$= \frac{1}{\pi}([(-V)cos(\omega t)]_0^{\pi}) = \frac{1}{\pi}(V+V) = \frac{2}{\pi}V$$

- **<u>Full bridge configuration-FHA model (4.3)</u>**

The average value output current I_o is given by:

$$I_o = \frac{2}{T_s}\int_0^{\frac{T_s}{2}} \left|i_{rct,FHA}(t)\right|dt = \frac{2}{\omega T_s}\int_0^{\omega\cdot\frac{T_s}{2}} \left|i_{rct,FHA}(t)\right|d\omega t$$
$$= \frac{1}{\pi}\int_0^{\pi} \left|\sqrt{2}\cdot I_{rct,FHA}\cdot\sin(2\pi f_s\cdot t-\varphi)\right|d\omega t$$
$$= \frac{1}{\pi}\left(\int_0^{\varphi} -\sqrt{2}\cdot I_{rct,FHA}\cdot\sin(\omega t-\varphi)\,d\omega t + \int_{\varphi}^{\pi}\sqrt{2}\cdot I_{rct,FHA}\cdot\sin(\omega t-\varphi)d\omega t\right)$$
$$= \frac{\sqrt{2}\cdot I_{rct,FHA}}{\pi}\left(\int_0^{\varphi} -\sin(\omega t-\varphi)\,d\omega t + \int_{\varphi}^{\pi}\sqrt{2}\cdot I_{rct,FHA}\cdot\sin(\omega t-\varphi)d\omega t\right)$$
$$= \frac{\sqrt{2}\cdot I_{rct,FHA}}{\pi}\left([cos(\omega t-\varphi)]_0^{\varphi} + [-cos(\omega t-\varphi)]_{\varphi}^{\pi}\right)$$
$$= \frac{\sqrt{2}\cdot I_{rct,FHA}}{\pi}(1-cos(\varphi)-cos(\pi-\varphi)+1)$$
$$= \frac{2\sqrt{2}}{\pi}\cdot I_{rct,FHA}$$

$u_{ro,FHA}(t)$ and $i_{rct,FHA}(t)$ are in phase, so the resistive load of the resonant network $R_{o,e}$ can be given by the ratio of the instantaneous voltage and current:

$$R_{o,e} = \frac{u_{ro,FHA}(t)}{i_{rct,FHA}(t)} = \frac{\frac{4}{\pi}\cdot V_o\cdot\sin(2\pi f_s\cdot t-\varphi)}{\sqrt{2}\cdot I_{rct,FHA}\cdot\sin(2\pi f_s\cdot t-\varphi)} = \frac{\frac{4}{\pi}\cdot V_o}{\sqrt{2}I_o\cdot\frac{\pi}{2\sqrt{2}}} = \frac{8}{\pi^2}R_o$$

- **Half bridge configuration-FHA model (4.4)**

The average value output current I_o is given by:

$$I_o = \frac{1}{T_s}\int_0^{T_s}\left|i_{rct,FHA}(t)\right|dt = \frac{1}{T_s}\int_0^{\frac{T_s}{2}}\left|i_{rct,FHA}(t)\right|dt = \frac{\sqrt{2}}{\pi}\cdot I_{rct,FHA}$$

$u_{ro,FHA}(t)$ and $i_{rct,FHA}(t)$ are in phase, so the resistive load of the resonant network $R_{o,e}$ can be given by the ratio of the instantaneous voltage and current:

$$R_{o,e} = \frac{u_{ro,FHA}(t)}{i_{rct,FHA}(t)} = \frac{\frac{2}{\pi}\cdot V_o\cdot\sin(2\pi f_s\cdot t-\varphi)}{\sqrt{2}\cdot I_{rct,FHA}\cdot\sin(2\pi f_s\cdot t-\varphi)} = \frac{\frac{2}{\pi}\cdot V_o}{\sqrt{2}I_o\cdot\frac{\pi}{\sqrt{2}}} = \frac{2}{\pi^2}R_o$$

- **Full bridge configuration--Theoretical calculations (4.7)**

The rms value I_m of the magnetizing current $i_m(t)$ is given by:

$$I_m = \sqrt{\frac{2}{T_s}\cdot\int_0^{\frac{T_s}{2}} i_m^2(t)dt} \Rightarrow I_m = \sqrt{\frac{2}{T_s}\cdot\int_0^{\frac{T_s}{2}}\left(\frac{V_oT_s}{4L_m}-\frac{V_o}{L_m}t\right)^2 dt} \Rightarrow$$

$$I_m^2 = \frac{2}{T_s}\cdot\int_0^{\frac{T_s}{2}}\left(\left(\frac{V_oT_s}{4L_m}\right)^2+\left(\frac{V_o}{L_m}\right)^2\cdot t^2-\frac{{V_o}^2T_s}{2L_m^2}t\right)dt \Rightarrow$$

$$I_m^2 = \frac{2}{T_s}\cdot\left[\int_0^{\frac{T_s}{2}}\left(\frac{V_oT_s}{4L_m}\right)^2 dt+\int_0^{\frac{T_s}{2}}\left(\frac{V_o}{L_m}\right)^2\cdot t^2dt-\int_0^{\frac{T_s}{2}}\frac{{V_o}^2T_s}{2L_m^2}tdt\right] \Rightarrow$$

$$I_m^2 = \frac{2}{T_s}\cdot\left(\left[\left(\frac{V_oT_s}{4L_m}\right)^2\cdot t\right]_0^{\frac{T_s}{2}}+\left[\left(\frac{V_o}{L_m}\right)^2\cdot\frac{t^3}{3}\right]_0^{\frac{T_s}{2}}-\left[\frac{{V_o}^2T_s}{2L_m^2}\cdot\frac{t^2}{2}\right]_0^{\frac{T_s}{2}}\right) \Rightarrow$$

$$I_m^2 = \frac{2}{T_s}\cdot\left(\left(\frac{V_oT_s}{4L_m}\right)^2\cdot\frac{T_s}{2}+\left(\frac{V_o}{L_m}\right)^2\cdot\frac{T_s^3}{24}-\frac{{V_o}^2T_s}{2L_m^2}\cdot\frac{T_s^2}{8}\right) \Rightarrow$$

$$I_m^2 = \left(\frac{V_oT_s}{4L_m}\right)^2+\left(\frac{V_o}{L_m}\right)^2\cdot\frac{T_s^2}{12}-\frac{V_o^2}{L_m^2}\cdot\frac{T_s^2}{8} \Rightarrow$$

$$I_m^2 = \frac{1}{48}\cdot\frac{V_o^2T_s^2}{L_m^2} \Rightarrow$$

$$I_m = \frac{1}{\sqrt{48}}\cdot\frac{V_oT_s}{L_m}$$

The rms value of the primary current $i_p(t)$ can be calculated:

$$i_s(t) = \mathrm{i_p(t)} - i_m(t) \Rightarrow |i_s(t)| = \left|\mathrm{i_p(t)} - i_m(t)\right| \Rightarrow$$

$$\frac{1}{\mathrm{T_s}}\int_0^{\mathrm{T_s}} |i_s(t)|\mathrm{dt} = \frac{1}{\mathrm{T_s}}\int_0^{\mathrm{T_s}} \left|\mathrm{i_p(t)} - i_m(t)\right|\mathrm{dt} \Rightarrow$$

$$\frac{1}{\mathrm{T_s}}\int_0^{\mathrm{T_s}} |i_s(t)|\mathrm{dt} = \frac{1}{\mathrm{T_s}}\left(\int_0^{\frac{\mathrm{T_s}}{2}} -\left(\mathrm{i_p(t)} - i_m(t)\right)dt + \int_{\frac{\mathrm{T_s}}{2}}^{\mathrm{T_s}} \left(\mathrm{i_p(t)} - i_m(t)\right)dt\right) \Rightarrow$$

$$\mathrm{I_o} = \frac{1}{\mathrm{T_s}}\left(-\int_0^{\frac{\mathrm{T_s}}{2}} \mathrm{i_p(t)}dt + \int_0^{\frac{\mathrm{T_s}}{2}} i_m(t)dt + \int_{\frac{\mathrm{T_s}}{2}}^{\mathrm{T_s}} \mathrm{i_p(t)}dt - \int_{\frac{\mathrm{T_s}}{2}}^{\mathrm{T_s}} i_m(t)dt\right) \Rightarrow$$

$$\mathrm{I_o} = \frac{1}{\mathrm{T_s}}\left(-\int_0^{\frac{\mathrm{T_s}}{2}} \mathrm{i_p(t)}dt + \int_0^{\frac{\mathrm{T_s}}{2}} i_m(t)dt + \int_{\frac{\mathrm{T_s}}{2}}^{\mathrm{T_s}} \mathrm{i_p(t)}dt - \int_{\frac{\mathrm{T_s}}{2}}^{\mathrm{T_s}} i_m(t)dt\right) \Rightarrow$$

$$\mathrm{I_o} = \frac{-2}{\mathrm{T_s}}\int_0^{\frac{\mathrm{T_s}}{2}} \sqrt{2}\mathrm{I_p}\sin(2\pi \mathrm{f_r t} + \varphi)\,\mathrm{dt} \Rightarrow \mathrm{I_o} = \frac{-2}{\omega \mathrm{T_s}}\int_0^{\omega\cdot\frac{\mathrm{T_s}}{2}} \sqrt{2}\mathrm{I_p}\sin(2\pi \mathrm{f_r t} + \varphi)\,\mathrm{d}\omega\mathrm{t} \Rightarrow$$

$$\mathrm{I_o} = \frac{-\sqrt{2}\mathrm{I_p}}{\pi}\int_0^{\pi} \sin(\omega \mathrm{t} + \varphi)\,\mathrm{d}\omega\mathrm{t} \Rightarrow \mathrm{I_o} = \frac{\sqrt{2}\mathrm{I_p}}{\pi}[cos(\omega t + \varphi)]_0^{\pi} \Rightarrow$$

$$\mathrm{I_o} = \frac{\sqrt{2}\mathrm{I_p}}{\pi}(cos(\pi + \varphi) - cos\varphi) \Rightarrow \mathrm{I_o} = \frac{\sqrt{2}\mathrm{I_p}}{\pi}(cos\pi cos\varphi - sin\pi sin\varphi - cos\varphi) \Rightarrow$$

$$\mathrm{I_o} = \frac{-\sqrt{2}\mathrm{I_p}}{\pi}(2cos\varphi) \Rightarrow \mathrm{I_o} = \frac{-2\sqrt{2}\mathrm{I_p}}{\pi}\sqrt{1 - si\,n^2\,\varphi} \Rightarrow \mathrm{I_o^2} = \frac{8\mathrm{I_p^2}}{\pi^2}\left(1 - \left(\frac{\mathrm{V_o T_s}}{4\sqrt{2}\mathrm{L_m I_p}}\right)^2\right) \Rightarrow$$

$$\mathrm{I_o^2} = \frac{8\mathrm{I_p^2}}{\pi^2} - \frac{8\mathrm{I_p^2}}{\pi^2}\cdot\left(\frac{\mathrm{V_o T_s}}{4\sqrt{2}\mathrm{L_m I_p}}\right)^2 \Rightarrow \mathrm{I_o^2} = \frac{8\mathrm{I_p^2}}{\pi^2} - \frac{\mathrm{V_o^2 T_s^2}}{4\pi^2\mathrm{L_m^2}} \Rightarrow \mathrm{I_p^2} = \frac{\pi^2\mathrm{V_o^2}}{8R_o^2} + \frac{\mathrm{V_o^2 T_s^2}}{32\mathrm{L_m^2}} \Rightarrow$$

$$I_p = \sqrt{\frac{\pi^2\mathrm{V_o^2}}{8R_o^2} + \frac{\mathrm{V_o^2 T_s^2}}{32\mathrm{L_m^2}}}$$

The rms value of the secondary current $i_s(t)$ is I_s and is given by:

$$I_s = \sqrt{\frac{2}{T_s}\cdot\int_0^{\frac{T_S}{2}} i_s^2(t)dt} = \sqrt{\frac{2}{T_s}\cdot\int_0^{\frac{T_S}{2}} \left(\mathrm{i_p(t)} - i_m(t)\right)^2 dt}$$

$$I_s^2 = \frac{2}{T_s}\cdot\int_0^{\frac{T_S}{2}} \left(\mathrm{i_p(t)} - i_m(t)\right)^2 dt \Rightarrow$$

$$I_s^2 = \frac{2}{T_s}\cdot\int_0^{\frac{T_S}{2}} \left(\mathrm{i_p^2(t)} + i_m^2(t) - 2\mathrm{i_p(t)}i_m(t)\right)dt \Rightarrow$$

$$I_s^2 = \frac{2}{T_s}\cdot\int_0^{\frac{T_S}{2}} \mathrm{i_p^2(t)}dt + \frac{2}{T_s}\cdot\int_0^{\frac{T_S}{2}} i_m^2(t)dt - \frac{2}{T_s}\cdot\int_0^{\frac{T_S}{2}} 2\mathrm{i_p(t)}i_m(t)dt \Rightarrow$$

$$I_s^2 = I_p^2 + I_m^2 - \frac{2}{T_s}\cdot\int_0^{\frac{T_S}{2}} 2\sqrt{2}\mathrm{I_p}\sin(2\pi \mathrm{f_r t} + \varphi)\left(\frac{V_o T_s}{4L_m} - \frac{V_o}{L_m}t\right)dt \Rightarrow$$

$$I_s^2 = I_p^2 + I_m^2 - \frac{\sqrt{2}\mathrm{I_p}V_o}{L_m}\int_0^{\frac{T_S}{2}} \sin(2\pi \mathrm{f_r t} + \varphi)\, dt + \frac{4\sqrt{2}\mathrm{I_p}}{T_s}\frac{V_o}{L_m}\cdot\int_0^{\frac{T_S}{2}} t\cdot\sin(2\pi \mathrm{f_r t} + \varphi)\, dt \Rightarrow$$

$$I_s^2 = I_p^2 + I_m^2 - \frac{\sqrt{2}\mathrm{I_p}V_o}{\omega L_m}\int_0^{\pi} \sin(\omega \mathrm{t} + \varphi)\, d\omega t + \frac{4\sqrt{2}\mathrm{I_p}}{T_s}\frac{V_o}{\omega^2 L_m}\cdot\int_0^{\pi} \omega t\cdot\sin(\omega \mathrm{t} + \varphi)\, d\omega t \Rightarrow$$

$$I_s^2 = I_p^2 + I_m^2 - \frac{2\sqrt{2}\mathrm{I_p}V_o}{\omega L_m}cos\varphi + \frac{4\sqrt{2}\mathrm{I_p}}{2\pi}\frac{V_o}{\omega L_m}\cdot\left(\int_0^{\pi}(\omega t + \varphi)\cdot\sin(\omega \mathrm{t} + \varphi)\, d\omega t - \varphi\cdot\int_0^{\pi}\sin(\omega \mathrm{t} + \varphi)\, d\omega t\right)\Rightarrow$$

$$I_s^2 = I_p^2 + I_m^2 - \frac{2\sqrt{2}\mathrm{I_p}V_o}{\omega L_m}cos\varphi + \frac{4\sqrt{2}\mathrm{I_p}}{2\pi}\frac{V_o}{\omega L_m}\cdot([-(\omega t + \varphi)cos(\omega t + \varphi) + sin(\omega t + \varphi)]_0^{\pi} - 2\varphi cos\varphi)\Rightarrow$$

$$I_s^2 = I_p^2 + I_m^2 - \frac{2\sqrt{2}\mathrm{I_p}V_o}{\omega L_m}cos\varphi + \frac{2\sqrt{2}\mathrm{I_p}}{\pi}\frac{V_o}{\omega L_m}\cdot(-(\pi + \varphi)cos(\pi + \varphi) + sin(\pi + \varphi) + \varphi cos\varphi - sin\varphi - 2\varphi cos\varphi)\Rightarrow$$

$$I_s^2 = I_p^2 + I_m^2 - \frac{2\sqrt{2}\mathrm{I_p}V_o}{\omega L_m}cos\varphi + \frac{2\sqrt{2}\mathrm{I_p}}{\pi}\frac{V_o}{\omega L_m}\cdot(\pi cos\varphi - 2sin\varphi)$$

The voltage $v_{Cr_1}(t)$ across the capacitor is

$$i_p(t) = Cr_1\cdot\frac{dv_{Cr_1}(t)}{dt}\Rightarrow v_{Cr_1}(t) = \frac{1}{Cr_1}\int_0^t i_p(t)dt + v_{Cr_1}(0)\Rightarrow$$

$$v_{Cr_1}(t) = \frac{1}{Cr_1}\int_0^t \sqrt{2}\mathrm{I_p}\sin(2\pi \mathrm{f_r t} + \varphi)dt + v_{Cr_1}(0)\Rightarrow$$

$$v_{Cr_1}(t) = \frac{\sqrt{2}\mathrm{I_p}}{Cr_1}\int_0^t \sin(\omega \mathrm{t} + \varphi)dt + v_{Cr_1}(0)\Rightarrow$$

$$v_{Cr_1}(t) = \frac{\sqrt{2}\mathrm{I_p}}{\omega Cr_1}\cdot[-cos(\omega t + \varphi)]_0^{\omega t} + v_{Cr_1}(0)\Rightarrow$$

$$v_{Cr_1}(t) = \frac{\sqrt{2}\mathrm{I_p}}{\omega Cr_1}\cdot[-cos(\omega t + \varphi) + cos\varphi] + v_{Cr_1}(0)$$

The voltage $v_{Cr_2}(t)$ across the capacitor is

$$i_s(t) = Cr_2\cdot\frac{dv_{Cr_2}(t)}{dt}\Rightarrow v_{Cr_2}(t) = \frac{1}{Cr_2}\int_0^t i_s(t)dt + v_{Cr_2}(0)\Rightarrow$$

$$v_{Cr_2}(t) = \frac{1}{Cr_2}\int_0^t \left(\mathrm{i_p(t)} - i_m(t)\right)dt + v_{Cr_2}(0)\Rightarrow$$

$$v_{Cr_2}(t) = \begin{cases} \frac{1}{Cr_2}\int_0^t \left(\mathrm{i_p(t)} - \frac{V_o T_s}{4L_m} + \frac{V_o}{L_m}t\right)dt + v_{Cr_2}(0), for\ 0 \le t \le \frac{\mathrm{T_s}}{2} \\ \frac{1}{Cr_2}\int_0^{\frac{\mathrm{T_s}}{2}} \left(\mathrm{i_p(t)} - \frac{V_o T_s}{4L_m} + \frac{V_o}{L_m}t\right)dt + \frac{1}{Cr_2}\int_{\frac{\mathrm{T_s}}{2}}^t \left(\mathrm{i_p(t)} + \frac{V_o T_s}{4L_m} - \frac{V_o}{L_m}t\right)dt + v_{Cr_2}(0), for\ \frac{\mathrm{T_s}}{2} \le t \le \mathrm{T_s} \end{cases}$$

- **<u>Half bridge configuration --Theoretical calculations (4.10)</u>**

The rms value I_m of the magnetizing current $i_m(t)$ is given by:

$$I_m = \sqrt{\frac{2}{T_s}\cdot\int_0^{\frac{T_S}{2}} i_m^2(t)dt} \Rightarrow I_m = \sqrt{\frac{2}{T_s}\cdot\int_0^{\frac{T_S}{2}} \left(\frac{V_o T_s}{8L_m} - \frac{V_o}{2L_m}t\right)^2 dt} \Rightarrow$$

$$I_m^2 = \frac{2}{T_s}\cdot\int_0^{\frac{T_S}{2}} \left(\left(\frac{V_o T_s}{8L_m}\right)^2 + \left(\frac{V_o}{2L_m}\right)^2\cdot t^2 - \frac{{V_o}^2 T_s}{8L_m^2}t\right) dt \Rightarrow$$

$$I_m^2 = \frac{2}{T_s}\cdot\left[\int_0^{\frac{T_S}{2}} \left(\frac{V_o T_s}{8L_m}\right)^2 dt + \int_0^{\frac{T_S}{2}} \left(\frac{V_o}{2L_m}\right)^2\cdot t^2 dt - \int_0^{\frac{T_S}{2}} \frac{{V_o}^2 T_s}{8L_m^2}tdt\right] \Rightarrow$$

$$I_m^2 = \frac{2}{T_s}\cdot\left(\left[\left(\frac{V_o T_s}{8L_m}\right)^2\cdot t\right]_0^{\frac{T_S}{2}} + \left[\left(\frac{V_o}{2L_m}\right)^2\cdot\frac{t^3}{3}\right]_0^{\frac{T_S}{2}} - \left[\frac{{V_o}^2 T_s}{8L_m^2}\cdot\frac{t^2}{2}\right]_0^{\frac{T_S}{2}}\right) \Rightarrow$$

$$I_m^2 = \frac{2}{T_s}\cdot\left(\left(\frac{V_o T_s}{8L_m}\right)^2\cdot\frac{T_S}{2} + \left(\frac{V_o}{2L_m}\right)^2\cdot\frac{T_s^3}{24} - \frac{{V_o}^2 T_s}{8L_m^2}\cdot\frac{T_s^2}{8}\right) \Rightarrow$$

$$I_m^2 = \left(\frac{V_o T_s}{8L_m}\right)^2 + \left(\frac{V_o}{2L_m}\right)^2\cdot\frac{T_s^2}{12} - \frac{V_o^2}{8L_m^2}\cdot\frac{T_s^2}{4} \Rightarrow$$

$$I_m^2 = \frac{1}{192}\cdot\frac{V_o^2 T_s^2}{L_m^2} \Rightarrow$$

$$I_m = \frac{1}{2\sqrt{48}}\cdot\frac{V_o T_s}{L_m}$$

The rms value of the primary current $\mathrm{i_p(t)}$ can be calculated:

$$i_s(t) = \mathrm{i_p(t)} - i_m(t) \Rightarrow |i_s(t)| = \left|\mathrm{i_p(t)} - i_m(t)\right| \Rightarrow$$

$$\frac{1}{\mathrm{T_s}}\int_0^{\mathrm{T_s}} |i_s(t)|\mathrm{dt} = \frac{1}{\mathrm{T_s}}\int_0^{\mathrm{T_s}} \left|\mathrm{i_p(t)} - i_m(t)\right|\mathrm{dt} \Rightarrow$$

$$\frac{1}{\mathrm{T_s}}\int_0^{\mathrm{T_s}} |i_s(t)|\mathrm{dt} = \frac{1}{\mathrm{T_s}}\left(\int_0^{\frac{\mathrm{T_s}}{2}} -\left(\mathrm{i_p(t)} - i_m(t)\right) dt + \int_{\frac{\mathrm{T_s}}{2}}^{\mathrm{T_s}} \left(\mathrm{i_p(t)} - i_m(t)\right) dt\right) \Rightarrow$$

$$2\mathrm{I_o} = \frac{1}{\mathrm{T_s}}\left(-\int_0^{\frac{\mathrm{T_s}}{2}} \mathrm{i_p(t)}dt + \int_0^{\frac{\mathrm{T_s}}{2}} i_m(t)dt + \int_{\frac{\mathrm{T_s}}{2}}^{\mathrm{T_s}} \mathrm{i_p(t)}dt - \int_{\frac{\mathrm{T_s}}{2}}^{\mathrm{T_s}} i_m(t)dt\right) \Rightarrow$$

$$2\mathrm{I_o} = \frac{1}{\mathrm{T_s}}\left(-\int_0^{\frac{\mathrm{T_s}}{2}} \mathrm{i_p(t)}dt + \int_0^{\frac{\mathrm{T_s}}{2}} i_m(t)dt + \int_{\frac{\mathrm{T_s}}{2}}^{\mathrm{T_s}} \mathrm{i_p(t)}dt - \int_{\frac{\mathrm{T_s}}{2}}^{\mathrm{T_s}} i_m(t)dt\right) \Rightarrow$$

$$2\mathrm{I_o} = \frac{-2}{\mathrm{T_s}}\int_0^{\frac{\mathrm{T_s}}{2}} \sqrt{2}\mathrm{I_p}\sin(2\pi\mathrm{f_r t} + \varphi)\,\mathrm{dt} \Rightarrow \mathrm{I_o} = \frac{-2}{\omega\mathrm{T_s}}\int_0^{\omega\cdot\frac{\mathrm{T_s}}{2}} \sqrt{2}\mathrm{I_p}\sin(2\pi\mathrm{f_r t} + \varphi)\,\mathrm{d\omega t} \Rightarrow$$

$$2\mathrm{I_o} = \frac{-\sqrt{2}\mathrm{I_p}}{\pi}\int_0^{\pi} \sin(\omega\mathrm{t} + \varphi)\,\mathrm{d\omega t} \Rightarrow \mathrm{I_o} = \frac{\sqrt{2}\mathrm{I_p}}{\pi}[cos(\omega t + \varphi)]_0^{\pi} \Rightarrow$$

$$2\mathrm{I_o}=\frac{\sqrt{2}\mathrm{I_p}}{\pi}(cos(\pi+\varphi)-cos\varphi)\Rightarrow \mathrm{I_o}=\frac{\sqrt{2}\mathrm{I_p}}{\pi}(cos\pi cos\varphi-sin\pi sin\varphi-cos\varphi)\Rightarrow$$

$$2\mathrm{I_o}=\frac{-\sqrt{2}\mathrm{I_p}}{\pi}(2cos\varphi)\Rightarrow 2\mathrm{I_o}=\frac{-2\sqrt{2}\mathrm{I_p}}{\pi}\sqrt{1-sin^2\varphi}\Rightarrow 4\mathrm{I_o^2}=\frac{8\mathrm{I_p^2}}{\pi^2}\left(1-\left(\frac{\mathrm{V_o T_s}}{8\sqrt{2}\mathrm{L_m I_p}}\right)^2\right)\Rightarrow$$

$$4\mathrm{I_o^2}=\frac{8\mathrm{I_p^2}}{\pi^2}-\frac{8\mathrm{I_p^2}}{\pi^2}\cdot\left(\frac{\mathrm{V_o T_s}}{8\sqrt{2}\mathrm{L_m I_p}}\right)^2\Rightarrow 4\mathrm{I_o^2}=\frac{8\mathrm{I_p^2}}{\pi^2}-\frac{\mathrm{V_o^2 T_s^2}}{16\pi^2\mathrm{L_m^2}}\Rightarrow \mathrm{I_p^2}=\frac{\pi^2\mathrm{V_o^2}}{2R_o^2}+\frac{\mathrm{V_o^2 T_s^2}}{128\mathrm{L_m^2}}\Rightarrow$$

$$I_p=\sqrt{\frac{\pi^2\mathrm{V_o^2}}{2R_o^2}+\frac{\mathrm{V_o^2 T_s^2}}{128\mathrm{L_m^2}}}$$

The rms value of the secondary current $i_s(t)$ is I_s and is given by:

$$I_s=\sqrt{\frac{2}{T_s}\cdot\int_0^{\frac{T_S}{2}}i_s^2(t)dt}=\sqrt{\frac{2}{T_s}\cdot\int_0^{\frac{T_S}{2}}\left(\mathrm{i_p(t)}-i_m(t)\right)^2dt}$$

$$I_s^2=\frac{2}{T_s}\cdot\int_0^{\frac{T_S}{2}}\left(\mathrm{i_p(t)}-i_m(t)\right)^2dt\Rightarrow$$

$$I_s^2=\frac{2}{T_s}\cdot\int_0^{\frac{T_S}{2}}\left(\mathrm{i_p^2(t)}+i_m^2(t)-2\mathrm{i_p(t)}i_m(t)\right)dt\Rightarrow$$

$$I_s^2=\frac{2}{T_s}\cdot\int_0^{\frac{T_S}{2}}\mathrm{i_p^2(t)}dt+\frac{2}{T_s}\cdot\int_0^{\frac{T_S}{2}}i_m^2(t)dt-\frac{2}{T_s}\cdot\int_0^{\frac{T_S}{2}}2\mathrm{i_p(t)}i_m(t)dt\Rightarrow$$

$$I_s^2=I_p^2+I_m^2-\frac{2}{T_s}\cdot\int_0^{\frac{T_S}{2}}2\sqrt{2}\mathrm{I_p}\sin(2\pi\mathrm{f_r t}+\varphi)\left(\frac{V_oT_s}{8L_m}-\frac{V_o}{2L_m}t\right)dt\Rightarrow$$

$$I_s^2=I_p^2+I_m^2-\frac{\sqrt{2}\mathrm{I_p}V_o}{2L_m}\int_0^{\frac{T_S}{2}}\sin(2\pi\mathrm{f_r t}+\varphi)\,dt+\frac{2\sqrt{2}\mathrm{I_p}}{T_s}\frac{V_o}{L_m}\cdot\int_0^{\frac{T_S}{2}}t\cdot\sin(2\pi\mathrm{f_r t}+\varphi)\,dt\Rightarrow$$

$$I_s^2=I_p^2+I_m^2-\frac{\sqrt{2}\mathrm{I_p}V_o}{2\omega L_m}\int_0^{\pi}\sin(\omega\mathrm{t}+\varphi)\,d\omega t+\frac{2\sqrt{2}\mathrm{I_p}}{T_s}\frac{V_o}{\omega^2L_m}\cdot\int_0^{\pi}\omega t\cdot\sin(\omega\mathrm{t}+\varphi)\,d\omega t\Rightarrow$$

$$I_s^2=I_p^2+I_m^2-\frac{\sqrt{2}\mathrm{I_p}V_o}{\omega L_m}cos\varphi+\frac{2\sqrt{2}\mathrm{I_p}}{2\pi}\frac{V_o}{\omega L_m}\cdot\left(\int_0^{\pi}(t+\varphi)\cdot\sin(\omega\mathrm{t}+\varphi)\,d\omega t-\varphi\cdot\int_0^{\pi}\sin(\omega\mathrm{t}+\varphi)\,d\omega t\right)\Rightarrow$$

$$I_s^2=I_p^2+I_m^2-\frac{\sqrt{2}\mathrm{I_p}V_o}{\omega L_m}cos\varphi+\frac{2\sqrt{2}\mathrm{I_p}}{2\pi}\frac{V_o}{\omega L_m}\cdot([-(\omega t+\varphi)cos(\omega t+\varphi)+sin(\omega t+\varphi)]_0^{\pi}-2\varphi cos\varphi)\Rightarrow$$

$$I_s^2=I_p^2+I_m^2-\frac{\sqrt{2}\mathrm{I_p}V_o}{\omega L_m}cos\varphi+\frac{\sqrt{2}\mathrm{I_p}}{\pi}\frac{V_o}{\omega L_m}\cdot(-(\pi+\varphi)cos(\pi+\varphi)+sin(\pi+\varphi)+\varphi cos\varphi-sin\varphi-2\varphi cos\varphi)\Rightarrow$$

$$I_s^2=I_p^2+I_m^2-\frac{\sqrt{2}\mathrm{I_p}V_o}{\omega L_m}cos\varphi+\frac{\sqrt{2}\mathrm{I_p}}{\pi}\frac{V_o}{\omega L_m}\cdot(\pi cos\varphi-2sin\varphi)$$

9.2. Results

- **20 cm distance, X=15cm,Y=0, full bridge configuration**

The efficiency measurements carried out in the lab are summarized in the graph:

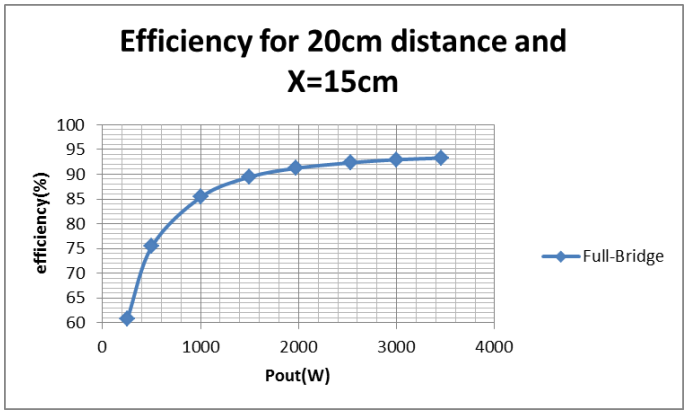

Figure 9-III Measured Efficiency

The results from the PLECS simulation for nominal operation are depicted below:

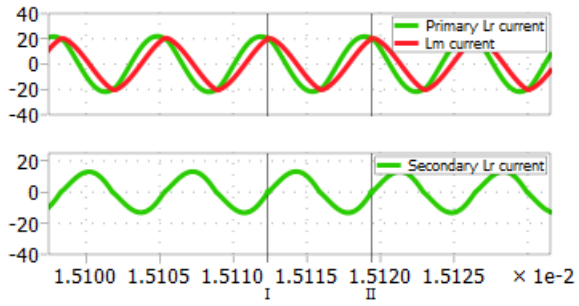

Figure 9-IV Simulation of the currents for nominal operation

The estimated efficiency curve for the whole output power range is depicted below:

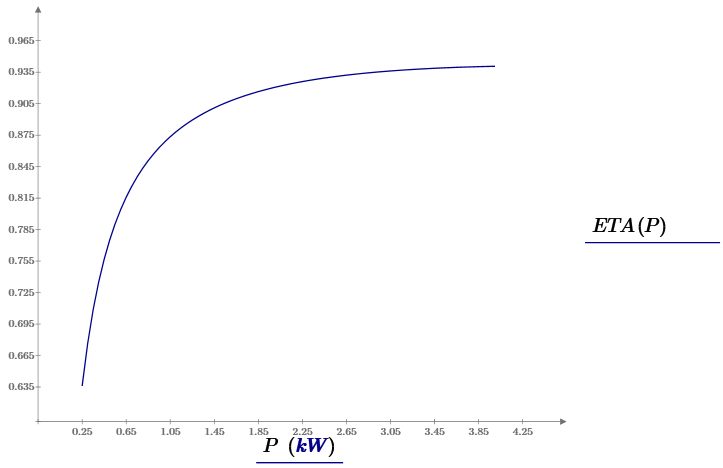

Figure 9-V Theoretically estimated efficiency curve

The power losses for the whole output power range are summarized:

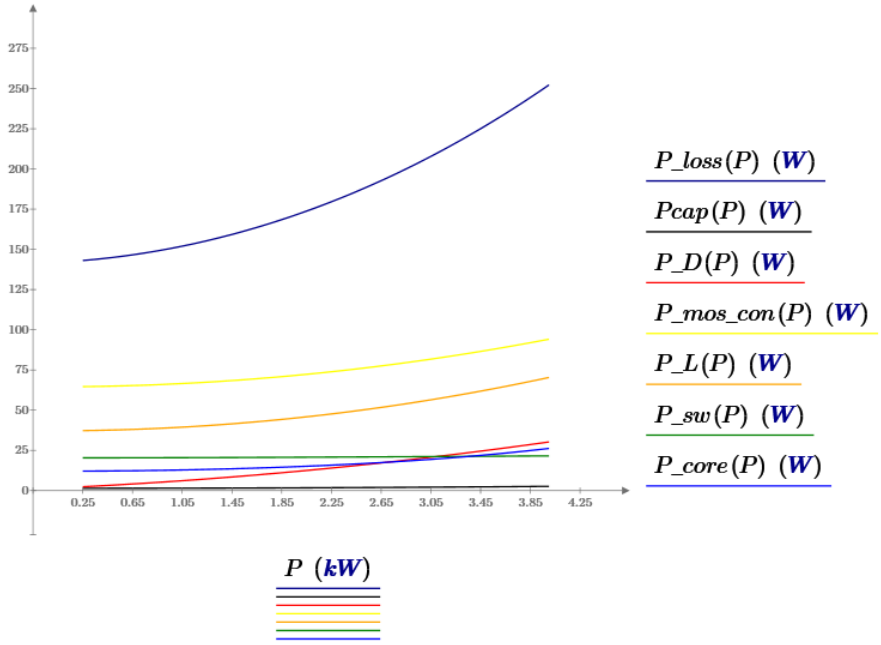

Figure 9-VI Theoretically calculated power losses for the whole output power range

The losses under nominal load conditions of operation (3,3kW) are presented here:

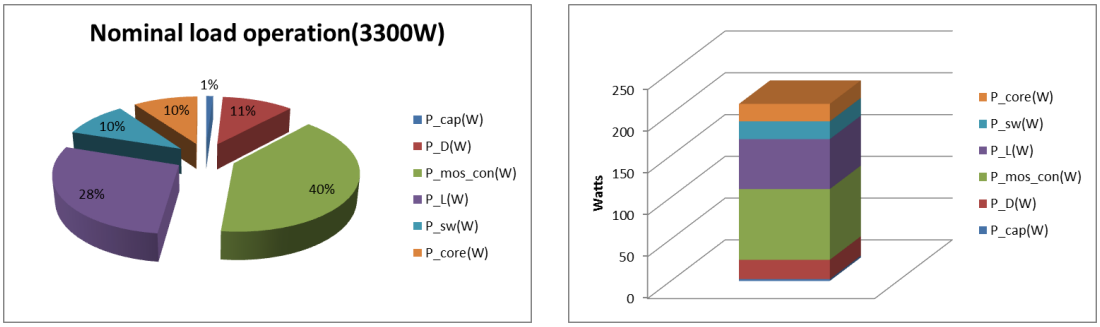

Figure 9-VII Losses analysis for nominal load conditions of operation

- **20 cm distance, X=15cm,Y=5cm, full bridge configuration**

The efficiency measurements carried out in the lab are summarized in the graph:

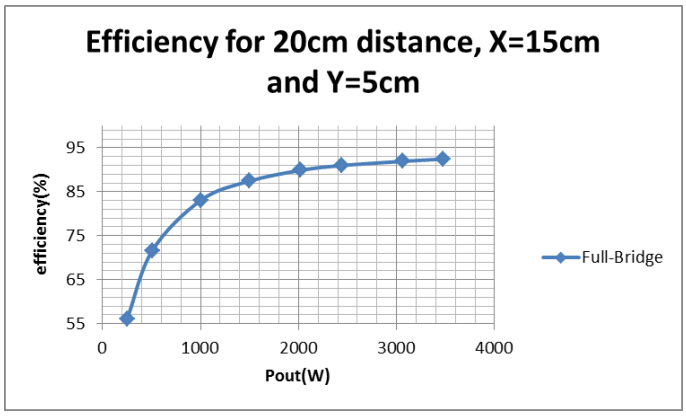

Figure 9-VIII Measured Efficiency

The results from the PLECS simulation for nominal operation are depicted below:

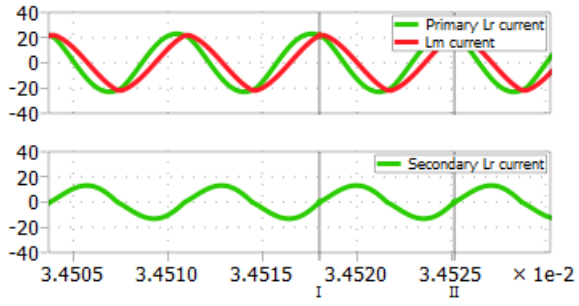

Figure 9-IX Simulation of the currents for nominal operation

The estimated efficiency curve for the whole output power range is depicted below:

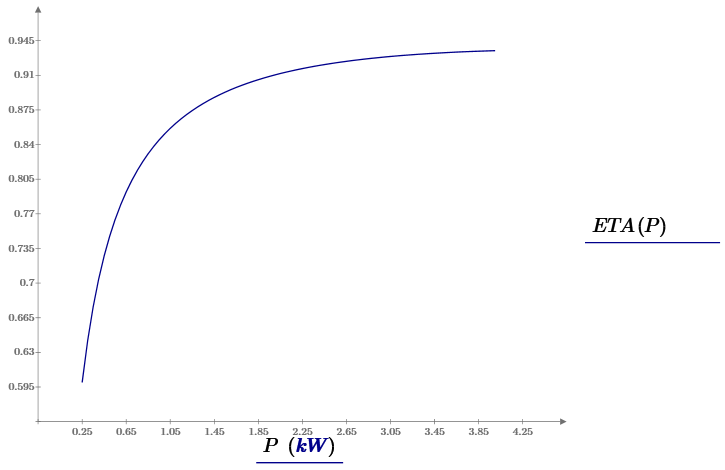

Figure 9-X Theoretically estimated efficiency curve

The power losses for the whole output power range are summarized:

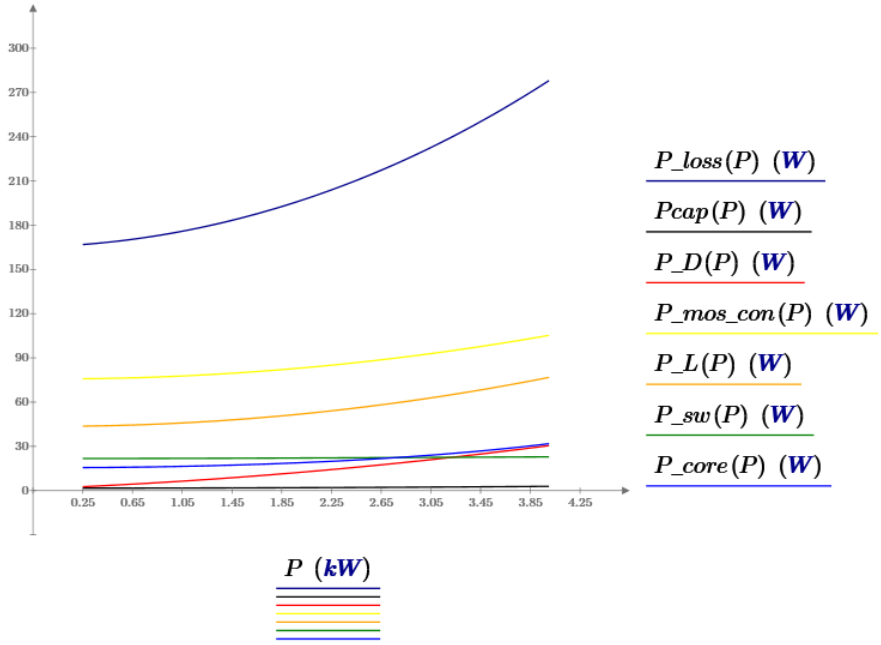

Figure 9-XI Theoretically calculated power losses for the whole output power range

The losses under nominal load conditions of operation (3,3kW) are presented here:

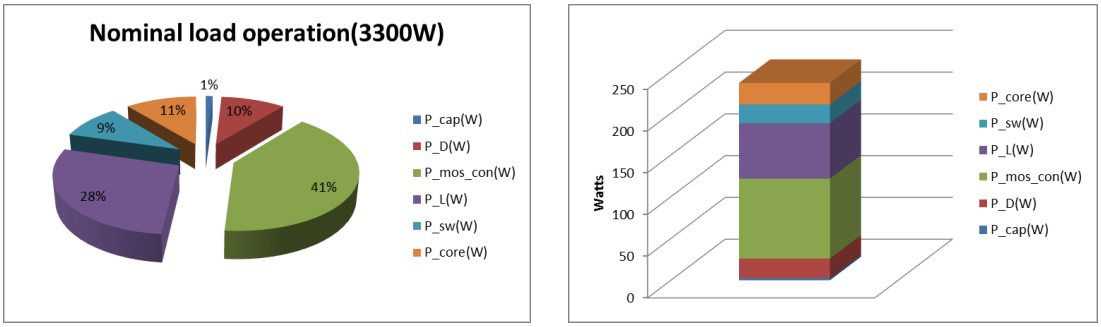

Figure 9-XII Losses analysis for nominal load conditions of operation

- **20 cm distance, X=15cm,Y=5cm, half bridge configuration**

The efficiency measurements carried out in the lab are summarized in the graph:

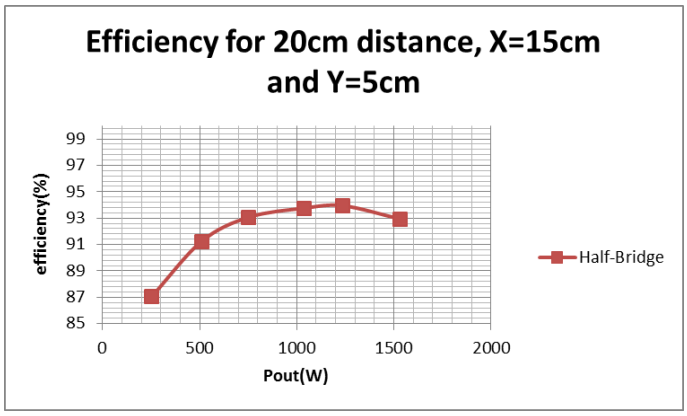

Figure 9-XIII Measured Efficiency

The results from the PLECS simulation for nominal operation are depicted below:

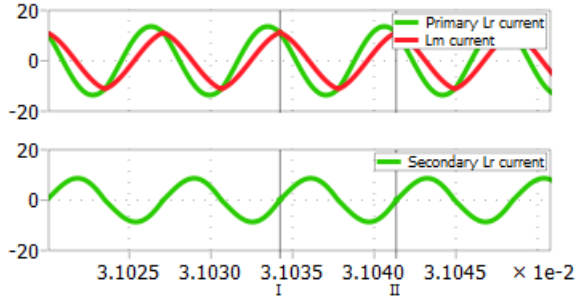

Figure 9-XIV Simulation of the currents for nominal operation

The estimated efficiency curve for the whole output power range is depicted below:

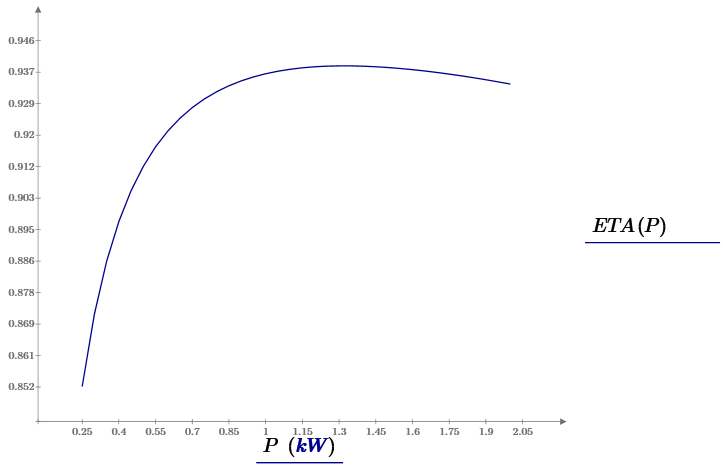

Figure 9-XV Theoretically estimated efficiency curve

The power losses for the whole output power range are summarized:

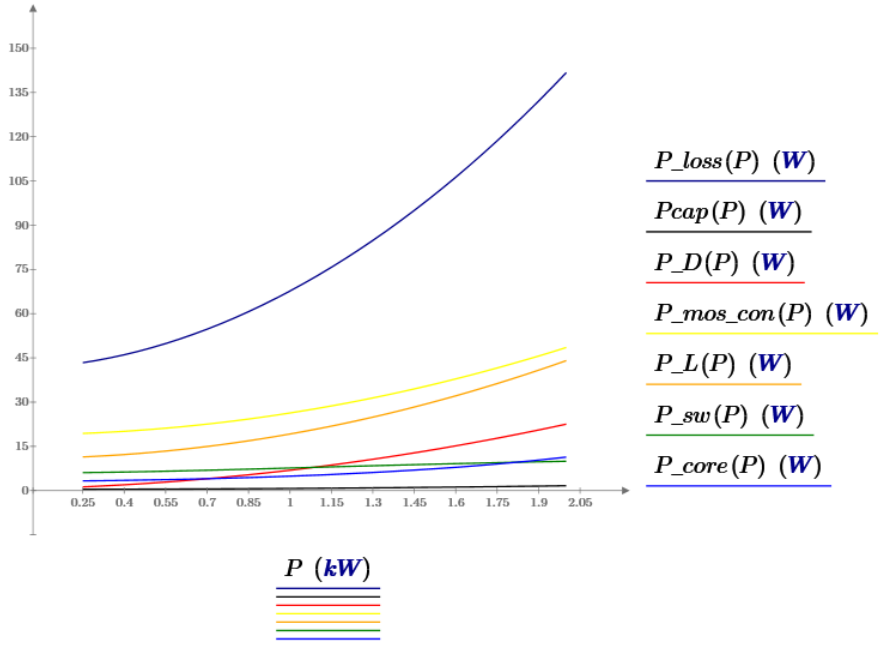

Figure 9-XVI Theoretically calculated power losses for the whole output power range

The losses under nominal load conditions of operation (1,1kW) are presented here:

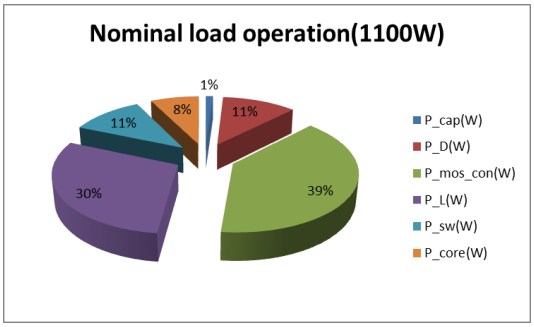

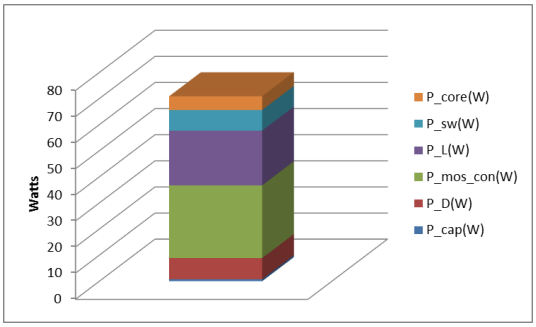

Figure 9-XVII Losses analysis for nominal load conditions of operation